Advanced Signal Processing Algorithms for GNSS/OFDM Receiver

Damien Serant

Université de Toulouse

THÈSE

En vue de l'obtention du

DOCTORAT DE L'UNIVERSITÉ DE TOULOUSE

Délivré par :
Institut National Polytechnique de Toulouse (INP Toulouse)

Présentée et soutenue par :
Damien SERANT

Le samedi 13 octobre 2012

Titre :

Advanced Signal Processing Algorithms for GNSS/OFDM Receiver

ED MITT : Domaine STIC : Réseaux, Télécoms, Systèmes et Architecture

Unité de recherche :
Laboratoire SIGNAV - École Nationale de L'Aviation Civile

Directeur(s) de Thèse :

Dr. Christophe MACABIAU
Pr. Marie-Laure Boucheret

Rapporteurs :

Pr. Giovanni E. Corazza
Pr. Daniel Roviras

Autre(s) membre(s) du jury :

Dr. Stephan Sand
Dr. Olivier Julien

Résumé

De par le développement de nombreux services et d'applications de localisation (positionnement des téléphones mobiles, aide à la personne…), le positionnement urbain et à l'intérieur des bâtiments représente aujourd'hui un marché important. Cependant, ces environnements sont très contraignants pour les systèmes de positionnement par satellites, à cause du blocage du signal par les bâtiments, des multitrajets, des interférences, etc. Même si des adaptations du système de positionnement par satellites existent pour réduire ces problèmes (récepteur haute-sensibilité, Assisted-GPS, évolutions système), elles ne permettent pas d'atteindre une disponibilité, une continuité et une précision suffisantes en ville et à l'intérieur des bâtiments.

Quelques alternatives au positionnement par satellites permettent de compléter ce dernier dans ces environnements difficiles. Ce sont, par exemple, d'autres capteurs de position (accéléromètres, magnétomètres, gyroscopes, odomètres, laser, vidéo), ou des systèmes radio dédiés (pseudolites, RFID, UWB) ou encore des signaux d'opportunités (SO).

Les SO sont des signaux de communication (par exemple : des signaux téléphonie mobile, radio, TV, Wifi) qui sont utilisés opportunément pour faire du positionnement. Bien que ces signaux ne soient pas prévus pour de telles applications, ils ont l'avantage d'être nombreux et variés dans les villes et à l'intérieur des bâtiments. De plus, ils permettent, de par leur nature, une bonne intégration des services de positionnement et de communication.

Parmi tous les SO envisageable, cette thèse se concentre sur ceux basés sur la modulation « Orthogonal Frequency Division Multiplexing » (OFDM), qui apparait comme un choix évident, du fait de son incroyable popularité parmi les standards de communication actuels et futurs (Wi-Fi, WiMAX, LTE, DVB-T/H/SH, DAB, T-DMB, ISDB-T, MediaFLO utilisent tous la modulation OFDM). Parmi tous les standard existants basés sur la modulation OFDM, le standard européen « Digital Video Broascasting – Terrestrial » de télévision numérique terrestre, a été choisi comme cas d'étude dans cette thèse car sa structure est relativement simple, permettant la réutilisation du travail pour d'autres standards basés sur la modulation OFDM et qu'il est déjà opérationnel et déployé en Europe, rendant possible des tests sur signaux réels.

Une méthode de mesure de pseudodistance basée sur des mesures de temps de propagation et utilisant les signaux DVB-T a été développée. Cette méthode utilise des boucles à verrouillage de retard (DLL) et prend en compte la spécificité des canaux de propagation terrestres (nombreux multitrajets, signal direct parfois absent, évanouissement du signal reçu…).

Les performances de cette méthode ont été déterminées théoriquement et validées par simulation, dans un cas idéal (canal de propagation gaussien). Cette étude théorique montre notamment un

écart-type de l'erreur d'estimation de la pseudodistance de l'ordre du mètre pour des SNR supérieurs à -20 dB, soit 30 à 40 dB en dessous du SNR requis pour décoder le signal TV.

Les performances dans un canal réaliste ont été déterminées empiriquement grâce à des tests sur signaux réels. Un banc de test à été développé . Il permet la réception de signaux TV avec deux antennes indépendantes et est muni d'un récepteur GPS pour avoir une référence de position et fournir une référence de temps au reste du banc de test.

Des mesures sur signaux réels on été réalisées dans plusieurs environnements (rural, urbain et à l'intérieur de bâtiments) en utilisant un émetteur TV synchronisé sur le temps GPS ou deux émetteurs en réseau mono-fréquence (SFN).

Les résultats des mesures sur signaux réels ont montré des écart-types de l'erreur d'estimation de pseudodistance de l'ordre de la dizaine de mètres, avec de meilleures performances en environnement rural (car moins de multitrajets) et une amélioration de la performance lors de l'utilisation de la diversité d'antenne.

Finalement, cette thèse montre la faisabilité du positionnement grâce à des signaux utilisant la modulation OFDM, avec une technique pouvant être facilement adaptée à d'autres signaux OFDM que le DVB-T (par exemple : LTE).

Abstract

The recent years have shown a growing interest in urban and indoor positioning with the development of applications such as car navigation, pedestrian navigation, local search and advertising and others location-based-services (LBS). However, in urban and indoor environment the classical mean of positioning, the Global Positioning Satellite System (GNSS) has limited availability, accuracy, continuity and integrity due to signal blockage by building, intense multipath conditions and interferences from the other signals, abundant in metropolitan areas. Even some improvements of GNSS can reduce these issues (high-sensitivity receiver, assisted-GNSS, multi-constellation GNSS…), they do not permit to reach sufficient performance in deep urban and indoor environments.

However, some alternatives to GNSS allow complementing it in difficult environments. They are, for example, additional sensors (accelerometers, gyrometers, magnetometers, odometers, laser, and video), radiofrequency systems dedicated to positioning (pseudolites, RFID, UWB) or signals of opportunity (SoO).

SoO are telecommunication signals (as mobile phone, TV, radio, Wi-Fi) that are used opportunely to provide a positioning service. Even if these signals are not designed for such application, they have the advantages to be many and varied in urban and indoor environments. In addition they allow, by definition, a good integration of communication and positioning services.

Among all the SoO available, this thesis focuses on the one based on the Orthogonal Frequency Division Multiplexing (OFDM) modulation. This choice is motivated by the important popularity of this modulation, that has been chosen in several actual and future telecommunication and broadcasting standards (Wi-Fi, WiMAX, LTE, DVB-T/H/SH, DAB, T-DMB, ISDB-T, MediaFLO…). Among this standard using the OFDM modulation, the European standard for digital television called “Digital Video Broadcasting – Terrestrial” (DVB-T) has been selected to be studied in this thesis. The choice is motivated by the relatively simple definition of this standard, allowing reuse of the work for other OFDM standards, and also because it is already operational in Europe, allowing tests on real signals.

A method to obtain ranging measurements based on timing synchronization using DVB-T signals has been developed. This method uses delay lock loops (DLL) and takes into account the specificity of the terrestrial propagation channel (many multipathes, direct signal sometimes absent, quick variation of received power…).

The performance of the method has been determinate theoretically and validated by simulation, in an ideal case (i.e.; with a Gaussian propagation channel). This theoretical study has proven than the ranging error standard deviation has an order of magnitude of 1 meter, for signal to noise ratio of about -20 dB, a SNR 40 dB under the demodulation threshold of the TV signal.

The performance in a realistic propagation channel has been determined on real signal. For that purpose a test bench has been developed. It allows to receive and record TV signals on two synchronized antennas and it includes and GPS receiver to record a reference position and provide a GPS time reference to the test bench.

Tests on real signals have been realized in several environments (sub-urban, urban and indoor) using 1 emitter synchronized on GPS time and 2 emitters in a signal frequency network (SFN).

The results of these tests on real signals showed a precision of the ranging estimation of about 10 meters with a better performance in rural environment and an improvement of the ranging estimate using antenna diversity.

Finally, the thesis proves the feasibility of positioning with signal using the OFDM modulation, with a technique that can be easily tailored to other OFDM signal than DVB-T.

Remerciements

I want to thank you Prof. Daniel Roviras, CNAM, and Prof. Giovanni E. Corazza, Università Di Bologna, for having accepted to be reviewer of my PhD thesis and for their valuable comments to improve my work. Thanks also to Dr. Stefan Sand, DLR, to have accepted to be member of the PhD defense jury.

Je voudrais remercier également mes directeurs de thèse, Prof. Marie-Laure Boucheret, INPT et Dr. Christophe Macabiau, ENAC, pour leurs conseils, leur aide et leur soutient durant toute ma thèse.

Un grand merci également au CNES et Thales Alénia Space pour avoir financé ma thèse et à leur représentants qui l'ont suivi, à savoir Lionel Ries pour le CNES et Mathieu Dervin et Stéphane Corazza pour Thales Alenia Space.

Bien sûr, je tiens à remercier tout particulièrement Dr. Olivier Julien, mon superviseur au quotidien, sans qui ce travail n'aurait pas été possible. Je tiens à saluer sa grande qualité d'encadrant, tant au plan technique que humain, qui a largement contribué à faire de ces trois années de thèse une expérience très enrichissante et très agréable.

Bien sûr ces trois années géniales que j'ai passé à l'ENAC doivent beaucoup à la très bonne ambiance qui règne dans ce labo, je pense que toutes les personnes qui y sont passé pourront confirmer cela. Christophe, ta personnalité unique explique en grande partie cet attachement qu'on a tous pour les années qu'on a passé ici, à la maison comme on dit, tu peux être très fier de cela. J'y ai rencontré beaucoup de personnes géniales, je ne les citerais pas toutes, mais au moins un grand merci à mes voisins de bureau successifs, Paul et Kevin, qui ont en partie fait que j'arrivais au travail avec le sourire (certes tard ^_^) et en me disant que j'allais passer une bonne journée.

Enfin je tiens à écrire tout la reconnaissance et l'affection que j'ai pour mes parents, mes frères et sœurs, mes neveux et nièce, qui m'ont apporté équilibre et soutien durant toute ma scolarité, et donc aussi durant ma thèse et qui sont donc largement contributeurs, sans même le savoir, de ce travail.

Table of content

List of figures

List of tables

List of acronyms

AOA	Angle of Arrival
AWGN	Additive White Gaussian Noise
BOC	Binary Offset Carrier
BS	Base Station
CFO	Carrier Frequency Offset
CP	Cyclic Prefix
DLL	Delay Lock Loop
DTV	Digital Television
DVB-H	Digital Video Broadcasting – Handheld
DVB-SH	Digital Video Broadcasting – Satellite-to-Handheld
DVB-T	Digital Video Broadcasting – Terrestrial
EMLP	Early Minus Late Power
ETSI	European Telecommunications Standards Institute
FFT	Fast Fourier Transform
FLL	Frequency Lock Loop
GNSS	Global Navigation Satellite System
GNU	GNU is not Unix
GPS	Global Positioning System
GSM	Global System for Mobile Communications
ICI	Inter-Carrier Interference
iFFT	Inverse FFT
ISI	Inter-Symbol Interference
LBS	Local Based Services
MFN	Multi-Frequency Network
MIMO	Multiple-Input Multiple-Output
MP	Matching Pursuit
NLOS	Non-Line-of-Sight
OFDM	Orthogonal Frequency Division Multiplexing
PPP	Precise Point Positioning
PPS	Pulse per Second
PR	Pseudo-range
PRBS	Pseudo-random Binary Sequence
RFID	Radio Frequency Identification

SCO	Sample Clock Offset
SFN	Single Frequency Network
SNR	Signal to Noise Ratio
SoO	Signal (or System) of Opportunity
TDOA	Time Difference of Arrival
TOA	Time of Arrival
TPS	Transmission Parameter Signaling
TTFF	Time to first fix
UHD	USRP Hardware Driver
UHF	Ultra High Frequency
UMTS	Universal Mobile Telecommunications System
USRP	Universal Software Radio Peripheral
UWB	Ultra Wide Band
VHF	Very High Frequency

Notations

N	Size of the FFT (de)modulator / Number of sample in an OFDM symbol without cyclic prefix / Number of modulated symbols in an OFDM symbol
N_{CP}	Size of the Cyclic Prefix window / Number of samples in the cyclic prefix
N_t	$N + N_{CP}$, Number of samples in a complete OFDM symbol
d	Modulated QAM or PSK symbol (just before iFFT modulator)
$\tilde{d}$	Demodulated symbol (just after FFT demodulator)
$\hat{d}$	Decided symbol (after channel equalization and decision)
p	$\in [0, N_{FFT} - 1]$ - Index of the subcarrier (or modulated symbol) in a block of N_{FFT} elements
k	$\in \mathbb{N}$ - Index of the OFDM symbol or equivalently, index of the block of N_{FFT} element
d_p^k	p-th subcarrier/modulated symbol of the k-th OFDM symbol/N_{FFT} block.
$h(t), H(f)$	Channel impulse response and channel frequency response
H_p^k	Channel frequency response over the p-th subcarrier of the k-th OFDM symbol
$s(t)$	Sent/transmitted signal
n	$\in [-N_{CP}\ N_{FFT} - 1]$ - Sample index in a block of $N_{FFT} + N_{CP}$ samples
l	$\in \mathbb{N}$ - Index of the block of $N_{FFT} + N_{CP}$ samples
s_n^l	n-th sample of the l-th $N_{FFT} + N_{CP}$ block of the transmitted/sent signal
$r(t)$	Received signal
r_n^l	n-th sample of the l-th $N_{FFT} + N_{CP}$ block of the received signal
τ	Timing offset, in sample, between the beginning of the useful part of the OFDM symbol and the beginning of the FFT windows
$\Lambda(m)$	Van-de-Beek metric
Δ_f	Carrier frequency offset (CFO), dimensionless, normalized by the subcarrier spacing
δ_f	Fractional part of the CFO
p_f	Integer part of the CFO
δ_{SCO}	Sampling clock offset
$\mathcal{P}, \mathcal{P}_c, \mathcal{P}_s$	Pilot index set, Continuous pilot index set, Scattered pilot index set
$R(\tau)$	Correlation function
$\hat{\tau}$	Estimated timing offset
ε_τ	Difference between estimated and actual timing offset
T_{symb}	Length, is second, of an OFDM symbol
T_U	Length, in second, of the useful part of the OFDM symbol, i.e. without cyclic prefix
T_{samp}	Sampling period

1 Introduction

1.1 Background and Motivation

The recent years have shown a growing interest in urban and indoor positioning with the development of applications such as car navigation, pedestrian navigation, local search and advertising and others location-based-services (LBS). However, in urban and indoor environment the classical mean of positioning, the GNSS has limited availability, accuracy, continuity and integrity due to signal blockage by building, intense multipath conditions and interferences from the other signals, abundant in metropolitan areas. As a consequence, several solutions have been explored to improve positioning performance in urban and indoor environments:

- **GNSS ameliorations**: this includes (1) receivers ameliorations, such as high-sensitivity receivers [1], advanced multipath mitigation[2–4], multi-constellation receiver, etc, or (2) system-level ameliorations, such as the introduction of new GNSS signals with features particularly interesting for urban and indoor positioning (e.g. BOC modulation more robust to multipath than classical BPSK, longer code, presence of a pilot channel allowing longer integration) and Assisted-GNSS [5] allowing lower C/N0 than classical GNSS.
- **Additional sensors:** inertial sensors, magnetometers, odometers, cameras can be coupled to GNSS [6][7] using, for example, a Kalman filter, to provide a better availability, accuracy, continuity and integrity of the positioning solution. They can even temporary replace GNSS during its unavailability periods using, for example, dead-reckoning techniques.
- **Terrestrial positioning systems:** they are systems deployed especially to provide a positioning service. One can cite pseudo-satellite (a.k.a. pseudolites) systems [8] that emit a GNSS signal to locally extend its coverage, new positioning signal (Locata [9], eLoran [10]), UWB emitters [11], RFID tags [12]. All these systems need the deployment of a specific infrastructure and are generally local.
- **Signals or Systems of Opportunity (SoO):** they are any radio-communication signals present in the air, which are opportunely used to provide a positioning service. It is this type of signals that is explored in this PhD and there are described in detail in the following.

The advantages of SoO for positioning are multiple:

- **Availability:** by definition, SoO are available in any place where a radio-communication signal is available. Thus in particular in indoor and urban areas, since a lot of radio-communication signals are deployed to be accessible in these environments.
- **Diversity of signals:** the number of SoO is immense, especially in urban and indoor environments. Thus, there is a huge diversity in the available modulations, frequency bands, signal bandwidths, types of network, etc.
- **Low cost**: SoO are existing radio-communication signal, they are “freely” available, in the sense of there is no need to an additional infrastructure to provide the positioning service.

Of course, SoO have also some drawbacks:

- **Not designed for a navigation purpose**: since SoO are designed for a communication purpose and not for a navigation purpose they may not have the characteristics required to

provide a positioning service. As an example, for positioning solution based on the estimation of time-of-arrival (TOA), most of radio-communication systems are not time-synchronized with a sufficient precision. However some of the last-generation communication systems require precise time synchronization (accuracy of few nanoseconds).

- **Multipath and non-line-of-sight propagation**: urban and indoor environments are already very challenging for GNSS positioning due to the presence of multipath and signal masking. Furthermore, in terrestrial networks, used for most of the considered SoO, multipath and masking phenomena are even more important, leading to quick and important fading of the received signal and to a non-line-of-sight (NLOS) propagation, which could be a big issue for geometric-based positioning.
- **The telecommunication service is a priority**: consequently, the positioning service using the telecommunication signal has to be thought to not degrade the telecommunication service. This is why generally, SoO are used passively, without impact on the telecommunication service, even some modification of the signal would improve the positioning performance.

1.1.1 State of the art of positioning techniques using SoO

Because of the variety of available SoO, a variety of techniques can be used to provide a positioning service. Depending on the characteristics of the targeted SoO, some positioning techniques are more suited than others. The existing positioning techniques and examples of SoO using these techniques are listed in the following.

1.1.1.1 Cell-id positioning

The cell-id positioning permits a rough location of a mobile station by identifying the in-view emitters. This technique assumes knowledge of emitter positions and its performance depends on the sizes of the emitter cells.

Cell-id positioning is classically used in GSM networks, leading to a positioning error of more than 1 km in average in suburban areas (large cell size) and about 200 meters in average in urban areas (smaller cell size) [13].

1.1.1.2 Signal strength positioning

The principle is to measure the signal strength of a received signal. Then, knowing the emitter position and according to a suitable propagation model, the distance between the mobile and the emitter can be estimated [14]. The precision of the technique depends on the reliability of the propagation model, which is unfortunately not good in urban and indoor environments.

The measurement of the signal strength can be also compared to a database, constructed during a calibration phase and which includes measured and predicted signal strengths in different locations. The estimated position is the position where the measurement fit the database [15]. The main drawback of this technique, also known as fingerprinting, is the cost of construction of the database,

which presents in addition a limited reliability (emitter configuration can evolve after the calibration phase leading to erroneous database contents).

This technique has notably be applied with Wi-Fi signals. They are particularly adapted to this positioning technique because signal strength measurements are already done in a Wi-Fi chipset and Wi-Fi hotspots are unambiguously identifiable through their MAC address and are not synchronized on a reference time. The precision of the positioning solution depends on the precision of the database and on Wi-Fi hotspot density. For example, an indoor experiment using the Ekahau Positioning Engine allows a mean positioning error comprised between 2.5 and 13 meters [16]. A more global outdoor coverage, such as proposed by Skyhook [17] (20 to 30 meters accuracy) or Google (100 meters accuracy) has often a less good precision.

1.1.1.3 Time Of Arrival (TOA)/Time Difference Of Arrival (TDOA) positioning

The main idea of this technique is to measure the time of arrival (TOA), sometimes called time of flight, of a signal. This time corresponds to the travel time of the signal from the transmitter to the receiver. To obtain a correct TOA the transmitter and the receiver have to be synchronized on the same clock, or, at least, the clock difference between emitter and receiver has to be known or estimated. A TOA measurement for the k-th transmitter of a group of emitter can be modeled as following:

$$TOA_k = \left\| r_{\text{rcv}} - r_{\text{trans},k} \right\| + b.c \tag{1.1}$$

where:

- TOA_k is the TOA of the k-th transmitter expressed in meter
- r_{rcv} is the vector of coordinates of the receiver
- $r_{\text{trans},k}$ is the vector of coordinates of the k-th transmitter
- b is the bias between clocks of transmitters and receiver, generally unknown
- c the speed of light

The receiver position determined by trilateration if at least four TOA measurements are available (or only 3 if the clock bias b in known) using, for example, the Non-Linear Least Square algorithm. This is the technique used in GNSS [18].

The TDOA technique is equivalent, but the measurement is the difference between TOAs from two different transmitters of the network. For this technique, the synchronization of the network of transmitters is still required but the difference in timing between emitters and receiver does not have to be estimated anymore. A TDOA measurement obtained from the k-th transmitter can be modeled as following :

$$TDOA_k = \left\| r_{\text{rcv}} - r_{\text{trans},k} \right\| - \left\| r_{\text{rcv}} - r_{\text{trans},0} \right\| \tag{1.2}$$

where:

- $TDOA_k$ is the TDOA of the k-th transmitter, expressed in meter
- r_{rcv} is the vector of coordinates of the receiver
- $r_{\mathrm{trans},k}$ is the vector of coordinates of the k-th transmitter
- $r_{\mathrm{trans},0}$ is the vector of coordinates of the transmitter taken in reference to compute TDOA

Then the receiver position is determined by multilateration, at the intersection of several hyperboloids depending on TDOA measurements, if 3 TDOA measurements (i.e. 4 emitters including reference transmitter).

TOA and TDOA positioning techniques allow the best precision, but it requires a precise synchronization of emitter (1 µs error = 300 meters error) and it is sensitive to multipath. Indeed multipathes result of reflection of the signal on obstacles around the receiver, that travel a longer distance than the direct signal before reaching the receiver. Thus, they may induce important error and the TOA or the TDOA measurement especially in urban and indoor environments. In addition, in those environment and more especially when considering terrestrial networks, the direct signal may even be absent. This induce an even more important error, generally called non-line of sight error. According to [19] this error can be modeled as a uniformly distributed distance comprised between 24.4 and 244 meters or, according to [20] an error constrained between 0m and 1300m and with a standard deviation of 409m.

Examples of SoO using TOA or TDOA techniques are:

- UMTS signals using TDOA technique permit to reach a positioning mean error comprised between 10 meters (rural environment) and 150 meters (urban environment) [13].
- ATSC signal (DTV standard used in north America) allows a positioning mean error from 4 meters (outdoor in direct sight of the TV emitters) to 30 meters (indoor) [21]. However this solution uses a reference station to deal with the non-synchronization of TV emitters.

1.1.1.4 Angle of arrival (AOA)

The measurement of angle of arrival is performed thanks to an antenna array. With at least two measures, a position of the receiver can be computed. The AOA measurement is almost always done by the base stations (BS) (an antenna array is easier to install in a BS that in the mobile receiver). In theory such a technique can be used with any radio signal but it requires a specific architecture of the BS or the receiver (presence of antenna array). In addition this technique is very sensitive to NLOS propagation, since it requires the reception of the LOS signal to obtain a correct estimation of the AOA.

In practice, an accuracy of about 100 meters can be reached [22].

1.1.2 Choice of OFDM modulation and of the DVB-T standard

Among all possible available SoO, this thesis focuses on the popular Orthogonal Frequency Division Multiplexing Modulation (OFDM). The specific reasons to explore the OFDM modulation capability for positioning are multiple:

- OFDM modulation has been chosen by a large number of modern telecommunication and audio/video broadcast standards (Wi-Fi, WiMAX, DAB, T-DMB, DVB-T/H/SH, ISDB-T, LTE…). This preeminence of OFDM-based signals makes them evident candidates to be used as signal-of-opportunity for ranging applications, and good candidates for nav/com services.
- OFDM timing and frequency acquisition is very simple and quick thanks to the presence of a specific redundant component of the OFDM signal called the Cyclic Prefix, contrary to GNSS where a heavy search in the 2D time/frequency space is necessary.
- OFDM signal includes pilot symbols that allows computing correlations between the received signal and a receiver-generated local replica, thus creating the grounds for precise synchronization (similarly to GNSS).
- The robustness of OFDM against multipath authorizes operation in Single-Frequency Networks (SFNs). A SFN is a network where all the emitters send the same signal at the same frequency in a synchronized way (usually based on GPS time and frequency). A SFN can be very useful to extend the coverage of an emitter to isolated/masked areas without requiring additional frequency. From a positioning point-of-view, a SFN is also extremely interesting because it allows tracking multiple signals coming from several synchronized emitters on the same frequency (only 1 tuner required). This synchronization of the emitters is also strength to use TOA/TDOA positioning technique.

To assess the performance of a positioning SoO based solution using the OFDM modulation, a particular signal using this modulation had to be targeted. Thus, the choice of the European standard for digital television, called Digital Video Broadcasting-Terrestrial (DVB-T), has been made for the reasons exposed below. In addition, even if it is not the best candidate for an operational system (particularly it generally has a low emitter density), it can be seen as a potential complement to GNSS-based positioning (DVB-T emitters are sometimes synchronized with GPS time). It is also particularly adapted for testing an OFDM-based ranging:

- The signal definition is very simple (no specific pilot OFDM symbols, classic pilot grid) which makes the reuse of this work possible for other OFDM-based standard.
- It is already deployed and operational (in France and many other countries) which allows tests on real signals, necessary to assess the performance of the ranging technique.
- Both Multi-Frequency Networks (MFN) and Single-Frequency-Network (SFN) are available, thus permitting to test two ranging solutions in the both type of networks.
- It is a wide-band (5 to 8 MHz) and high-power signal that could offer promising ranging accuracy and availability (even indoor).

1.2 Thesis Objectives

The general thesis objective is to investigate the potential of the OFDM modulation to be used as a signal-of-opportunity for positioning, in order to assist or complement GNSS in urban and indoor environments.

Considering the characteristic of the OFDM signal explained in section 1.1.2, especially the presence of a pilot component, the TOA/TDOA positioning technique is logically envisaged. Given the choice of the DVB-T standard as a study case, the first objective is obviously to develop a ranging method using a DVB-T signal, comprising acquisition and tracking modules.

In order to prove the potential of the DVB-T signal (and more generally of the OFDM-based signals) to provide a precise ranging estimation, the second objective is to theoretically derive the performance of the acquisition and of tracking, in an AWGN channel. For that the mathematical models governing the ranging method have to be derived. Of course, the theoretical results have to be validated by simulations.

The third thesis objective is to assess the performance of the ranging method in a real environment. For that a test bench is designed and developed (including hardware and software). This test bench must permit to record DVB-T signal in real environments (indoor and urban), must provide a reference position and must be portable.

1.3 Thesis Contributions

In collaboration with another PhD student [23], a ranging method using DVB-T signal has been developed. This includes acquisition and tracking algorithms adapted to terrestrial multi- and single-frequency networks.

A theoretical analysis of acquisition and tracking performance in Gaussian channel was done. This includes, for the acquisition algorithm, the definition of the detection probability as a function of SNR given a false alarm probability. For the tracking, the expression of the standard deviation of the tracking error and the expression of the tracking threshold have been derived theoretically and validated by simulation.

A flexible test bench, permitting TV signal recording on two reception chains (allowing antenna diversity operations), synchronized of GPS time and providing a reference position has been

developed. Multiple test field campaigns were done in various environments and in two emitter's configurations (MFN and SFN).

All the recorded signals were post-processed using a developed C++ program implementing the conceived ranging method, with different processing parameters, in order to give a final tracking performance and conclude on the feasibility of a positioning solution using SoO based on the ODFM modulation.

The thesis contributions have been published in three communications in international conferences [24–26] and in a technical article of Inside GNSS magazine [27]. In addition, this PhD has contributed to one publication in an international journal [28], to three communications in international conferences [29–31] and to one technical article of Inside GNSS magazine [32].

1.4 Thesis Outline

Chapter 1 describes the OFDM modulation, the mathematical model of an OFDM-based signal and the impact of transmission and receiver impairments in the OFDM demodulation. It also presents the DVB-T standard, including signal parameters and pilot structure, and describes the algorithms of a classical DVB-T receiver that have studied and implemented for this thesis.

Chapter 1 introduces the background of the ranging method using DVB-T signal. This includes a presentation of specificities of terrestrial propagation channels and the description of the acquisition and tracking algorithms. It also presents the theoretical analysis of the performance of acquisition and tracking.

Chapter 1 describes the designed test bench including the hardware part and the software part. It also presents its validation.

Chapter 1 deals with the results of tests on real signal using a DVB-T emitter synchronized on GPS time, in urban and indoor environment. For the urban test two reception antennas are used and the tracking error is analyzed for several tracking configuration. Two novel methods to improve tracking performance are proposed, from the observation of the test on real signals.

Chapter 1 presents the results of tests on real signal using two DVB-T emitters in single-frequency network in suburban and urban areas. The TDOA error is presented in both cases.

Chapter 0 proposes a conclusion and some possible continuations of this work.

2 The Orthogonal Frequency Division Multiplexing (OFDM) Modulation and the ETSI DVB-T Standard

This chapter describes the OFDM modulation, the DVB-T standard and algorithms of a classical DVB-T receiver.

2.1 Orthogonal Frequency Division Multiplexing

2.1.1 OFDM Principle

The concept of OFDM [33] consists in transmitting in parallel N complex data symbols over N orthogonal narrowband subcarriers (1 subcarrier carries 1 symbol). The width of these subcarriers is chosen narrow enough so that the channel frequency response can be considered as flat over the subcarrier bandwidth. The consequence is that channel equalization becomes very simple even in case of dense multipath environment. Thanks to the orthogonality of the subcarriers, their spectra can overlap without interfering with each other, allowing an excellent spectral efficiency and no Inter-Carrier Interference (ICI) when the receiver is synchronized.

An OFDM symbol is obtained by passing the N complex data symbols through an inverse-Fast Fourier Transform (iFFT) operator, as depicted in Eq. (2.1). The useful part of the OFDM symbol is thus composed of N samples. To take advantage of the FFT algorithm N is generally chosen as a power of two.

$$s_n^k = iFFT\left(d_p^k\right)[n] = \frac{1}{N}\sum_{p=0}^{N-1} d_p^k \exp\left(j2\pi\frac{pn}{N}\right), \text{with } 0 \le n \le N-1 \tag{2.1}$$

where:

- n is the sample time index,
- p is the subcarrier index,
- k is the OFDM symbol number,
- d_p^k is the complex data symbol carried by the p-th subcarrier and
- s_n^k is the n-th sample of the k-th OFDM symbol.

Conversely, the demodulation of an OFDM symbol is performed by a direct FFT. In absence of impairments due to transmission and supposing a perfect synchronization of the receiver, this demodulation operation permits to directly recover the transmitted symbols as shown in Eq. (2.2).

$$\begin{aligned}
\tilde{d}_{p'}^{k} = FFT\left(s_n^k\right)[p'] &= \sum_{n=0}^{N-1} s_n^k \exp\left(-j2\pi\frac{np'}{N}\right) \\
&= \frac{1}{N}\sum_{n=0}^{N-1}\sum_{p=0}^{N-1} d_p^k \exp\left(j2\pi\frac{pn}{N}\right)\exp\left(-j2\pi\frac{np'}{N}\right) \\
&= \frac{1}{N}\sum_{p=0}^{N-1} d_p^k \sum_{n=0}^{N-1}\exp\left(j2\pi\frac{n(p-p')}{N}\right) \\
&= \sum_{p=0}^{N-1} d_p^k \delta(p-p') \; = d_{p'}^{k},
\end{aligned} \tag{2.2}$$

Additionally, a guard interval of N_{CP} samples is inserted before the useful part of the OFDM symbol in order to avoid Inter-Symbol Interference (ISI). Most of the time, this guard interval is a replica of the last N_{CP} samples of the OFDM symbol and is then referred to as Cyclic Prefix (CP). By doing so, any demodulation of the OFDM symbol that is done with an N-sample FFT starting in the CP will only result in a phase rotation of each subcarrier proportional to its frequency, thus easily equalized. Thus, a complete OFDM symbol is composed of $N + N_{CP}$ samples. The expression of the transmitted signal s_n^k on Eq. (2.1) can be extended to include the definition of the CP:

$$s_n^k = \frac{1}{N}\sum_{p=0}^{N-1} d_p^k \exp\left(j2\pi\frac{pn}{N}\right), \text{with} - N_{CP} \le n \le N-1 \tag{2.3}$$

As it can be seen on Eq. (2.3), the samples belonging to the cyclic Prefix are represented by negative indexes and:

$$s_n^k = s_{n+N}^k \text{ if } n \in \{-N_{CP}, \dots, -1\} \tag{2.4}$$

To illustrate the OFDM principle, Figure 2.1 shows an OFDM transmission block diagram.

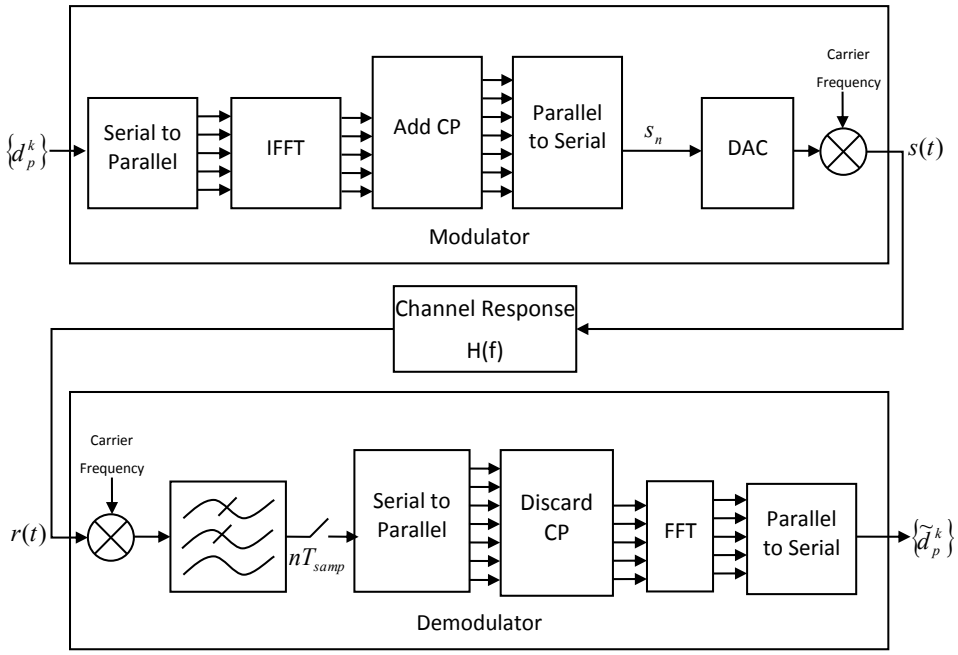

Figure 2.1: OFDM transmission block diagram

The demodulation operation described in Eq. (2.2) supposes that the received signal is equal to the transmitted signal. Unfortunately, in real world, the transmitted signal is affected by the propagation channel and by the receiver imperfections. The impact of these impairments is presented in the next section.

2.1.2 Impact of the transmission chain on the received OFDM signal

The received signal is affected by multiple impairments due to channel propagation (frequency selectivity, time dispersivity, propagation delay, Doppler effect…) and receiver imperfections (mismatch between emitter and receiver local oscillators and sampling clocks, thermal noise…). To understand the OFDM principle and the related receiver algorithms it is important to analysis the impact of each one of these impairments on the demodulation performance. Thus, in the following subsections, the impact of each source of errors on the demodulated symbols is analyzed, supposing that the other sources are null.

2.1.2.1 Impact of timing offset

To recover properly the transmitted symbol d_p^k, the FFT windows has to start just after the CP, on the first useful sample of the OFDM symbol. Let τ be the timing offset of the position of the FFT windows compared to its ideal position, that is to say the first sample after the CP (see illustration of the timing offset on Figure 2.2). The value of the timing offset τ is dimensionless, normalized by the sampling period. The timing offset τ is defined positive when the FFT windows is in the cyclic prefix, in order to have a correspondence in the variation of the timing offset and the propagation delay (i.e. when the propagation delay augments, the timing offset augments).

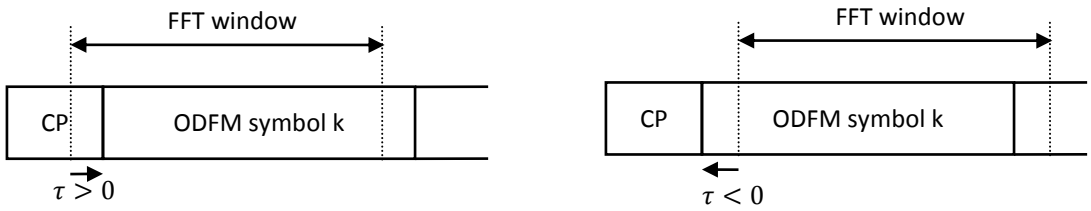

Figure 2.2: Timing offset illustration

To analyze the impact of the timing offset τ, two cases have to be considered, as illustrated on Figure 2.3:

- the FFT windows starts in the "safe zone"
- the FFT windows starts in the "ISI zone"

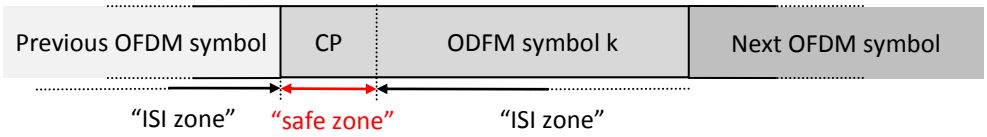

Figure 2.3: "Safe zone" and "ISI zone" illustration

FFT starts in the "safe zone":

In the "safe zone" the beginning of the FFT windows is inside the cyclic prefix. Thus, when the FTT windows start in the "safe zone" the FTT operates only on samples from one OFDM symbols. The mathematical expression of the "safe zone" is presented on Eq. (2.5).

$$\tau \in [0, N_{CP}] \tag{2.5}$$

The expression of the demodulated symbols when the timing offset is the "safe zone" is shown on Eq. (2.6) [34].

$$\tilde{d}_p = d_p \exp\left(-j2\pi \frac{\tau p}{N}\right) \tag{2.6}$$

Thus, according to Eq. (2.6), when the timing offset is such that the FFT windows starts in the "safe zone", the p-th demodulated subcarrier is rotated by a phase depending on the timing offset and the subcarrier number. However, we will see later that this phase could be corrected by channel equalization.

FFT starts in the "ISI zone":

In the "ISI zone" the FFT window contains contribution of two consecutive OFDM symbols. The mathematical expression of the "ISI zone" is presented on Eq. (2.7).

$$\tau \notin [0, N_{CP}] \tag{2.7}$$

When the timing offset is in the "ISI zone", a demodulated symbol is affected by 3 different effects that induce a SNR degradation at the FFT output:

- an attenuation of the magnitude of the demodulated symbol, since in the FFT window some samples do not belong to the desired OFDM symbol and so do not represent useful power,
- an apparition of ISI, due to the presence in the FFT windows of samples coming from the previous or the next OFDM symbol and,
- an apparition of ICI, resulting from a loss of orthogonality due to an FFT not made on the whole OFDM symbol.

According to [35], if the timing offset τ is small compared to the FFT size N, the attenuation of the expected demodulated symbol is negligible and the power of the ICI and ISI, for an unitary power of the useful signal ($P_U = 0\ dB$), is:

$$P_{ICI+ISI} = \frac{2N_\tau}{N} - \frac{{N_\tau}^2}{N^2} \tag{2.8}$$

where

- $N_\tau = \begin{cases} \lfloor \tau \rfloor, \text{if } \tau \leq 0 \\ \lfloor \tau - N_{CP} \rfloor, \text{if } \tau > N_{CP} \end{cases}$ represents the number of samples in the FFT windows that are belonging to the previous or the next OFDM symbol, and
- $\lfloor x \rfloor$ is the largest previous integer of x

The power of the noise induced by a FTT window misplaced in the "ISI zone", as a function of the timing offset, is showed on Figure 2.4. The power of the useful signal is supposed unitary ($P_U = 0\ dB$), $N = 4096$ and the simulated results are obtained over 200 OFDM symbols. The results, shown for a positive timing offset, would be similar for a negative timing offset in the "ISI zone".

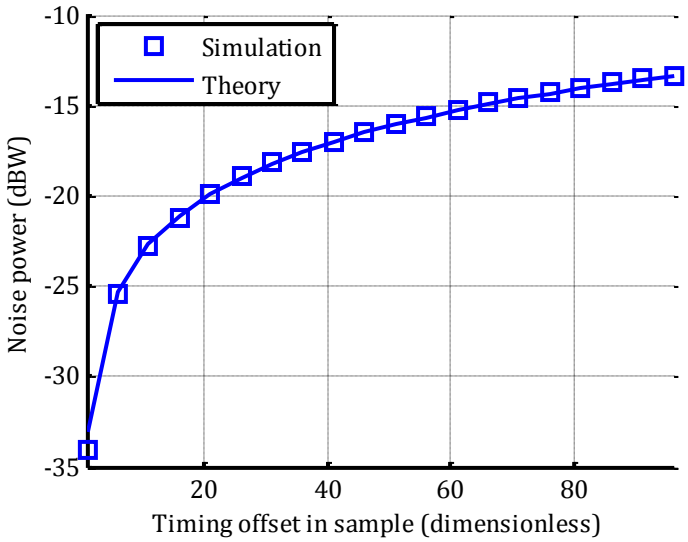

Figure 2.4: Noise power due to timing offset in the "ISI zone" ($P_U = 0\ dBW$, $N = 4096$)

Such a noise power can be very problematic. For example, in a DTV system using the DVB-T standard, for which the required SNR for receive TV is around 15 dB, an additional noise of -15 dBW on a useful signal with a 0 dBW power, due to a timing offset in "ISI zone" of 60 samples, leads to a SNR degradation of 3 dB.

Thus, a timing synchronization that positions the FFT window in the "safe zone" is essential to ensure a good demodulation. It is also important to note that in multipath channel the "safe zone" in reduced because of the spreading of the previous symbol in the CP. This case will be studied more in detail in the subsection 2.1.2.4.

2.1.2.2 Impact of carrier frequency offset (CFO)

Due to Doppler effect and the difference between the local oscillator frequencies of transmitter and receiver, the baseband received signal is modulated by a residual frequency offset f_d. Then the complex envelop of the received baseband signal is:

$$r(t) = s(t)\exp(j2\pi f_d t) \tag{2.9}$$

The CFO, denoted Δ_f, is defined as the residual frequency offset f_d normalized by the subcarrier spacing as expressed on Eq.(2.10).

$$\Delta_f = f_d T_U = f_d T_{samp} N \tag{2.10}$$

where:

- T_U is the duration of the useful part of an OFDM symbol (i.e. CP excluded)
- T_{samp} is the sampling period

To study its impact on the demodulation, the CFO Δ_f can be decomposed in a fractional component δ_f and an integer component p_f, as defined in Eq. (2.11).

$$\Delta_f = \delta_f + p_f, \text{ with } \delta_f \in]-0.5,0.5] \text{ and } p_f \in \mathbb{N} \tag{2.11}$$

Impact of integer CFO

In this case δ_f is supposed null. After performing standard manipulation, it can be shown [36] that the presence of integer CFO results in a shift of the index of the modulated symbol by p_f and in a phase rotation of the modulated symbol depending on the OFDM symbol index:

$$\tilde{d}_p^k = d_{\lfloor p-p_f \rfloor_N}^k \exp\left(j2\pi k p_f \frac{N_t}{N}\right) \tag{2.12}$$

where:

- $\lfloor p - p_f \rfloor_N = (p - p_f)\ mod\ N$
- $N_t = N + N_{CP}$ the number of samples in the whole OFDM yylbol (including CP)

Thus, in order to recover the transmitted symbol d_p^k, the integer CFO has to be estimated and its impact has to be corrected, but since its does not induce additional noise on the demodulated symbol, this estimation and correction can be done after the FFT demodulation block.

Impact of fractional CFO

In this case p_f is supposed null. After performing standard manipulation, it can be shown [36] that the presence of fractional CFO results in a attenuation and phase rotation of the modulated symbol depending on the OFDM symbol index and in an additional noise referred to as ICI :

$$\tilde{d}_p^k = d_p^k \frac{\sin(\pi\delta_f)}{N \sin\left(\pi \frac{\delta_f}{N}\right)} \exp\left(j\pi\delta_f \frac{N-1}{N}\right) \exp\left(j2\pi k\delta_f \frac{N_t}{N}\right) + ICI(\delta_f) \tag{2.13}$$

[36] gives an expression of the power the ICI term for small value of the fractional CFO:

$$P_{ICI} = \frac{(\pi\delta_f)^2}{3} \tag{2.14}$$

The Figure 2.5 represents the ICI power in presence of small fractional CFO. The power of the useful signal is supposed unitary ($P_U = 0\ dB$), $N = 4096$ and the simulated results are obtained over 200 OFDM symbols.

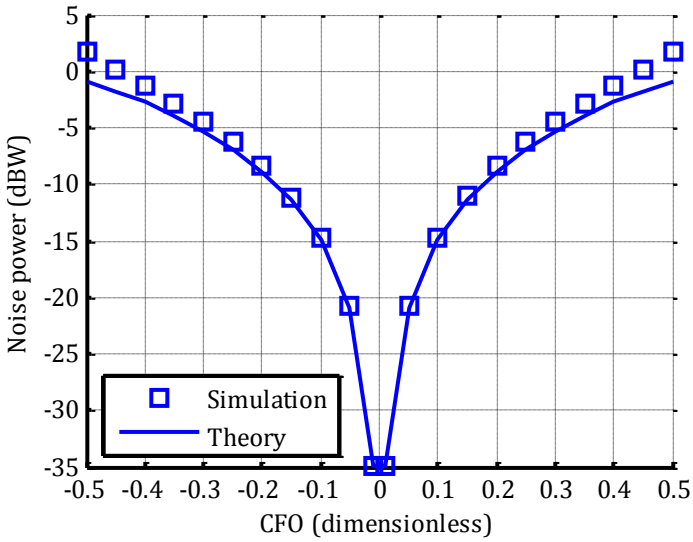

Figure 2.5: Noise power due to fractional CFO ($P_U = 0\ dBW$, $N = 4096$)

As it can be seen on the previous plot that fractional CFO can bring an important noise on the demodulated symbols. Consequently, the estimation and correction of the fractional CFO has to be done before demodulation (i.e. before the FFT operation), that is to say on the raw signal just after the ADC.

To sum up, the presence of Carrier Frequency Offset on the received signal results in two principal impairments:

- Integer CFO: shift of the modulated symbol index. No additional noise on the demodulated symbol. Estimation and correction after demodulation are possible.

- Fractional CFO: Additional noise on the demodulated symbol. Estimation and correction before demodulation are necessary.

2.1.2.3 Impact of sampling clock offset (SCO)

The sampling clock offset (SCO), denoted δ_{SCO}, is due to Doppler effect and mismatch between emitter and receiver sampling clock frequencies. It is often expressed in part per million (ppm) such as 1 ppm corresponds to a drift of 1 µs/s between the ideal and the receiver sampling clocks. Its mathematical expression is:

$$\delta_{SCO} = \frac{T_{samp} - T_{samp,r}}{T_{samp}} \tag{2.15}$$

where:

- T_{samp} is the ideal sampling period to correctly demodulate the received signal and
- $T_{samp,r}$ is the real sampling period of the receiver

The effect of SCO is quite similar to fractional CFO with the difference that the impairment depends on the subcarrier index p [34]:

$$\tilde{d}_p^k = d_p^k \frac{\sin(\pi\delta_{SCO}p)}{N\sin\left(\pi\frac{\delta_{SCO}}{N}p\right)} \exp\left(j\pi\delta_{SCO}\frac{N-1}{N}p\right) \exp\left(j2\pi k\delta_{SCO}\frac{N_t}{N}p\right) + ICI(\delta_{SCO}, p) \tag{2.16}$$

Again similarly to the fractional CFO case the expression on the ICI power induced by SCO is [34]:

$$P_{ICI} = \frac{(\pi\delta_{SCO}p)^2}{3} \tag{2.17}$$

What is important in Eq. (2.13) is that the ICI power is proportional to the square of the subcarrier index p. Consequently, systems with a large number of subcarrier will be more vulnerable to SCO. However, the value of the SCO is often small enough to limit the ICI power. As an illustration Figure 2.6 shows the ICI power as a function of the subcarrier index for SCO of 10 ppm and 50 ppm (classical values for quartz oscillators) for 100 independent realizations. In this example $N = 4096$.

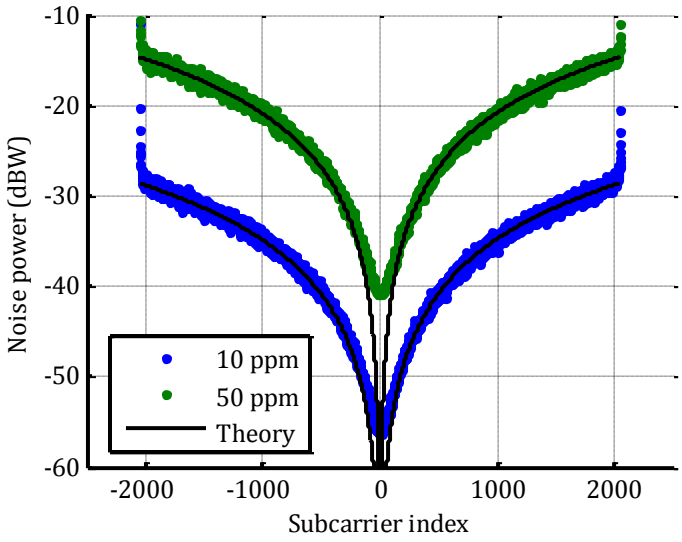

Figure 2.6: Noise power due to SCO as a function of subcarrier index ($P_U = 0\ dBW$, $N = 4096$)

The power of additional noise on demodulated symbols due to SCO is limited and as a consequence its estimation can be done after the demodulation block.

2.1.2.4 Impact of multipath channel

The impulse response $h(t)$ of a multipath channel can be modeled as:

$$h(t) = \sum_{l=0}^{L-1} \alpha_l \delta(t - \tau_l T_{samp}) \tag{2.18}$$

where:

- L is the number of multipath,
- α_l is the complex attenuation of the l-th multipath and
- τ_l is the delay, relative to the sample period, of the l-th multipath.

Thus the received signal is:

$$r(t) = s(t) * h(t) \tag{2.19}$$

The introduction of the multipath channel results in two distinct phenomena, time dispersivity and frequency selectivity, which have each different impact on demodulation.

Time dispersivity

The time dispersivity implies that an OFDM symbol "overflows" on the following OFDM symbol. Consequently the "safe zone" of the timing offset is reduced, as shown on Figure 2.7. This diagram illustrates also the necessity to have a size of the CP longer than the maximum delay of the multipath channel, in order to have a safe zone sufficiently big compared to the precision of the timing synchronization algorithm. As long as the timing offset is kept in the safe zone, no noise is added on the demodulated symbols.

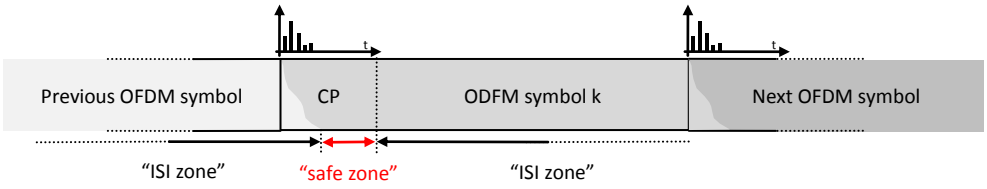

Figure 2.7: Illustration of time dispersivity due to multipath channel

Frequency selectivity

Let $H(f)$ be the frequency response of the multipath channel. It is the Fourier transform of the channel impulse response $h(t)$ and consequently its expression is:

$$H(f) = \sum_{l=0}^{L-1} \alpha_l \exp(j2\pi f \tau_l) \tag{2.20}$$

where:

- f is normalized by the sample frequency ($f = f_{Hz} T_{samp}$)

With basic manipulation [34], it can be shown that the expression of demodulated symbol in presence of multipath channel is:

$$\tilde{d}_p^k = H_p^k d_p^k \tag{2.21}$$

where:

- H_p^k channel frequency response over the p-th subcarrier of the k-th OFDM symbol

According to Eq. (2.21), in presence of multipath channel, the demodulated symbols is equal to the transmitted one multiplied by a complex factor which is the frequency response of the channel over the subcarrier carrying this symbols. Thus, to recover the transmitted symbol this complex factor has to be estimated. As explained in section 2.3.5, it is very easy to do using pilot symbols which value is known by the receiver.

2.2 Digital Video Broadcasting – Terrestrial (DVB-T)

2.2.1 Presentation of DVB-T

The DVB-T [37] is a European standard for digital TV broadcasting to fixed receivers in the VHF and UHF bands and is based on OFDM modulation. DVB-H (Handheld) and DVB-SH (Satellite-to-Handheld) standards, both based on DVB-T, target mobile TV receivers and other potential frequency bands.

These standards define several modes which depend on three parameters: the FFT size (N), the ratio between the Cyclic Prefix length and the useful OFDM symbol length ($CP = N_{CP}/N$) and the sampling period (T_{samp}). Table 2.1 shows different possible values defined in the DVB-T/H/SH standards for each parameter.

Table 2.1: DVB-X mode parameters

Parameters	Possible values		
	DVB-T	DVB-H	DVB-SH
N	2048 and 8192	2048, 4096 and 8192	1024, 2048, 4096 and 8192
CP	1/32, 1/16, 1/8, 1/4	1/32, 1/16, 1/8, 1/4	1/32, 1/16, 1/8, 1/4
T_{samp} (µs)	7/64, 1/8, 7/48 and 7/40	7/64, 1/8, 7/48 and 7/40	7/64, 1/8, 7/48, 7/40 and 35/64

Additional parameters can be derived from the FFT size N and the sampling period T_{samp}. There are the transmission mode equivalent to the FFT size and the approximate bandwidth equivalent to the sampling period. Their values are given in Table 2.2.

Table 2.2: Correspondence between FFT size and sampling period and their equivalents

FFT size	Transmission mode
1024	1K
2048	2K
4096	4K
8192	8K

Sampling Period (µs)	Approximate bandwidth
7/64	8Mhz
1/8	7MHz
7/48	6MHz
7/40	5Mhz
35/64	1.7Mhz

2.2.2 DVB-T subcarrier types

The N subcarriers of an OFDM symbol have different natures. They are:

Null subcarriers:

Null subcarriers are situated on the edges of the signal spectrum and have a zero value. They serve as guard bands to avoid out-of-band emissions of the OFDM signal. The number of null subcarriers, noted N_0, depends on the transmission mode. Null subcarriers are distributed in the lower band on the $N_{0,\text{lower}}$ first subcarriers and in the upper band on the $N_{0,\text{upper}}$ last subcarriers, as detailed in Table 2.3.

Table 2.3: Number of null subcarriers

Transmission mode	Number of null subcarriers N_0	Number of null subcarriers in the lower band $N_{0,\text{lower}}$	Number of null subcarriers in the upper band $N_{0,\text{upper}}$
1K	171	86	85
2K	343	172	171
4K	687	344	343
8K	1375	688	687

Data subcarriers:

Data subcarriers carry the useful information. In the case of DVB-T, the useful information is the TV broadcast (MPEG-2 multiplex) interleaved and coded to improve its robustness. The data bits are mapped on 7 possible constellations detailed on Table 2.4. The amplitude of the data subcarriers is normalized so their average power is unitary. The normalization factor, different for each type of constellation, is also given on Table 2.4.

Table 2.4: Possible mapping constellations and their normalization factor

Constellation name	Constellation points ($z = n + j.m$)	Normalization factor
QPSK	$n, m \in \{-1,1\}$	$1/\sqrt{2}$
16-QAM	$n, m \in \{-3,-1,1,3\}$	$1/\sqrt{10}$
Non-uniform 16-QAM	$n, m \in \{-4,-2,2,4\}$	$1/\sqrt{20}$
Non-uniform 16-QAM	$n, m \in \{-6,-4,4,6\}$	$1/\sqrt{52}$
64-QAM	$n, m \in \{-7,-5,-3,-1,1,3,5,7\}$	$1/\sqrt{42}$
Non-uniform 64-QAM	$n, m \in \{-8,-6,-4,-2,2,4,6,8\}$	$1/\sqrt{60}$
Non-uniform 64-QAM	$n, m \in \{-10,-8,-6,-4,4,6,8,10\}$	$1/\sqrt{108}$

Transmission Parameter Signaling (TPS) subcarriers:

TPS subcarriers carry information about the transmission such as data constellation map, code rates, transmission mode, CP length… A complete TPS message is constituted by 68 bits which are transmitted over 68 consecutive OFDM symbols, one TPS bit by OFDM symbol, using a differential BPSK modulation. Each TPS bit, is transmitted redundantly over N_{TPS} subcarriers of the OFDM symbol, such as every TPS subcarrier transmits the same differentially encoded TPS bit. The differential BPSK modulation is initialized according the value of a PRBS sequence (see Eq. (2.22)) at each beginning of a TPS message. The value of N_{TPS} depends on the transmission mode, as detailed on Table 2.5.

Table 2.5: Number of TPS subcarrier for each transmission mode

Transmission mode	Number of TPS subcarriers (N_{TPS})
1K	7
2K	17
4K	34
8K	68

Pilot subcarriers:

Pilot subcarriers have values known by the receiver and are useful for several synchronization processes necessary to demodulate correctly an OFDM symbol. The pilot subcarriers are BPSK-

modulated and are transmitted with a boosted amplitude by a 4/3 factor. In an OFDM symbol several subcarriers are carrying a pilot symbol and their value are derived from a Pseudo-Random Binary Sequence (PRBS) $\{w_p\}$ defined in the DVB-T standard, as shown on Eq. (2.22).

$$d_p^k = \frac{4}{3}\left(1 - 2w_{p-N_{0,\text{lower}}}\right), p \in \mathcal{P}^k \tag{2.22}$$

where:

- $\mathcal{P}^k$ is the set of index of pilot subcarriers in the k-th OFDM symbol
- $w_p \in \{0,1\}$ is th p-th element of the PRBS. The polynomial generator of this PRBS is : $X^{11} + X^2 + 1$
- $N_{0,\text{lower}}$ is the number of null subcarriers in the lower band

The pilot index set $\mathcal{P}^k$ is decomposed in 2 subsets:

- **Scattered pilot** set, ${\mathcal{P}_S}^k$, in which pilots are regularly spaced but whose positions differs from an OFDM symbol to another according to the Eq. (2.23). This configuration leads to 4 different patterns of scattered pilot indexes which are repeated every 4 OFDM symbols (i.e. the OFDM symbol k and the OFDM symbol $k + 4$ have the same pattern of scattered pilots indexes).

$${\mathcal{P}_S}^k = \left\{p \in [\![N_{0,lower}\, N - N_{0,upper}]\!] \mid p = 3\left((k-1)\bmod 4 + 1\right) + N_{0,lower} + 12q\,, q \in \mathbb{N}\right\} \tag{2.23}$$

- **Continuous pilot** set, $\mathcal{P}_C$, in which pilots are not regularly space, but at a fix position from an OFDM symbol to another. The positions of continuous pilot subcarriers are defined in the standard.

Figure 2.8 shows an illustration of scattered and continuous pilots and Table 2.6 gives for each transmission mode the number of continuous and scattered pilot subcarriers per OFDM symbol.

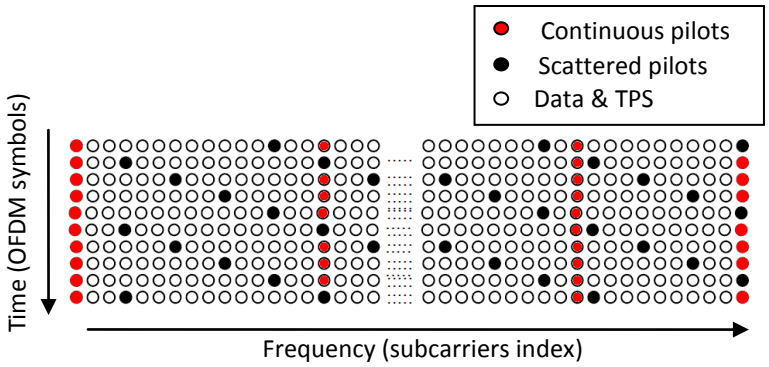

Figure 2.8: Pilot organization

Table 2.6: Number of scattered and continuous pilot subcarriers

Transmission mode	Number of scattered pilot subcarriers	Number of continuous pilot subcarriers
1K	71	25
2K	142	45
4K	284	89
8K	568	177

Figure 2.9 shows the four type of subcarrier in the complex plan.

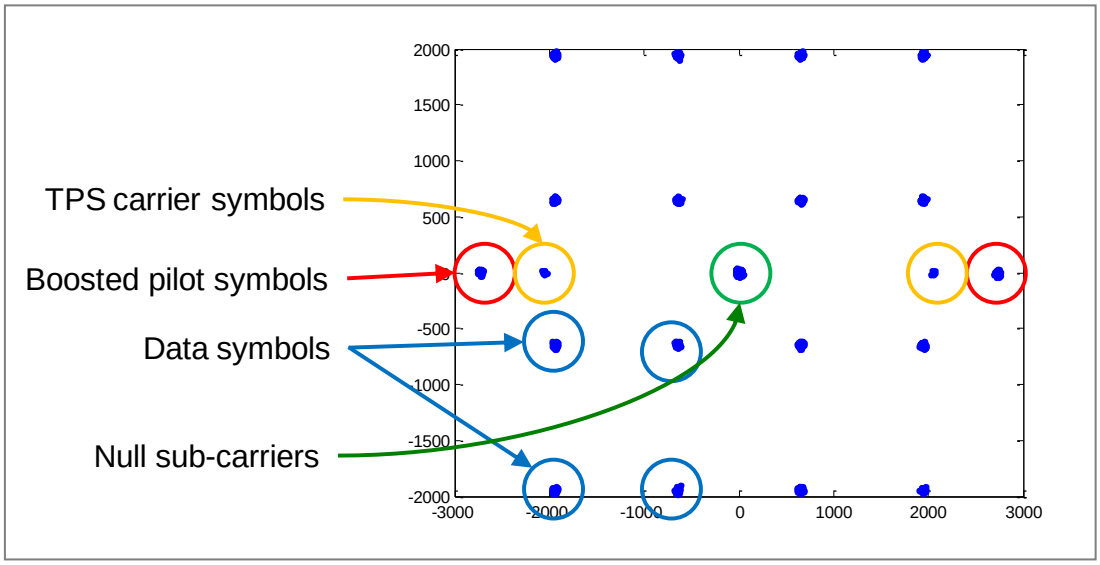

Figure 2.9: Different natures of subcarriers [30]

2.2.3 DVB-T in France

In France where the real signal tests were done, the DVB-T is the standard chosen by the authorities for the national terrestrial digital television. The deployment began in 2005 and is today fully operational in almost all the country. The parameters retained for the French DVB-T are presented in Table 2.7.

Table 2.7: DVB-T parameters in France

Mode – FFT size	8K - 8192
Approximate bandwidth – Sampling period	8Mhz – 7/64 µs
CP ratio	1/8
Data symbols constellation	64-QAM
Possible central frequencies in UHF band	$474\text{Mhz} + (k-21).8\text{Mhz} + f_{\text{offset}}$

where:

- $k \in \{21, \dots, 69\}$ is the channel number
- $f_{\text{offset}} = 166.667$ kHz a spectrum protection offset

In addition the two possible types of network, Multi-Frequency Network and Single Frequency Network, are available. For the SFN, the configuration is often a main regional emitter with multiple local emitters for fill hole in the coverage of the principal emitter, even if some small SFNs with emitters having similar emitting powers also exist.

2.3 Algorithms of a DVB-T receiver

As explained on section 2.1.2, several impairments introduced by the transmission chain (propagation channel and receiver imperfections) have to be estimated and corrected by the receiver in order to properly demodulate the received signal. Depending on the nature of the received signal, a large number of estimation and correction algorithms are available and even for a same type of signal, several algorithms are possible. Instead of giving an exhaustive list of all existing algorithms used in an OFDM receiver, this section intends to describe only the algorithms chosen for the developed DVB-T software receiver and even if some of these algorithms can be used for other OFDM signal they mainly concern DVB-T.

The estimation performance of each algorithm using a simulated DVB-T signal are provided here with the following parameters:

Table 2.8: DVB-T parameters used for the performance study

FFT size -Transmission mode	4096 - 4K
Sampling Period - Approximate Bandwidth	7/64 µs - 8 MHz
Cyclic Prefix ratio	1/8
Constellation	16-QAM

2.3.1 Timing offset and fractional CFO estimation

Estimation

As explained in section 2.1.2.1, the estimation of the timing offset and of the fractional CFO has to be done before the demodulation FFT, on the received samples. The chosen algorithm, is based on the Van de Beek algorithm [38] which takes advantage of the redundancy between the CP and the end of the OFDM symbols to determine the timing offset and the fractional CFO. The metric used to estimate those 2 parameters is:

$$\Lambda(m) = \frac{1}{N_{CP}} \sum_{n=m}^{N_{CP}+m-1} r_n r_{n+N}^{*} \ , m \in [0, N-1] \tag{2.24}$$

with:

- r_n the n-th the received sample

According to [38], the estimate of the timing offset $\hat{\tau}$ and the estimate of the fractional CFO $\hat{\delta}_f$ are presented on Eq. (2.25) and Eq. (2.26).

$$\hat{\tau} = \arg\max_{\mathrm{m}}(|\Lambda(m)|) \tag{2.25}$$

$$\hat{\delta}_f = -\frac{1}{2\pi}\,\mathrm{angle}\big(\Lambda(\hat{\tau})\big) \tag{2.26}$$

Furthermore, in order to improve the estimation performance, an averaged metric, described on Eq. (2.27), can be used instead of the metric of Eq. (2.24) by averaging it over consecutive OFDM symbols.

$$\Lambda^{N_{vdb}}(m) = \frac{1}{N_{vdb}} \sum_{k=0}^{N_{vdb}-1} \Lambda_{\mathrm{k}}(m) \tag{2.27}$$

where :

- $\Lambda_k(m) = \Lambda(m + kN_t)$
- N_{vdb} is the number of averaged metric

Figure 2.10 and Figure 2.11 show the standard deviation of the estimated timing offset and fractional CFO as a function of SNR for 2 averaging summation number values (1 and 10). The DVB-T parameters of Table 2.8 are used. The timing offset estimation is valid for SNR above -6 dB for 1 summation and -10 dB for 10 summations. For these SNR the standard deviation of the timing offset estimation error is about 30 samples. In this zone where the timing offset estimation is valid, the standard deviation of the estimated fractional CFO is about 0.01, which corresponds, according the signal parameters, to a value of 22 Hz.

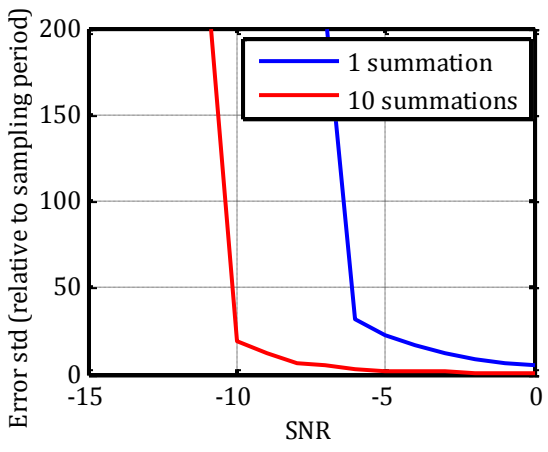

Figure 2.10: Standard deviation of the timing offset estimation as a function of SNR for 2 summation numbers

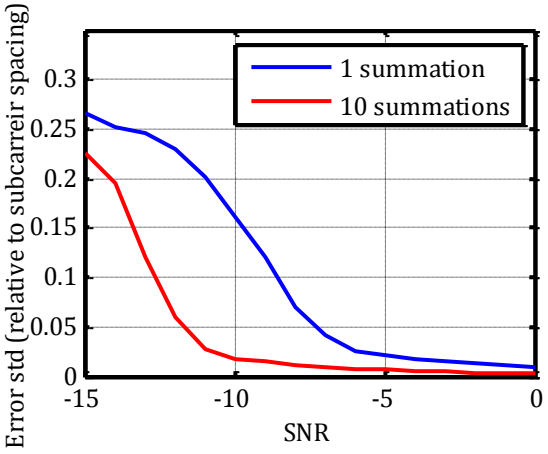

Figure 2.11: Standard deviation of the fractional CFO estimation as a function of SNR for 2 summation numbers

Correction

Thanks to the value of the estimated timing offset $\hat{\tau}$, the FFT can be computed on samples belonging to a same OFDM symbol. In addition, the estimated timing offset is shifted by a margin τ_{margin} to position the start of the FFT window inside the cyclic prefix and thus avoid ISI. Thus timing offset estimator becomes:

$$\hat{\tau} = \arg\max_{\mathrm{m}}(|\Lambda(m)|) - \tau_{margin} \tag{2.28}$$

The phase rotation induced on the demodulated symbol by this shift of the FFT windows of τ_{margin} samples, is compensated in frequency domain in the following way (see Eq. (2.6)):

$$\widetilde{d_p^k} = FFT(\{r_n^k\})[p].\exp\left(j2\pi\frac{\tau_{margin}p}{N}\right) \tag{2.29}$$

where:

- $\{r_n^k\}$ is the N-sized vector of received samples on which is applied the FFT,
- $\widetilde{d_p^k}$ is the p-th demodulated symbol of the k-th OFDM symbol and
- τ_{margin} is the FFT window margin. Its value is arbitrary and set to $\frac{N_{CP}}{4}$.

Then, thanks to the value of the estimated CFO, the frequency offset is directly corrected by multiplying the received samples by the appropriate complex exponential.

2.3.2 Integer CFO estimation

Estimation

As explained in the section 2.1.2.2, the effect of an integer CFO is a circular permutation of indexes of demodulated symbols. The algorithm used in the DVB-T software receiver to estimate the integer CFO, compares several permutations of continuous pilot subcarrier indexes and keeps the permutation that yields the maximum value of the metric of Eq. (2.30).

$$F(g) = \sum_{p\in\mathcal{P}_C} \tilde{d}^k_{(p+g)_{N_{FFT}}}\left(\tilde{d}^{k+1}_{(p+g)_{N_{FFT}}}\right)^* \tag{2.30}$$

where

- $(p+g)_{N_{FFT}}$ denotes the value of $p+g$ modulo N_{FFT}
- $\mathcal{P}_c$ the continuous subcarrier index set

The product of 2 consecutive OFDM symbols is used to mitigate the effect of the channel (which is considered as stable over 2 consecutive symbols)

Thus the estimate of the integer part of the CFO is:

$$\hat{g} = \arg\max_{g}|F(g)| \tag{2.31}$$

Here again the metric can be averaged over several consecutive symbols to improve estimation performance by reducing noise.

Figure 2.12 shows the estimation error rate as a function of SNR for 2 averaging summation number values (1 and 10). The DVB-T parameters of Table 2.8 are used. For 1 summation and above a SNR of about -5 dB, the error rate is quasi null. For 10 summations the SNR threshold is about -10 dB.

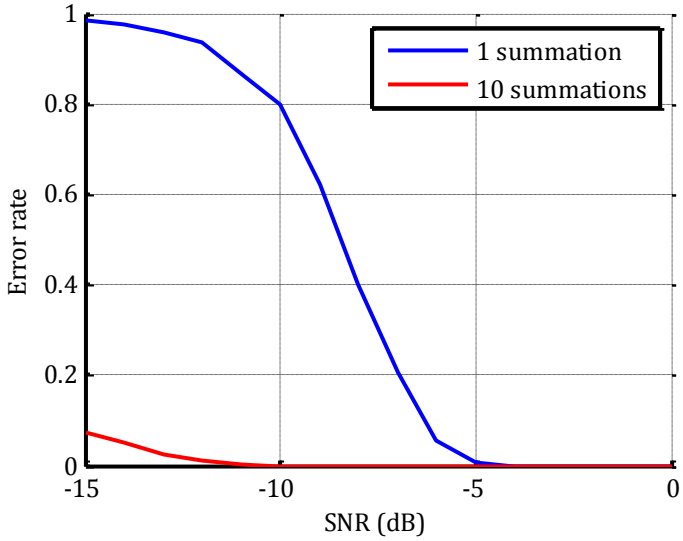

Figure 2.12: Error rate of the integer CFO estimation as a function of SNR for two summation number values

Correction

The effect of integer CFO is corrected in the same way that in the fractional CFO case, by multiplying the received samples by a complex exponential at the appropriate frequency.

2.3.3 Scattered sequence identification

As explained in section 2.2.1, there are 4 possible patterns of scattered pilot indexes, repeating every 4 OFDM symbols. Thus, to use the scattered pilots it is necessary to estimate which one of the 4 possible patterns is used by the current OFDM symbol. The algorithm that estimates the scattered pilot pattern id. exploits this redundancy of the pattern, by looking for the similitude between 2 OFDM symbols spaced by 4, over the subcarriers of the 4 possible scattered pilot patterns. Mathematically the metric used in this algorithm is:

$$S(m) = \sum_{p \in \mathcal{P}_S^m} \widetilde{d_p^k} \left(\widetilde{d_p^{k+4}} \right)^* , m \in \{0,1,2,3\} \tag{2.32}$$

where:

- $\mathcal{P}_S^m$ is the m-th scattered pilot pattern and

- $m \in \{0,1,2,3\}$ the 4 possible scattered pilot pattern numbers

Thus, the estimate of the scattered pilot pattern number (between the 4 possible values) is:

$$\hat{m} = \arg\max_{s} |S(m)| \tag{2.33}$$

Here again, the metric can be averaged over several consecutive OFDM symbols to improve estimation performance by reducing noise.

Figure 2.13 shows the estimation error rate as a function of SNR for 2 averaging summation number values (1 and 10). The DVB-T parameters of Table 2.8 are used. For 1 summation and above a SNR of about -7 dB, the error rate is quasi null. For 10 summations the SNR threshold is about -12 dB.

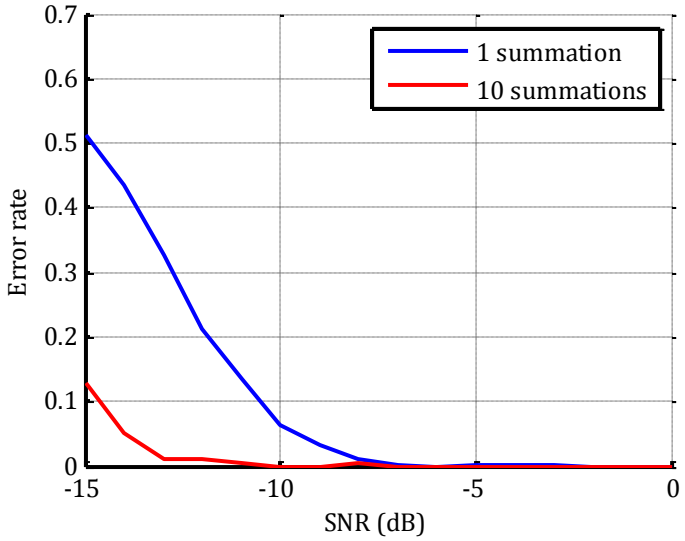

Figure 2.13: Error rate of the scattered sequence number estimation as a function of SNR for two summation number values

2.3.4 Joint SCO and residual CFO estimation

The residual CFO that remains after estimation and correction of fractional CFO thanks to Van de Beek algorithm (see section 2.3.1) and the SCO can be estimated in a joint algorithm.

Estimation

This algorithm, presented in [34], computes the phase difference between the demodulated symbols over the continuous pilot subcarriers of 2 consecutive OFDM symbols. This phase difference is:

$$\theta_p^k = \text{angle}\left(\widetilde{d_p^{k+1}}.\widetilde{d_p^{k}}^*\right) \tag{2.34}$$

where:

- θ_p^k denotes the phase difference between the p-th subcarrier of the k-th OFDM symbol and the p-th subcarrier of the k+1-th OFDM symbol

If we suppose that the channel frequency response is stable over 2 consecutive OFDM symbols, the phase difference observed on the continuous pilot subcarrier (whose value is the same from an OFDM symbol to another) only depends on values of residual CFO and SCO. Thus according to the effect of the fractional CFO and SCO on demodulated subcarrier presented on sections 2.1.2.2 and 2.1.2.3, the estimates of SCO and residual CFO can be obtained as:

$$\hat{\delta}_{SCO} = \frac{N}{2\pi(N+N_{CP})} \frac{\overline{\boldsymbol{\theta p}} - \overline{\boldsymbol{\theta}}.\overline{\boldsymbol{p}}}{\overline{\boldsymbol{p^2}} - \overline{\boldsymbol{p}}^{\boldsymbol{2}}} \tag{2.35}$$

$$\widehat{\delta_f} = \frac{N}{2\pi(N+N_{CP})} \left(\overline{\boldsymbol{\theta}} - \hat{\delta}_{SCO}\overline{\boldsymbol{p}}\right) \tag{2.36}$$

where:

- $\overline{\boldsymbol{\theta p}} = \sum_{p\in\mathcal{P}_C} \theta_p^k.p$
- $\overline{\boldsymbol{\theta}} = \sum_{p\in\mathcal{P}_C} \theta_p^k$
- $\overline{\boldsymbol{p}} = \sum_{p\in\mathcal{P}_C} p$
- $\overline{\boldsymbol{p^2}} = \sum_{p\in\mathcal{P}_C} p^2$
- $\mathcal{P}_c$ the continuous subcarrier index set

Here again, the metric of Eq. (2.34) can be averaged over several consecutive OFDM symbols to improve estimation performance by reducing noise.

Figure 2.14 and Figure 2.15 show the mean values of the estimates of SCO and fractional CFO as a function of SNR for 2 averaging summation number values (1 and 10). The DVB-T parameters of Table 2.8 are used. In this example the CFO value is 0.01 and the SCO value is 10 ppm. From these figures it is clear that the joint estimation of CFO and SCO is only valid for SNR above about 0 dB whatever the number of summations. For lower SNR the metric of Eq. (2.34) is too noisy and do not permit a good estimation of CFO and SCO.

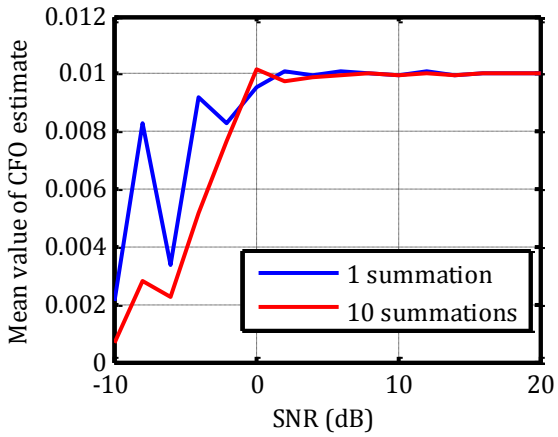

Figure 2.14:Mean value of CFO estimate as a function of SNR for 2 summation numbers

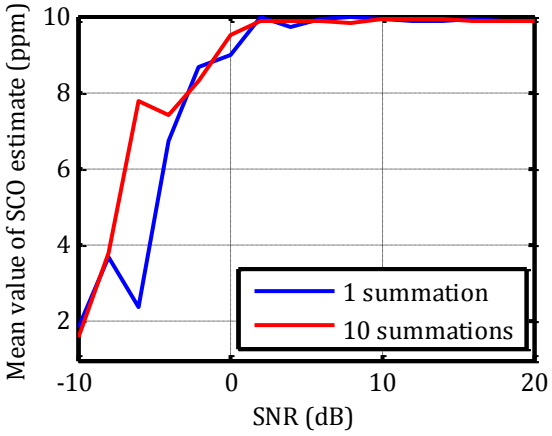

Figure 2.15: Mean value of SCO estimate as a function of SNR for 2 summation numbers

Figure 2.16 and Figure 2.17 show the standard deviation of the estimates of SCO and fractional CFO for SNR in the valid range (above 0 dB) and for 2 averaging summation number values (1 and 10). The estimation of the CFO is quite precise and better than the estimation made with the CP (see section 2.3.1). The estimation of SCO is not as good at 0 dB (classical encountered SCO are around 10 ppm) but for higher SNR it is better. In both case, the use of summation improves significantly the parameters estimation.

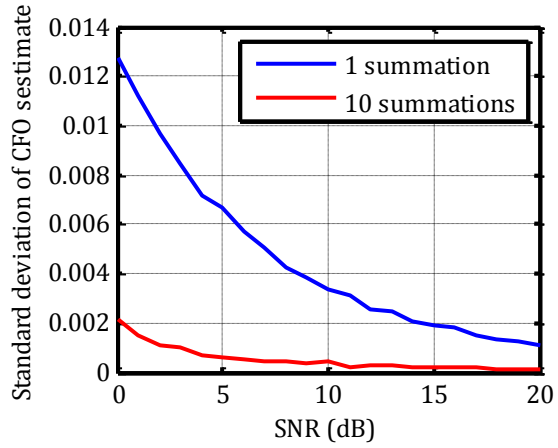

Figure 2.16:Standard deviation of CFO estimate as a function of SNR for 2 summation numbers

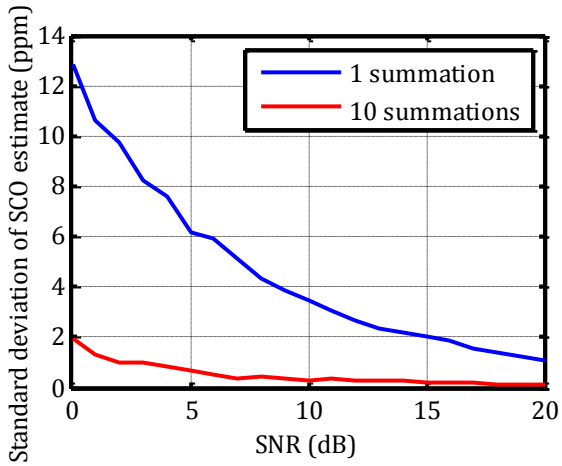

Figure 2.17: Standard deviation of SCO estimate as a function of SNR for 2 summation numbers

Correction

The effect of residual CFO is corrected as the fractional CFO, by multiplication of the received samples by the appropriate complex exponential.

The effect of SCO is corrected by interpolating the received sampled at the corrected sampling period in two steps: oversampling by zero-padded FFT and interpolation at the corrected time vector.

2.3.5 Channel frequency response estimation

Estimation

The channel estimation technique used in the software receiver is very basic, and is made in 2 steps:

- estimation of the channel over pilot subcarriers
- interpolation of this estimation over other subcarriers (linear, cubic or spline interpolation)

Let $\widehat{H_p^k}$ be the estimate of the channel over the p-th subcarrier of the k-th OFDm symbol. Thus, the estimate of the channel over pilot subcarriers is:

$$\widehat{H_p^k} = \frac{\widetilde{d_p^k}}{d_p^k}, p \epsilon \mathcal{P}_c \cup \mathcal{P}_s^k \tag{2.37}$$

where:

- $\mathcal{P}_c$ is the continuous subcarrier index set,
- $\mathcal{P}_s^k$ is the scattered subcarrier index set used in the k-th OFDM symbol,
- $\widetilde{d_p^k}$ is the symbol carried by the p-th demodulated subcarrier of the k-th OFDM symbol (at the FFT output) and
- d_p^k is the symbol transmitted on the p-th subcarrier of the k-th OFDM symbol. Its value is known in the case of a pilot subcarrier.

Then the estimate of the channel over other subcarriers is:

$$\widehat{H_q^k} = \text{interp}(\widehat{H_p^k}, q), q \notin \mathcal{P}_c \cup \mathcal{P}_s$$

where:

- interp is an interpolation function that can be linear, cubic or other.

Figure 2.18 shows the root mean square error of channel estimation as a function of SNR for three interpolation functions (linear, cubic and spline). It can be seen that the three interpolation functions have similar performance below 30 dB SNR where cubic and spline interpolation become better. In all cases, to have a good estimation (RMSE> -5 dB) the SNR has to be above 10 dB.

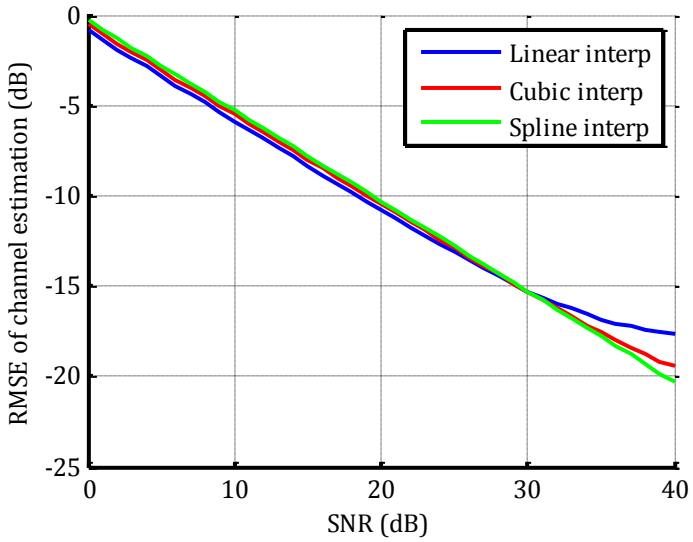

Figure 2.18: RMSE of channel estimation as a function of SNR

Correction:

To perform the channel equalization, the demodulated symbols are simply multiplied by the conjugate of the estimated channel as shown on Eq. (2.38).

$$\widehat{d_p^k} = \widetilde{d_p^k}.\widehat{H_q^k}^*, p \notin \mathcal{P}_c \cup \mathcal{P}_s \tag{2.38}$$

where:

- $\widehat{d_p^k}$ is the equalized symbol,
- $\widetilde{d_p^k}$ is the demodulated symbol (at the FFT output) and
- $\widehat{H_q^k}$ is the estimated channel frequency response.

3 Proposed Pseudo-Range Estimation Method using DVB-T Signals

This chapter concerns the proposed pseudo-range (PR) estimation method using DVB-T signals. The principle of the method is explained in the first section. A second part presents the results of a theoretical analysis of the behavior of the PR estimation method in an AWGN propagation channel, referred as ideal conditions.

3.1 Background of the method

This section presents the background of the PR estimation method introduced in [30]. First, it describes the urban propagation channel that affects DVB-T signal and presents its specificities in the context of the PR estimation method by timing measurement. Then, in the following parts, the PR estimation is presented, beginning by a description of the correlation function computation process and followed by a description of acquisition, tracking and exclusion algorithms. Finally, two techniques to improve correlation operation are presented.

3.1.1 The Propagation Channel

As explained in [23], the urban terrestrial propagation channel is very challenging for a time-based ranging application. Indeed, some particularities of urban propagation channel when terrestrial emitters are used such as strong signal attenuation or a presence of lot of signal replicas with intensive power variation are unusual in the traditional positioning application, GNSS. Indeed, even if urban GNSS navigation can experience difficult multipath conditions, this is nothing compared to the effect of a terrestrial propagation (excepted for low elevation satellite). As pointed out in [23], no model of an urban propagation channel, adapted to a time-based ranging application, was found in the literature. Indeed, since existing models targets telecommunication applications, they present a good modeling of the power variation but a modeling of the multipath delay distribution which is not appropriate for timing measurements.

In [23], exploring the use of a DVB-SH signal-of-opportunity (DVB-SH is a standard based on the DVB-T made for handheld devices, in the 2.2 GHz band and using one satellite and several terrestrial emitters in SFN), an urban propagation channel model, called TU-20 [39] and used for the UMTS mobile cellular technology, was studied, since UMTS works in the same frequency band than DVB-SH. In this model, the multipath delays are fixed whereas the multipath power is following a Rayleigh distribution and has a Jakes spectrum. Thus the expression of the channel model impulse response is:

$$h^k(\tau) = \sum_{n=0}^{L-1} \alpha_l^k . \delta(\tau - \tau_l) \tag{3.1}$$

where:

- k is the OFDM symbol index
- $h^k(\tau)$ is the channel model impulse response at the time of reception of the k-th OFDM symbol
- L is the number of multipath in the model
- α_l^k is the amplitude of the l-th multipath at the time of reception of the k-th OFDM symbol, generated according to the diagram of Figure 3.1
- τ_l is the delay of the l-th multipath

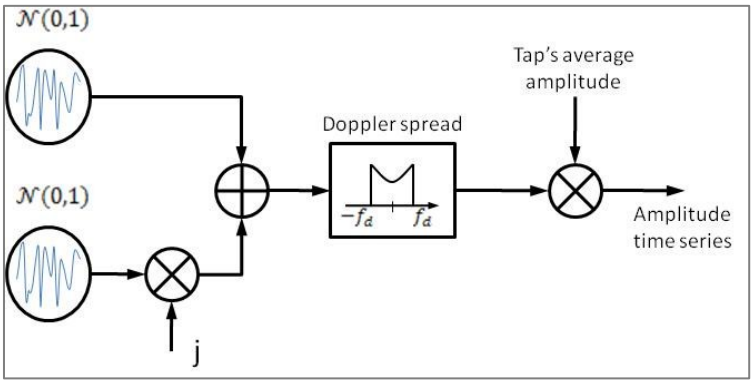

Figure 3.1: Multipath amplitude generation

Unfortunately, the TU-20 model, as all the propagation channel models found on literature, is dedicated to telecommunication and broadcast applications, uses fix multipath delays, which is not a good characteristic for ranging based on timing measurement.

To handle this lack of model, previous work [28] used the output of a measurement campaign realized by the French Space Agency (CNES) to characterize the urban channel for a DVB-SH transmission system. From these parameters, a multipath channel was generated according to the measured multipath delays and simulated multipath amplitudes following a Rayleigh distribution. This channel was applied to a simulated DVB-SH signal and the ranging estimation was done on this semi-simulated signal. This work showed very hopeful results with a ranging error standard deviation of a few tens of meters, and a 2-D positioning accuracy in the range of 30 to 50 meters (Standard deviation) in a middle-sized French city, based on 3 emitters (1 satellite + 2 terrestrial emitters). It appeared during these tests that a significant source of error was coming from the fact that the direct signal was blocked most of the time.

However, even if the generated signals were based on a real measurement campaign, some uncertainties still remained on the employed multipath channel because of hardware constraints

during the measurement campaign (only six multipath delays estimated, limited sensitivity) and doubts on the representativeness of the chosen multipath amplitudes generation.

Thus to confirm the good results obtained in this work, the choice was made to perform tests on real signals based on DVB-T.

3.1.2 Mathematical expression of the correlation function

The pseudo-range estimation method is based on the computation of a correlation between the received signal and a local replica, followed by an acquisition and tracking of the peaks of this correlation function. By doing so it is possible to compute a PR measurement mainly composed of the true distance between emitter and receiver, the emitter and receiver clock difference and multipathes error.

The local replica used to compute the correlation function is only composed of the scattered pilot subcarriers (the other subcarriers are set to zero). Since the pilot values are defined in the frequency domain, the correlation is computed by making the inverse Fourier transform of the product in frequency domain between the demodulated OFDM symbol and a pilot OFDM symbol (the local replica) as illustrated on the diagram of Figure 3.2.

As explained in section 2.2.2, the scattered pilot are present every twelve subcarriers and the index of the first scattered pilot depends on the OFMD symbol number, with a periodicity of 4 OFDM symbols (OFDM symbols k and $k+4$ have the same scattered pilot distribution).

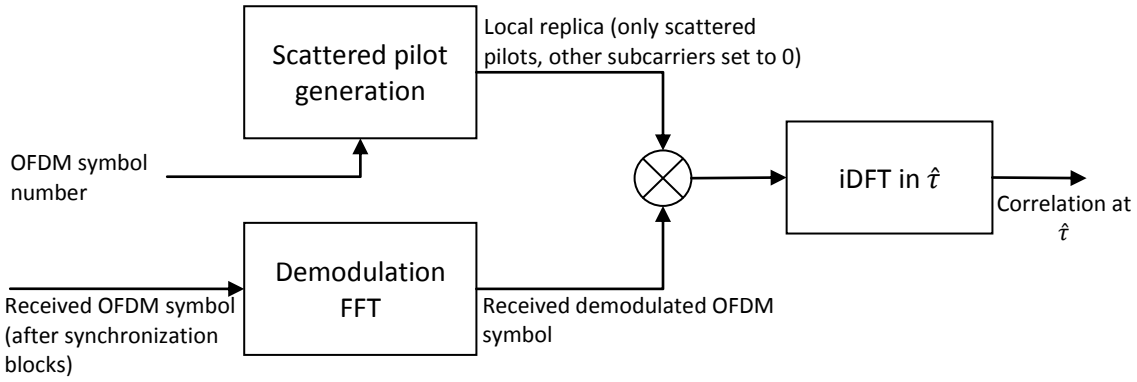

Figure 3.2: Principle of the correlation function computation

According to the diagram of Figure 3.2, the expression of the correlation function of the k-th OFDM symbol is:

$$R^k(\hat{\tau}) = iDFT\left(\left\{\widetilde{d_p^k}P_p^k\right\}_{p\in P_S^k}\right)[\hat{\tau}] = \frac{1}{N_{P_S}}\sum_{p\in P_S^k}\widetilde{d_p^k}P_p^k \exp\left(j2\pi\frac{\hat{\tau}p}{N}\right) \quad (3.2)$$

where:

- $\hat{\tau}$ is the delay, normalized by the sampling period, where the correlation is computed
- $\widetilde{d_p^k}$ is the demodulated symbol over the p-th subcarrier of the k-th OFDM symbol
- P_p^k is the value (-1 or +1) of the pilot over the p-th subcarrier of the k-th OFDM symbol
- $\mathcal{P}_S^k$ is the set of scattered pilot indexes for the k-th OFDM symbol
- $N_{P_S} = \mathrm{card}(\mathcal{P}_S^k)$ is the number of scattered pilot

The correlation function expression is derived supposing that there is no impairment in the transmission, only a timing offset τ in the safe zone (see section 2.1.2.1). Thus, $\widetilde{d_p^k} = d_p^k \exp\left(-j2\pi\frac{\tau p}{N}\right)$ and after some manipulations on Eq. (3.2), it is possible to derive the expression of the correlation function of the k-th OFDM symbol as (see Annex A):

$$R^k(\hat{\tau}) = \frac{1}{N_{P_S}}\frac{4}{3}\exp\left(j2\pi\frac{P_0^k}{N}\,\varepsilon_\tau\right)\exp\left(j\pi\frac{N-12}{N}\varepsilon_\tau\right)\,\frac{\sin\left(\pi\frac{12N_{P_S}}{N}\varepsilon_\tau\right)}{\sin\left(\pi\frac{12}{N}\varepsilon_\tau\right)} \tag{3.3}$$

with:

- $P_0^k = 3\big((k-1)\bmod 4 + 1\big) \in \{12,3,6,9\}$ the index of the first scattered pilot in the k-th OFDM symbol and
- $\varepsilon_\tau = \hat{\tau} - \tau$ the difference between the point where the correlation is computed and the timing offset, also known as the tracking error

It can be seen on Eq. (3.3) that the absolute value of the correlation function is periodic with a period of $\frac{N}{12}$. Indeed:

$$\left|R^k\left(\hat{\tau}+\frac{N}{12}\right)\right| = \frac{1}{N_{P_S}}\frac{4}{3}\left|\frac{\sin\left(\pi\frac{12N_{P_S}}{N}\varepsilon_\tau + 12\pi\right)}{\sin\left(\pi\frac{12}{N}\varepsilon_\tau + \pi\right)}\right| = \frac{1}{N_{P_S}}\frac{4}{3}\left|\frac{\sin\left(\pi\frac{12N_{P_S}}{N}\varepsilon_\tau\right)}{\sin\left(\pi\frac{12}{N}\varepsilon_\tau\right)}\right| = \left|R^k(\hat{\tau})\right| \tag{3.4}$$

This $\frac{N}{12}$ periodicity is a direct consequence of the 12 subcarriers spacing between two successive scattered pilots.

Furthermore, since $N \gg 1$ in the case of DVB-T and for small values of ε_τ, the expression of the correlation function can be simplified and does not depend anymore on the OFDM symbol index k. This simplified expression, denoted $R_U(\hat{\tau})$ and shown on Eq. (3.5), will be used in the following.

$$R_U(\hat{\tau}) = \frac{4}{3}\exp(j\pi\varepsilon_\tau)\,\mathrm{sinc}(\pi\beta\varepsilon_\tau) \tag{3.5}$$

where:

- $\beta = \frac{12N_{P_S}}{N} \approx 0.832$ is a coefficient which represent the width of the sinc function

Figure 3.3 illustrates the periodicity of the absolute value of the correlation function for $N = 2048$ and thus $N_{P_S} = 142$ and a null timing offset. On Figure 3.4 a closer look on the correlation peak show the sinc shape of the correlation function.

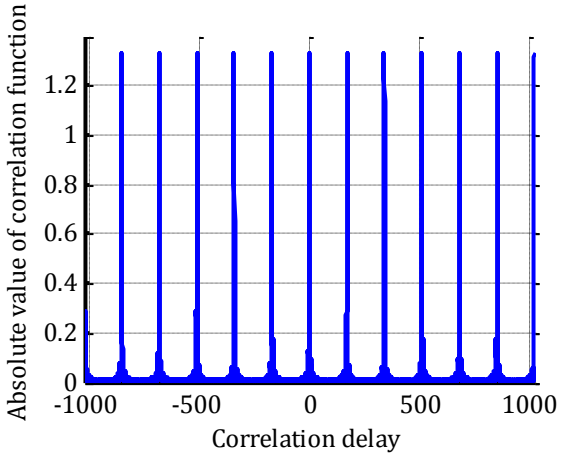

Figure 3.3: Absolute value of the correlation function

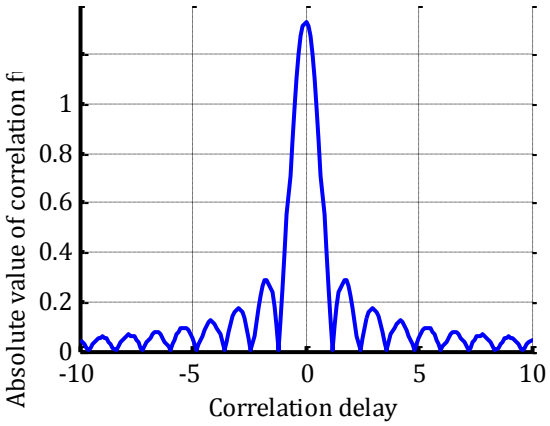

Figure 3.4: Close up on the central peak of the correlation function

3.1.3 Acquisition and tracking processes

Due to the specificities of the terrestrial propagation channel already discussed, the correlation function obtained from real signals will present multiple peaks corresponding to all the replicas of the transmitted signal reaching the receiver. These peaks can evolve very fast (e.g. fading) due to the changing environment in urban conditions. More notably, the peak corresponding to the first received signal (the one of interest for ranging) is not necessarily the most powerful and might not even be present. In order to try to always track the shortest signal (either the direct signal, or by default one of the shortest replicas), the proposed ranging method uses multiple delay lock loops (DLL) in order to constantly track several correlation peaks. This allows relying on the second tracked shortest replica if the first one disappears due to fading or signal blockage. The following method is then used (although slight variations are used depending if the emitters are in SFN or not):

- First, an iterative algorithm, that could be the Matching Pursuit [40], is used to acquire the delays corresponding to the different peaks of the correlation function. In order to make sure that the direct signal or the shortest detectable replica is not missed, this acquisition is run periodically.
- Second, all (or a subset of all) the acquired peaks are tracked independently using several classical DLL using a normalized early-minus-late-power (EMLP) discriminator. The shortest tracked delay is then used to form the pseudorange measurement. Specific detectors are used to minimize the number of replicas tracked.

3.1.3.1 Acquisition of correlation peak delays

Contrary to the GNSS acquisition, it is not necessary to search the correlation peaks over the whole correlation range and for multiple values of the frequency offset (search delay-frequency grid concept). Indeed the timing offset and fractional CFO estimation made by the Van de Beek algorithm, introduced in the section 2.3.1, permit to know precisely the frequency offset and, with a rougher precision (about ±50 samples), the timing offset.

Thus, to find the correlation peaks, the correlation function has to compute just between ±50 samples around the delay estimated by the Van de Beek algorithm. Figure 3.5 shows an example of a correlation function obtained after Van de Beek algorithm, in presence of arbitrary multipathes of delays {0, 4, 12} samples and relative amplitudes {0.5, 1, 0.3}.

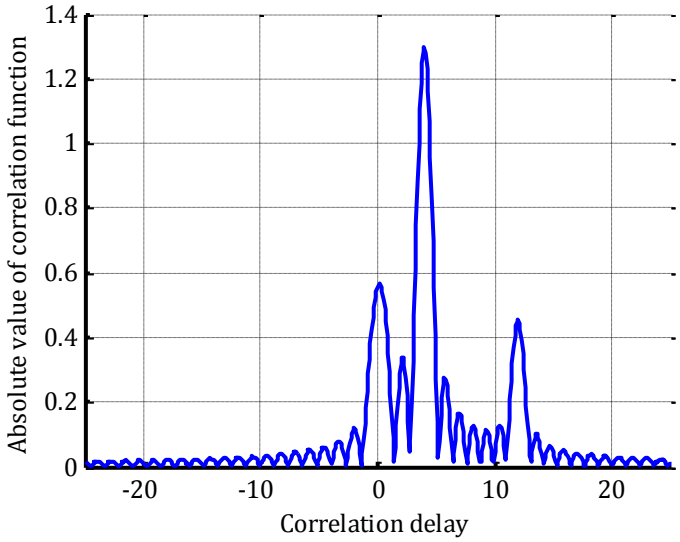

Figure 3.5: Correlation function in presence of multipath

Then the peak delays can be acquired using the matching pursuit algorithm [40] and consist in executing the following actions:

- Find the highest peak in the absolute correlation function, then
- Subtract to the correlation function this estimated peak using the correlation function model $R_U(\tau)$
- Loop the two first steps until no more significant peak has been found until the desired number of peaks has been found

As an illustration, Figure 3.6 shows the result of the MP algorithm applied to the correlation function of Figure 3.5. It can be seen that peak delay estimates are correct but that the amplitude estimates are not so good. Indeed, in the MP algorithm that is implemented here, the absolute value of correlation function is modeled as a sum of absolute sinc functions, whereas in reality it is the absolute value of a sum of sinc functions. This model mismatch creates a slightly erroneous estimation of the peak amplitude but which is not so problematic as long as the peak delays estimation is good.

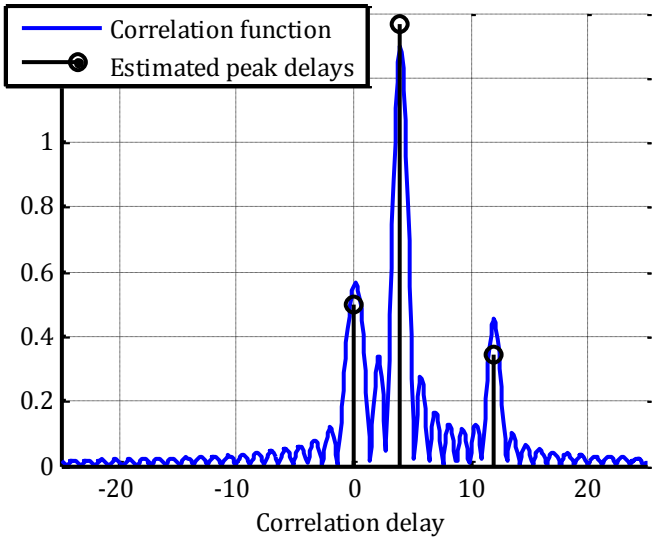

Figure 3.6: Estimated peak delay by MP algorithm

In addition to prevent bad delay acquisitions on the secondary lobes of the sinc function which could appears as peaks for the MP algorithm, it is possible to use windowing techniques in order to reduce the correlation side-lobes, as discussed in section 3.1.5.2.

3.1.3.2 Tracking of correlation peak delays

The tracking of each delay initialized during the acquisition phase is achieved with a classical Delay Lock Loop (DLL) using a normalized Early-Minus-Late-Power (EMLP) discriminator. The block diagram of this DLL is presented on Figure 3.7. There is one DLL running for each delay acquired.

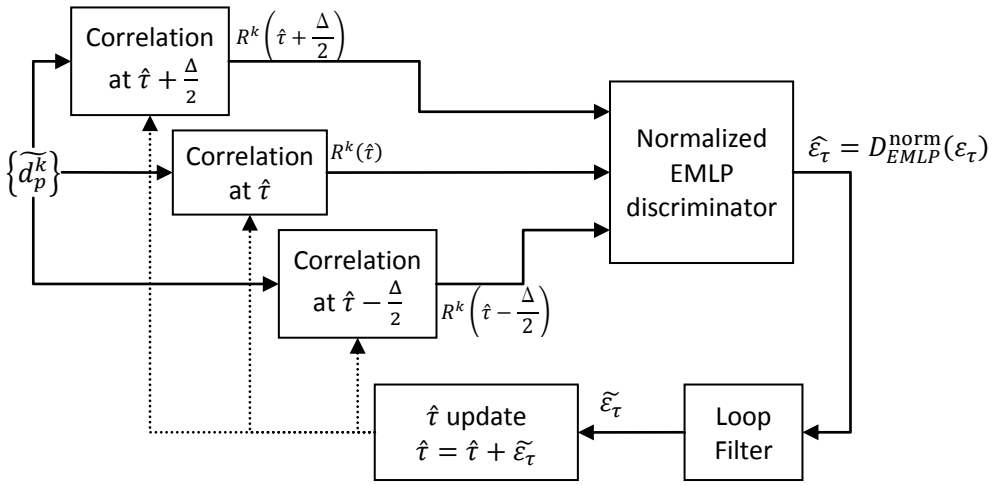

Figure 3.7: DLL block diagram

First, the estimated delay, denoted $\hat{\tau}$, is initialized with the value found in the acquisition phase. The correlation between the k-th demodulated OFDM symbol and the pilot local replica is computed at 3

points: at $\hat{\tau} + \frac{\Delta}{2}$, called the "late" correlation, $\hat{\tau}$, called the "prompt" correlation and $\hat{\tau} - \frac{\Delta}{2}$, called the "early" correlation. The delay between the early and the late correlation points, denoted Δ is called the correlator spacing.

Second, the discriminator is computed, thanks to the values of the early, prompt and late correlations. A first estimate of the tracking error $\varepsilon_\tau = \hat{\tau} - \tau$, defined as the difference between the estimated delay and the true delay, is obtained with the discriminator of the Eq. (3.6).

$$D_{EMLP}^{\text{norm}}(\varepsilon_\tau) = \frac{\left|R\left(\hat{\tau} - \frac{\Delta}{2}\right)\right|^2 - \left|R\left(\hat{\tau} + \frac{\Delta}{2}\right)\right|^2}{K_{norm}|R(\hat{\tau})|^2} \tag{3.6}$$

This discriminator is normalized by a factor denoted K_{norm} such that $D_{EMLP}^{\text{norm}}(\varepsilon_\tau) = \varepsilon_\tau$ for ε_τ close to 0. This normalization factor (calculation in Annex A) is:

$$K_{norm} = \frac{1 - (\Delta/2)\pi\beta.\sin(\pi\beta\Delta) - \cos(\pi\beta\Delta)}{(\pi\beta)^2.\Delta^3/2^4} \tag{3.7}$$

with: $\beta = \frac{12N_{P_S}}{N}$

Figure 3.8 illustrates the discriminator output $D_{EMLP}^{\text{norm}}(\varepsilon_\tau)$ for several values of the correlation spacing Δ.

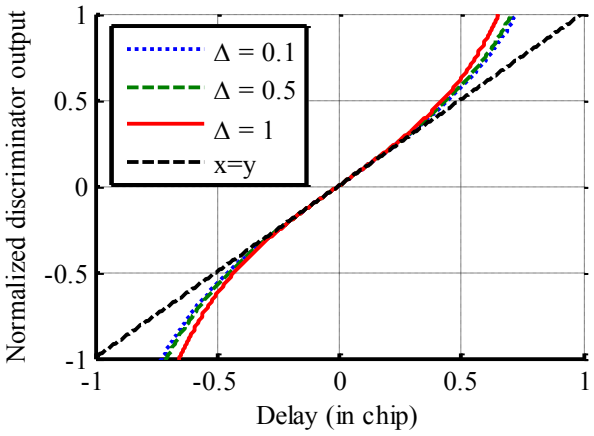

Figure 3.8: Discriminator output

Third, the final estimation of the tracking error is obtained by filtering the discriminator output in order to reduce the estimation noise. The loop filter, inspired from [41], is defined by three parameters: the time between each delay estimate T_l, the loop order and the loop bandwidth B_l. The value of T_l is fixed by the delay between two discriminator output, classically the duration of an OFDM symbol (T_S), the loop order controls the behavior of the loop in dynamic conditions and the loop bandwidth control the sensibility of the loop.

Finally, the new delay estimate at the instant $k+1$, is computed by making the operation of Eq. (3.8). Then new correlations at early, prompt and late points are computed according to this updated delay estimate, leading to a new discriminator output and so on.

$$\hat{\tau}^{k+1} = \hat{\tau}^{k} + \widetilde{\varepsilon_{\tau}} \tag{3.8}$$

3.1.4 DLL exclusions and Re-acquisitions

To fight against the instability of the urban propagation channel that produces on the correlation function quick changes of the peak amplitudes and even sudden disappearance of peaks, two processes are used to manage these issues.

First, the DLL exclusions, which are criteria that stop a DLL if it has diverged or if two (or more) DLLs have converged. The DLL divergence can arise when the tracked peak suddenly disappears (because of signal blockage by a building for example). From this instant the DLL can potentially began to evolve freely in the noise. This divergence can be detected by observing the rate of evolution of the delay. If this rate is too important (compared to expected dynamic of the receiver) the DLL is considered to have diverged. The DLL convergence occurs when two (or more) DLL converges towards the same delay. Then, only one of the converging DLL is kept and the other are stopped. The convergence is detected when the difference between two estimated delays is below a defined threshold (typically one sample).

The second process is the delay re-acquisition. It consists in making periodic delay acquisitions, e.g. every one second, in order to be able to detect and track a newly appeared peak. During re-acquisition only the detected peaks that are not already tracked are kept.

3.1.5 Improvement of correlation operation

In order to improve acquisition and tracking performances, two operations have been introduced in the calculation of the correlation function. There are summations of consecutive correlation functions to reduce noise and windowing techniques to limit the secondary lobes of the correlation function.

3.1.5.1 Use of correlation function summations

There are two types of summations: coherent summations that operate of the complex valued correlation function and the non-coherent summations that operate on the squared absolute value of the correlation function. Mathematically, the expression of the correlation function with N_C coherent summation and N_I non-coherent summations is:

$$R_{N_C,N_I}(\hat{\tau}) = \frac{1}{N_I}\sum_{l=0}^{N_I-1}\left|\frac{1}{N_c}\sum_{k=0}^{N_C-1} R^{k+lN_C}(\hat{\tau})\right|^2 \quad (3.9)$$

where

- $R^k(\hat{\tau})$ si the correlation function computed with the k-th OFDM symbol

It is important to note that, according to Eq. (3.9), $N_C \times N_I$ consecutives symbols are necessary to compute the correlation$R_{N_C,N_I}(\hat{\tau})$, and thus when using summation the loop update time becomes:

$$T_l = T_S N_C N_I \quad (3.10)$$

The interest of the coherent summations compared to the non-coherent summations is a better noise reduction due to the quadratic losses introduced in the non-coherent because of the squared absolute term. This is shown on Figure 3.9, that represents the values of $\sqrt{R_{1,1}(\hat{\tau})}$(in blue), $\sqrt{R_{20,1}(\hat{\tau})}$ (in red) and $\sqrt{R_{1,20}(\hat{\tau})}$ (in green) for N =4096 and supposing a SNR of the received signal of -10 dB.

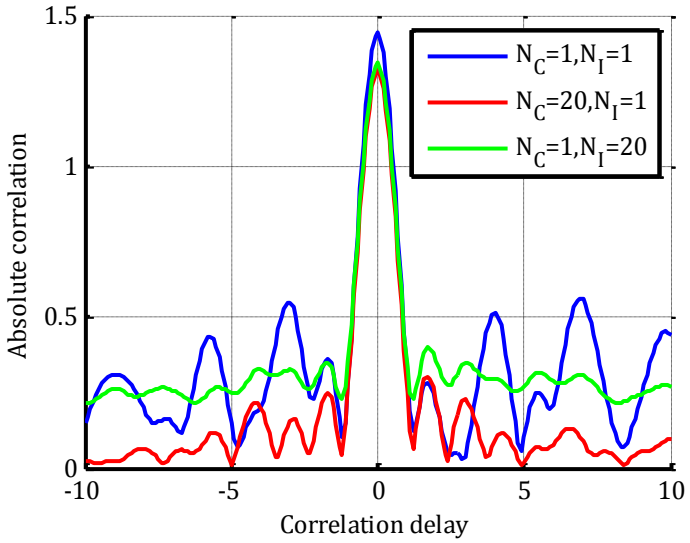

Figure 3.9: Impact of summations on the noise of correlation function

One the other hand, the coherent summations, since they are done on the complex valued correlation, present a problem when the different correlations have not the same phase (for example when a residual CFO is present). The problem does not appear for non-coherent summations since they are done on the squared absolute value of the correlation. This phenomenon is shown on Figure 3.10, where are represented the values of $\sqrt{R_{1,1}(\hat{\tau})}$(in blue), $\sqrt{R_{20,1}(\hat{\tau})}$ (in red) and $\sqrt{R_{1,20}(\hat{\tau})}$ (in green) for N =4096 and supposing a residual CFO of 0.02 (about 100 Hz in this case) and no noise.

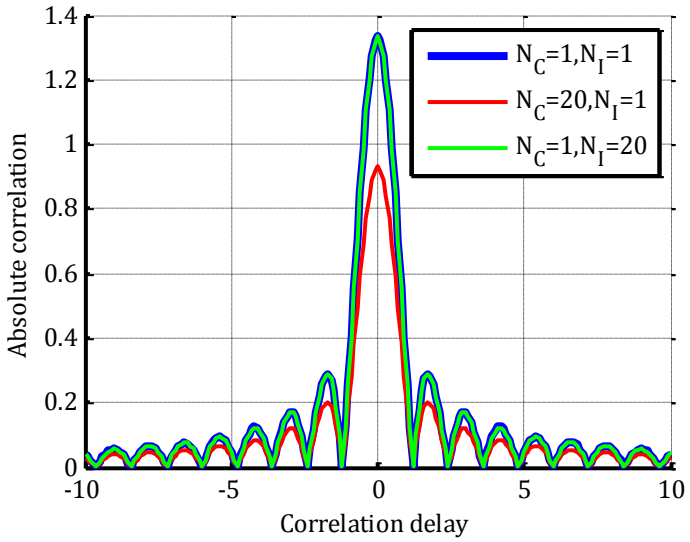

Figure 3.10: Impact of residual CFO in correlation summations

It can be clearly seen that correlation peak amplitude is reduced when used coherent summations. Then even if coherent summations bring an important noise reduction their number has to be limited in order to avoid a significant decrease of the correlation peak amplitude.

Another interesting consequence of coherent summations appears when N_C is a multiple of 4. In this case the $N/12$-periodicity of the absolute correlation function became a $N/3$-periodicity as shown on Figure 3.12. This is due to the fact that 4 consecutive scattered pilot patterns are equivalent to one pattern with pilots spaced by 3 subcarriers, as illustrated on Figure 3.11 from [30]

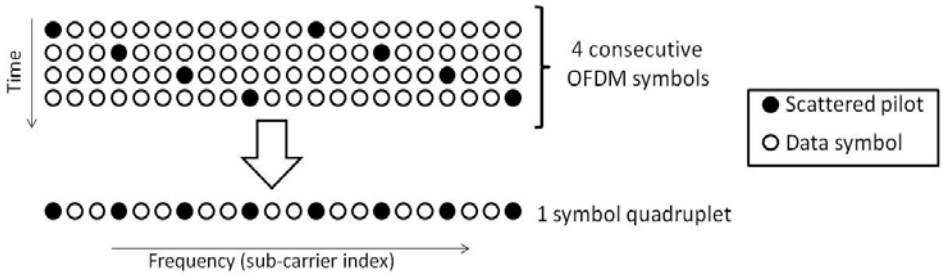

Figure 3.11 Artificial scattered pilot periodicity increase by averaging multiple of 4 consecutive correlation output [30]

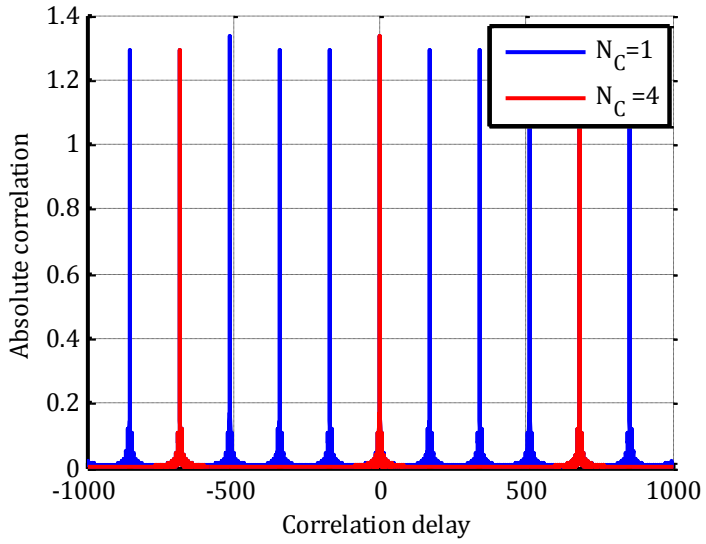

Figure 3.12: Illustration the periodicity reduction of the correlation function for N_C multiple of 4

3.1.5.2 Use of windowing techniques

The goal of windowing techniques is to reduce the secondary lobes that appear on the correlation function, in order to limit the influence of two remote peaks on each other and to avoid false acquisition on secondary lobes. This is achieved by using a window vector, denoted w, in the computation of the correlation:

$$R_w^k(\hat{\tau}) = iDFT\left(\left\{\widetilde{d_p^k} w_p P_p^k\right\}_{p\in P_S^k}\right)[\tau] = \frac{1}{N_{P_S}} \sum_{p\in P_S^k} \widetilde{d_p^k} w_p P_p^{k*} \exp\left(j2\pi \frac{\tau p}{N}\right) \quad (3.11)$$

where:

- $R_w^k(\tau)$ denotes the widowed correlation of the k-th OFDM symbol
- $w_p = 1$ for the rectangular window (i.e. no windowing),
- $w_p = 0.53836 - 0.46164.\cos\left(2\pi \frac{p}{K-1}\right)$ for the hamming window,
- $w_p =$ $0.35875 - 0.48829\cos\left(2\pi \frac{p}{K-1}\right) + 0.14128\cos(4\pi \frac{p}{K-1}) - 0.01168\cos\left(6\pi \frac{p}{K-1}\right)$ for the blackman-harris window

The absolute correlation function is shown on Figure 3.13 for the three selected windows.

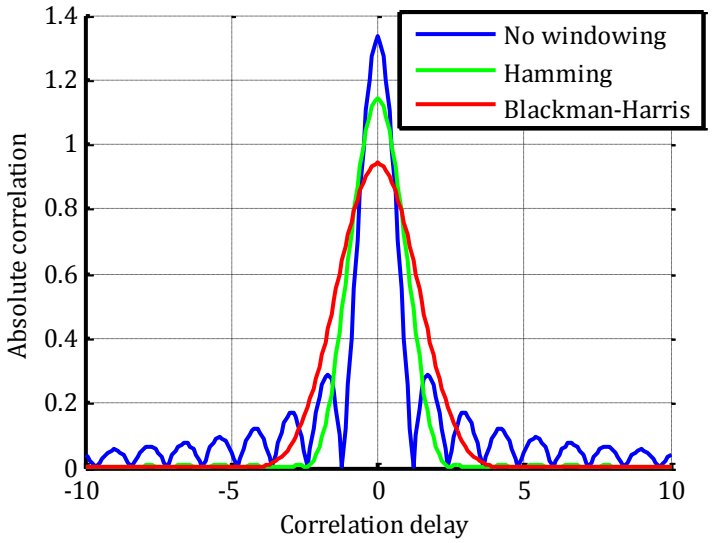

Figure 3.13: Illustration of windowed correlation functions

As it can be seen, the use of windowing impacts three characteristics of the correlation function: amplitude of the main lobe, width of the main lobe and amplitude of sidelobes. Table 3.1 resumes these characteristics through three parameters:

- the sidelobe isolation defined as the difference, in dB, between the correlation peak and the most significant sidelobe amplitudes,
- the peak amplitude and
- the peak width taken at the half maximum amplitude.

Table 3.1: Window characteristics

	Sidelobe isolation (dB)	**Peak amplitude**	**Peak width (in samples)**
Rectangular	13.3	1.33	1.45
Hamming	43	1.14	2.2
Blackman-Harris	93	0.94	3.2

The Blackman-Harris window presents the best sidelobe isolation. The drawbacks are reduced peak amplitude (i.e. reduced noise isolation) and an important increase of the peak width that degrade tracking precision.

The Hamming window presents a good compromise between sidelobe isolation and peak amplitude and width reduction.

3.2 Theoretical Analysis in AWGN

3.2.1 Acquisition performance

As explained earlier the overall acquisition of a correlation peak delay is made in two separate steps:

- The Cyclic Prefix acquisition, based on Van De Beek algorithm, which precisely estimates the fractional CFO and roughly estimates the received signal delay (with a precision of about 100 samples in practice).
- The peak delays acquisition, based on the Matching Pursuit algorithm, which precisely estimates the delay of each peak in the correlation function.

The peak delays acquisition has been extensively studied in [23] and its performance will not be detailed here.

Thus, in this section only the Cyclic Prefix acquisition performance will be studied. Its performance is studied in term of probability of detection to quantify the chances of a successful acquisition for a given SNR of the received signal. As a reminder, the Cyclic prefix acquisition consist is computing a correlation between a window of N_{CP} samples with a window of same size located N samples after. The maximum of the correlation occurs when the 2 windows are respectively located on the Cyclic Prefix and on the end of the OFDM symbol, thus providing a detection of the beginning of the OFDM symbol.

Computing a detection probability is quite challenging because, as the contrary to GNSS acquisition where the received noisy signal is correlated with a clean replica, here a part of the received noisy signal is correlated with another noisy part of itself.

3.2.1.1 Hypothesis test definition

To solve the detection problem, the following hypothesis test is defined:

- H_0: the useful signal is not present → $r_n = n_n$
- H_1: the useful signal is present → $r_n = r_n^u + n_n$

where:

- r_n is the n-th sample of the received signal
- r_n^u is the n-th sample of the received useful signal
- n_n is the n-th sample of the received noise

Let $\sigma_{r^u}^2$ be the power of the useful signal, σ_n^2 the power of noise and $SNR = \frac{\sigma_{r^u}^2}{\sigma_n^2}$ the signal-to-noise of the received signal.

From those two hypotheses, two probabilities can be defined:

- the false alarm probability, denoted p_{fa}, which is the probability to decide H_1 when H_0 is valid or, in other terms, the probability to detect the useful signal when it is not present and

- the detection probability, denoted p_d, which is the probability to decide H_1 when H_1 is valid or, in other terms, the probability to detect the useful signal when it is actually present.

3.2.1.2 Signal detector definition

The signal detection is made by a detector based on the metric of Eq. (2.24) defined in section 2.3.1. This signal detector T is:

$$T = |\Lambda(m)|^2 = \left| \frac{1}{N_{CP}} \sum_{n=m}^{N_{CP}+m-1} r_n r_{n+N}^* \right|^2, m \in [0, N-1] \tag{3.12}$$

To study the false alarm and detection probabilities, the statistical distribution of this detector has to be analyzed under the two hypotheses H_0 and H_1.

Statistical distribution of T under H_0

Under H_0 hypothesis, we have: $r_n = n_n$ Thus, it can be shown (Annex A) that:

$$\frac{2N_{CP}}{\sigma_n^4} T^{H_0} \sim \chi_2^2 \tag{3.13}$$

where:

- $\sigma_n^2 = Var[n_n]$ is the variance of the received noise and
- χ_2^2 denotes the chi-square distribution with 2 degrees of freedom

Then, from this distribution, it is possible to derive, for a given false alarm probability p_{fa}, a threshold T_h such that:

$$p_{fa} = P(T^{H_0} > T_h) \tag{3.14}$$

Statistical distribution of T under H_1

Under H_1 hypothesis, we have: $r_n = r_n^u + n_n$ To compute the statistical distribution in this case we consider the signal detector at the perfect synchronization point. Under this condition, $r_n = r_{n+N_{FFT}}$, for $n \in [m, N_{CP} + m - 1]$ and the value of $|\Lambda(m)|^2$ is maximum. Thus, it can be shown (Annex A) that:

$$\frac{2N_{CP}}{2\sigma_{ru}^2\sigma_n^2 + \sigma_n^4} T^{H_1} \sim \chi_2^2(\lambda) \tag{3.15}$$

where:

- σ_{ru}^2 is the power of the received useful signal
- $\chi_2^2(\lambda)$ denotes the noncentral Chi-square distribution with 2 degrees of freedom
- $\lambda = \frac{2N_{CP}\sigma_{ru}^4}{2\sigma_{ru}^2\sigma_n^2+\sigma_n^4} = \frac{2N_{CP}SNR^2}{2SNR+1}$ is the noncentrality parameter

From this distribution and the previous defined threshold T_h, given a certain signal-to-noise ratio ($SNR = \frac{\sigma_{ru}^2}{\sigma_n^2}$), it is possible to determine the detection probability p_d such that:

$$p_d = P\left(T^{H_1} > \frac{T_h}{1+2SNR}\right) \tag{3.16}$$

3.2.1.3 Use of coherent and non-coherent summations

One way to improve detection performance is to use coherent or non-coherent summations to reduce noise. Supposing N_C coherent summation and N_I non-coherent summations to new detector is:

$$T_{N_C,N_I} = \frac{1}{N_I}\sum_{l=0}^{N_I-1}\left|\frac{1}{N_C}\sum_{k=0}^{N_C-1}\Lambda^{k+lN_I}(m)\right|^2 \tag{3.17}$$

where:

- $\Lambda^k(m) = \sum_{n=m}^{N_{CP}+m-1} r_{n+k.N_t} r^*_{n+k.N_t+N_{FFT}}$ is the CP acquisition metric computed on the k-th N_t-sized block
- $N_t = N + N_{CP}$ is the size of the complete OFDM symbol (i.e. CP included)

Thus the statistical distributions became (Annex A):

$$\frac{2N_{CP}N_CN_I}{\sigma_n^4} T^{H_0}_{N_C,N_I} \sim \chi^2_{2N_I} \tag{3.18}$$

$$\frac{2N_{CP}N_cN_I}{2\sigma_{ru}^2\sigma_n^2+\sigma_n^4} T^{H_1}_{N_C,N_I} \sim \chi^2_{2N_I}(\lambda) \tag{3.19}$$

where:

- $\chi^2_{2N_I}$ denotes the chi-square distribution with $2N_I$ degrees of freedom
- $\chi^2_{2N_I}(\lambda)$ denotes the non-central Chi-square distribution with $2N_I$ degrees of freedom
- $\lambda = \frac{2N_{CP}N_CN_I\sigma_{ru}^4}{2\sigma_n^2\sigma_{ru}^2+\sigma_n^4} = \frac{2N_{CP}N_CN_ISNR^2}{2SNR+1}$ is the non-centrality parameter

3.2.1.4 Illustrations of detection performance

To illustrate the detection performance, Figure 3.14 and Figure 3.15 show the theoretical probability of detection as a function of SNR for different numbers of coherent and non-coherent summations for a false alarm probability of 10^{-3}. The parameters are: $N = 4096$, $CP = 1/8$. On the same figure are cross-plotted the simulated detection probability obtained over 1000 iterations.

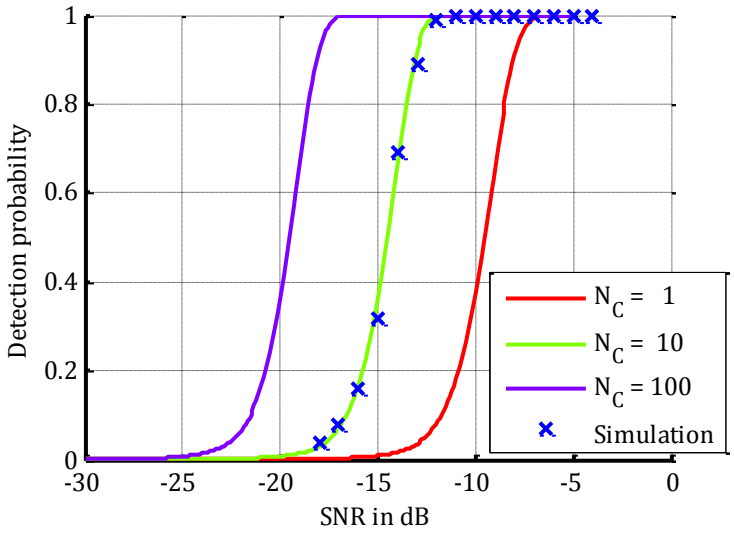

Figure 3.14: Probability detection for different coherent summations ($p_{fa} = 10^{-3}, N_I = 1$)

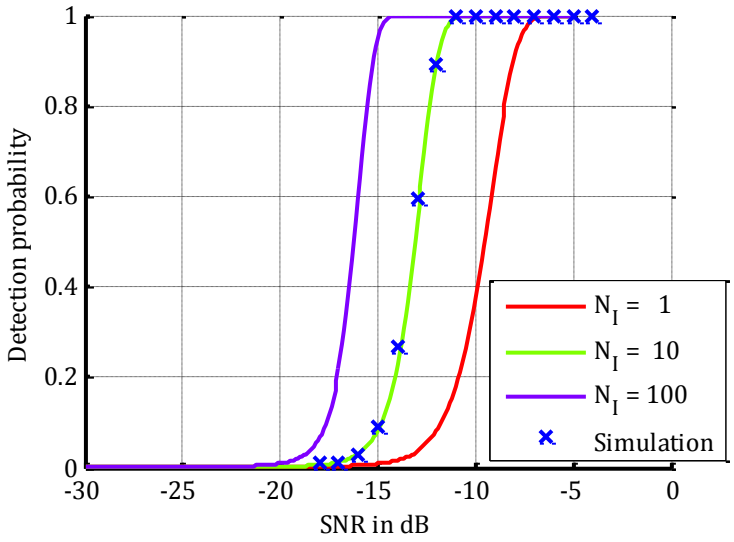

Figure 3.15: Probability detection for different non-coherent summations ($p_{fa} = 10^{-3}$, $N_C = 1$)

It can be seen simulated results match perfectly the theoretical ones. Then, it is clear that coherent summations present a better noise reduction that non-coherent summation. It is a classical result due to squaring losses. However, it is important to note that, coherent summations are sensitive to phase variations induced by, for example, CFO and propagation channel variations.

Another interesting figure of merit to analyze is the number of coherent or non-coherent summation that is necessary to reach a certain detection probability for a SNR and a false alarm probability fixed. For example, Figure 3.16 gives these numbers as a function of SNR for $p_{fa} = 10^{-3}$ and $p_d = 0.99$. We have also $N = 4096$ and $CP = 1/4$.

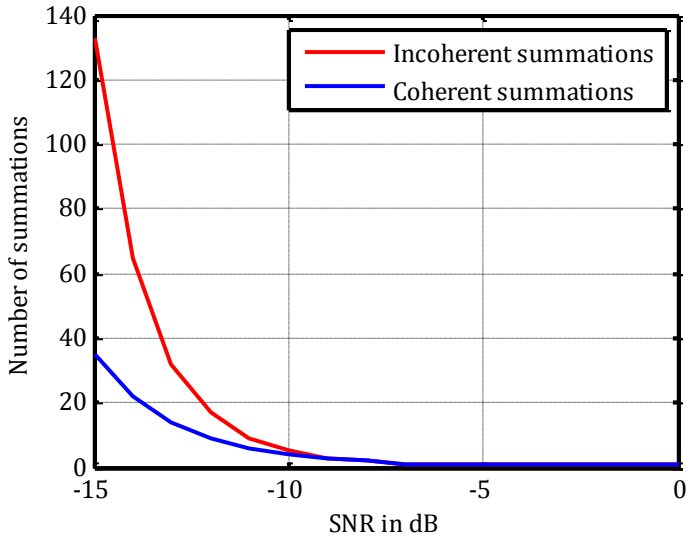

Figure 3.16: Number of summations needed as a function of SNR ($p_{fa} = 10^{-3}, p_d = 0.99$)

Thus, even at a very low SNR (the operational SNR for demodulate TV data is around 10-20 dB) it is possible to satisfy restrictive false alarm and detection probabilities with a limited number of summations.

3.2.2 Tracking performance

Of course, the tracking performance in an AWGN channel is very different from the performance in urban propagation channel that present numerous and powerful multipathes. However, it is still important to perform this study in an ideal propagation channel to give an idea of the maximum reachable performance to point out the potential of the PR estimation method.

The tracking performance is analyzed by calculating the variance of the estimated delay. For this purpose, a model of the noisy correlation function is derived. The next step is to compute the variance of the normalized EMLP discriminator output (see section 3.1.3.2). Then the variance of the estimated delay, which is the discriminator output filtered by the loop filter can be computed. Finally a tracking threshold is computed, defined as a limit SNR from which the tracking is decided impossible.

3.2.2.1 Model of the correlation output in presence of noise

The correlation output model is given for the following hypothesis:

- The receiver is perfectly frequency synchronized: no CFO, no SCO.
- The propagation channel is an AWGN (no multipath, only an additive Gaussian noise).
- An attenuation coefficient α due to propagation is applied on the received signal.
- A timing offset τ in the “safe zone”.

In these conditions and according to section 2.1.2 the expression of the demodulated symbols is :

$$\widetilde{d_p^k} = \alpha d_p^k P_p^k \exp\left(-j2\pi \frac{\tau p}{N}\right) + n_p^k \tag{3.20}$$

In addition the SNR is defined as the ratio between the power of data subcarriers and the power of the noise on those subcarriers, as expressed on Eq. (3.21).

$$SNR = \frac{\alpha^2 \sigma_{d,\text{data}}^2}{\sigma_n^2} = \frac{\alpha^2}{\sigma_n^2} \tag{3.21}$$

where:

- $\sigma_{d,\text{data}}^2$ is the variance of the data symbols, equals to 1 with our signal definition (see section 2.2.2).

According to Eq. (3.5) defined in section 3.1.2, the correlation of the two terms of the demodulated symbols of Eq. (3.20) leads to the following noisy correlation function model:

$$R(\hat{\tau}) = \alpha R_U(\hat{\tau}) + R_N(\hat{\tau}) \tag{3.22}$$

where:

- $R_U(\hat{\tau}) = \frac{4}{3}\exp(j\pi\varepsilon_\tau)\,\text{sinc}\left(\pi \frac{12N_{P_S}}{N}\varepsilon_\tau\right)$ is the useful correlation (i.e. without noise) as calculated in section 3.1.2 and
- $R_N(\hat{\tau}) = \frac{1}{N_{P_S}} \sum_{p \in P_S^k} n_p^k P_p^{k^*} \exp\left(j2\pi \frac{\hat{\tau} p}{N}\right)$ is the noise term of the correlation.

3.2.2.2 Variance of discriminator output

The expression of the discriminator is (see section 3.1.3.2):

$$D_{EMLP}^{\text{norm}}(\varepsilon_\tau) = \frac{\left|R\left(\hat{\tau} - \frac{\Delta}{2}\right)\right|^2 - \left|R\left(\hat{\tau} + \frac{\Delta}{2}\right)\right|^2}{K_{norm}|R(\hat{\tau})|^2} \tag{3.23}$$

To make this calculation several hypothesis are made:

- The discriminator normalization by the prompt correlator is supposed perfect, i.e. it is assumed that there is no noise component on the value of $R(\hat{\tau})$. In practice to achieve that noisy conditions, one can obtain an almost noiseless value of $R(\hat{\tau})$ by averaging it on several consecutive OFDM symbols.
- The tracking error is supposed close to zero ($\varepsilon_\tau \simeq 0$)

It can be demonstrated that the variance of the normalized discriminator output is (Annex A):

$$Var(D_{EMLP}^{\text{norm}}) = \frac{K_1}{N_C N_I N_{P_S} SNR}\left[1 + \frac{K_2}{N_C N_{P_S} SNR}\right] \tag{3.24}$$

where:

- $K_1 = \frac{9\left(1-\text{sinc}(\pi\beta\Delta)\right)\text{sinc}\left(\pi\beta\frac{\Delta}{2}\right)^2}{4{K_{norm}}^2}$, $K_2 = \frac{9\left(1+\text{sinc}(\pi\beta\Delta)\right)}{32\text{sinc}\left(\pi\beta\frac{\Delta}{2}\right)^2}$, $K_{norm} = \frac{1-(\Delta/2)\pi\beta.\sin(\pi\beta\Delta)-\cos(\pi\beta\Delta)}{(\pi\beta)^2.\Delta^3/2^4}$.
- $\beta = \frac{12N_{P_S}}{N}$.
- Δ is the correlator spacing.
- N_{P_S} is the number of scattered pilot.

- N_C and N_I are respectively the numbers of coherent and non-coherent summations of the correlation points used in input of the discriminator.
- SNR is the ratio between the power of data subcarriers and the power of the noise on the subcarriers as defined in Eq. (3.21).

According to Eq. (3.24), some observations can be done about the variance of the normalized ELMP discriminator output:

- The higher the SNR is, the smaller the discriminator output variance.
- The higher the total number of subcarriers N is, the smaller the discriminator output variance, as the number of scattered pilot N_{P_S} is proportional to the total number of subcarriers N (see Table 2.6).
- The higher the numbers of coherent and non-coherent summation are, the smaller the discriminator output variance is. In addition, coherent summations permit a better variance diminution than non-coherent summations by reducing the quadratic losses (the second term in the brackets of Eq. (3.24)).

3.2.2.3 Variance of the tracking error estimate

To compute the variance of the tracking error estimate it is supposed that the loop has converged. The loop filter is defined by three parameters (see section 3.1.3.2 for details) including the loop bandwidth B_l and the loop update time $T_l = N_C N_I T_S$. According to [18] if the discriminator output is known, the variance of the tracking error estimate $\widetilde{\varepsilon_\tau}$ can be easily found and is:

$$Var[\widetilde{\varepsilon_\tau}] = 2B_l T_l Var(D_{EMLP}^{\text{norm}}) = \frac{2B_l T_S K_1}{N_{P_S} SNR}\left[1 + \frac{K_2}{N_C N_{P_S} SNR}\right] \tag{3.25}$$

According to Eq. (3.25), some observations can be done:

- Most of the time $B_l T_l \ll 1$, thus the introduction of the loop filter permits to significantly reduce the variance of the estimated tracking error
- The greater the loop update time is, the higher the variance of the tracking error estimate is. Indeed, if the loop update-time increases while the loop bandwidth remains constant, the loop is necessarily more reactive and thus, the variance of the estimated tracking error estimate augments.
- When the number of scattered pilot N_{P_S} augments (i.e when N augments), the OFDM symbols duration T_S and thus the loop update time T_l augments in the same proportion. Thus, the principal coefficient $\frac{2B_l T_S K_1}{N_{P_S} SNR}$ is constant and only the quadratic losses ($\frac{K_2}{N_C N_{P_S} SNR}$) are reduced. This analysis is only true for DVB-T signals if which the ratio between the FFT size and the number of scattered subcarrier is fix (and equal to $1024/71$). More generally, if the number of pilot augment (the FFT size being constant) the variance of the tracking error decreases.
- The higher the CP ratio is, the longer the OFDM symbol duration T_S and the loop update time is, and thus the higher the variance of the tracking error estimate is.
- When the number of coherent summations augments, the quadratic losses are reduced.
- The number of non-coherent summations has no influence on the tracking error variance.

3.2.2.4 Validation of theoretical variance formulas

The two theoretical formulas of Eq. (3.24) and Eq. (3.25) have been validated by simulations. Validation results for each formula are in the 2 following subparts. To validate this formula a synthetic DVB-T signal has been generated with the following parameters:

- $N = 4096$
- $CP = 1/8$
- Null propagation delay ($\tau = 0$)
- Adjustable SNR

Validation of discriminator variance output

The normalized EMLP discriminator has been computed for each generated OFDM symbols at a null delay (to ensure that $\varepsilon_\tau \simeq 0$, has supposed in the theoretical calculation) and finally, its variance has been computed and compared to the theoretical one. The assumption of a perfect normalization of the discriminator made for the calculation of the theoretical expression has not been made in the simulation. Thus, the EMLP discriminator is normalized by the noisy prompt correlation. Figure 3.17 shows the simulated standard deviation as a function of SNR and its comparison with the theory. The parameters of the discriminator are: $\Delta = 1$, $N_C = 1$ and $N_I = 1$. The unit is converted in meter according to the following formula:

$$\text{stdev}(D_{EMLP}^{\text{norm}})_{\text{meter}} = \sqrt{Var[D_{EMLP}^{\text{norm}}]}.T_{samp}.c_{light} \tag{3.26}$$

where:

- T_{samp} is the sampling period (see Table 2.1)
- c_{light} is the speed of light

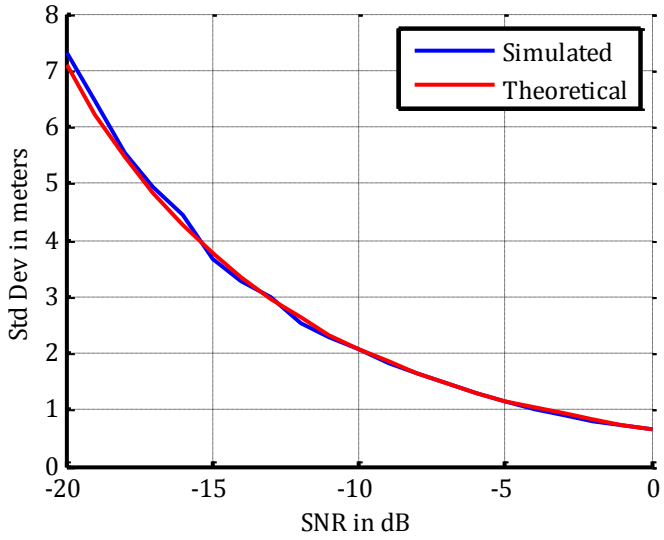

Figure 3.17: Simulated and theoretical standard deviations of the discriminator output

Simulated and theoretical results match perfectly, despite the non-perfect normalization of the EMLP discriminator in the simulation, proving that the simplification made on the theoretical calculation is not harmful.

Validation of estimated tracking error variance

The same simulation has been made with the integration of the loop filter. Thus, in this case, the delays of the early, prompt and late correlations are totally controlled by the loop and not fixed as is the previous simulation (closed-loop). Figure 3.18 shows the simulated tracking error estimate standard deviation as a function of SNR, and its comparison to the theoretical value. The parameters of the discriminator are: $\Delta = 1$, $N_C = 1$. The parameters of the loop are: $B_l = 10\ Hz$ and $T_l = T_S$ (T_S is the duration of one OFDM symbol). As in the previous simulation the unit is converted into meter.

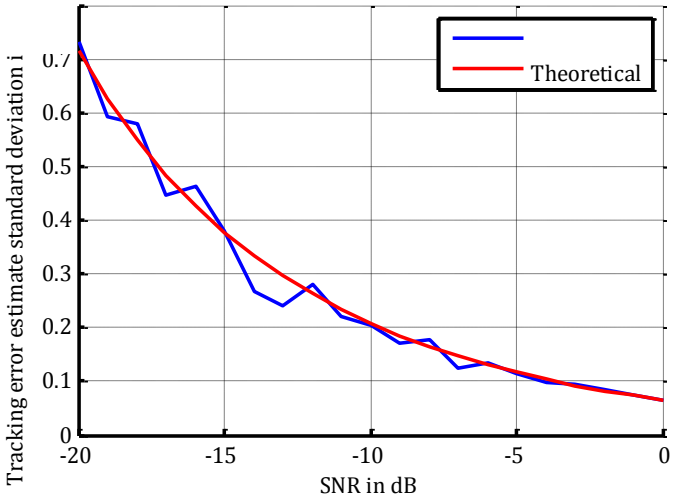

Figure 3.18: Simulated and theoretical standard deviation of the tracking error estimate

Here again, the simulated results match perfectly the theoretical ones. The tracking error variance is very small (below one meter) even for SNR very low. Since operational SNR to demodulate TV data are around 15 dB, a large SNR margin is available, authorizing good tracking performances even out of the coverage of the TV emitter (indoor or far from the emitter).

3.2.2.5 Impact of signal, discriminator and loop parameters on tracking error estimate variance

In this section, the impact of signal, discriminator and loop parameters on the tracking error estimate variance are analyzed using the theoretical formula. Table 3.2 shows the simulation parameters and their default values. The parameters having their impact studied are in red. Since, according to Eq. (3.25), the impact of non-coherent summation is null, its impact is not studied here.

Table 3.2: Simulation parameters default values

Category	Parameters	Default value
DVB-T Signal parameter	FFT size N - Mode	4096 – 4K
	CP ratio	1/8
	Approximate Bandwidth – T_{samp}	8 MHz – 7/64 µs
Discriminator parameters	Number of coherent summations N_c	1
	Correlator Spacing Δ	1 sample
Loop parameters	Loop bandwidth B_l	10 Hz
	Loop update time T_l	$T_S.N_c$

Impact of FFT size

Figure 3.19 shows the theoretical standard deviation of the tracking error estimate as a function of SNR for the 3 possible values of the FFT size (2048, 4096, and 8192) in a DVB-T signal. It is important to note that augmenting the FFT size increases the number of scattered pilot subcarriers N_{P_S}(see Table 2.6) but it also increases the OFDM symbol duration T_S (indeed $T_S = N(1 + CP)T_{samp}$) and thus the loop update time T_l.

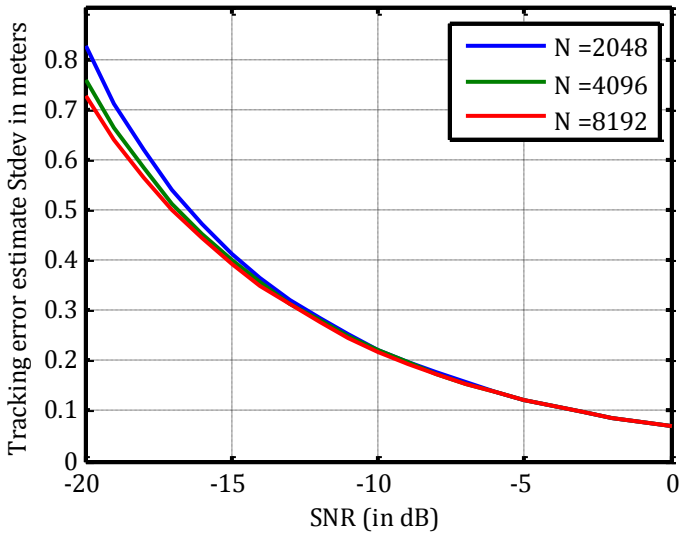

Figure 3.19: Impact of the FFT size on the tracking error estimate standard deviation

The impact of the FFT size on the tracking error is almost null, except for low SNR. Indeed, according to Eq. (3.25), the gain on the discriminator output variance due to an increase of the number of scattered pilot is almost entirely compensated by the increase of the loop update time that forces the loop the be more reactive and more permissive regarding the noise. The small gain impacts the quadratic losses and so appears only at low SNR. However at -20 dB, the quadratic losses are still weak and the impact FFT size is thus limited.

Impact of coherent summations

Figure 3.20 shows the theoretical standard deviation of the tracking error estimate as a function of SNR for 3 values of the coherent summation number (1, 10, and 100).

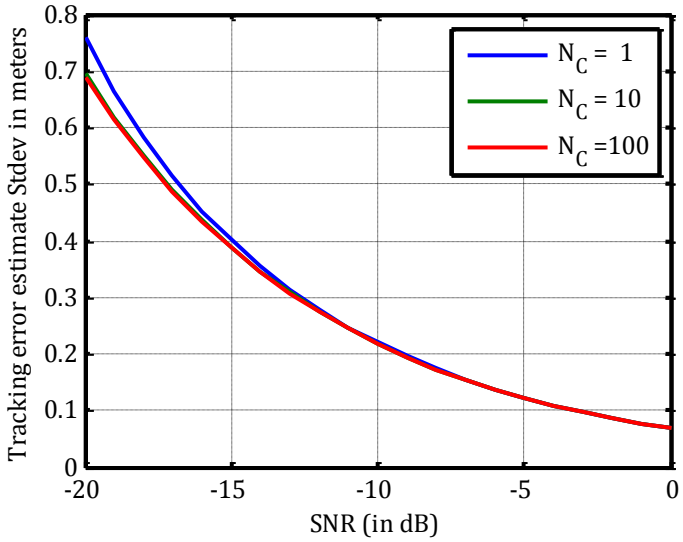

Figure 3.20: Impact of the coherent summation number on the tracking error estimate standard deviation

The impact of coherent summations on is almost null, except for low SNR. Indeed, according to Eq. (3.25), the coherent summations reduce only the quadratic losses, which are significant at low SNR. However at -20 dB, the quadratic losses are still weak and the impact of coherent summation is thus limited.

Impact of correlator spacing

Figure 3.21 shows the theoretical standard deviation of the tracking error estimate as a function of SNR for 3 values of the correlator spacing (0.1, 0.5, and 1).

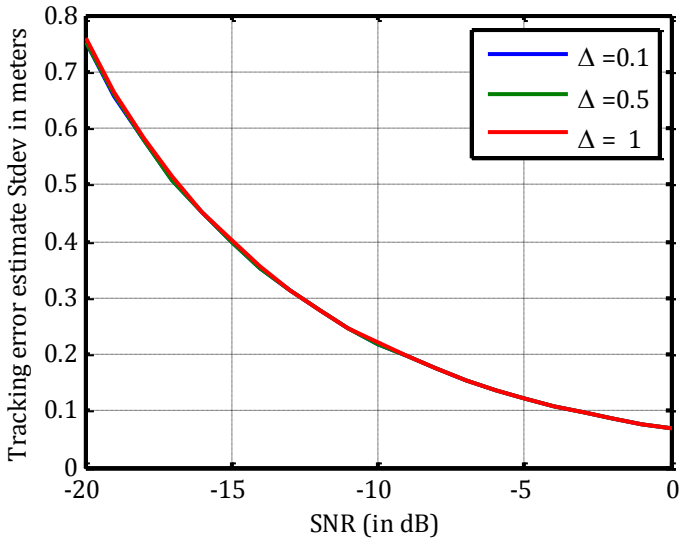

Figure 3.21: Impact of the correlator spacing on the tracking error estimate standard deviation

The 3 curves are superimposed. So, the correlator spacing has no influence on the tracking error estimate variance. This result could be quite surprising in view of the strong dependence on Δ of the factors K_1 and K_2 in the theoretical formula of the tracking error estimate variance of Eq. (3.25).

Impact of loop bandwidth

Figure 3.22 shows the theoretical standard deviation of the tracking error estimate as a function of SNR for 3 values of the loop bandwidth (1 Hz, 5 Hz, and 10 Hz).

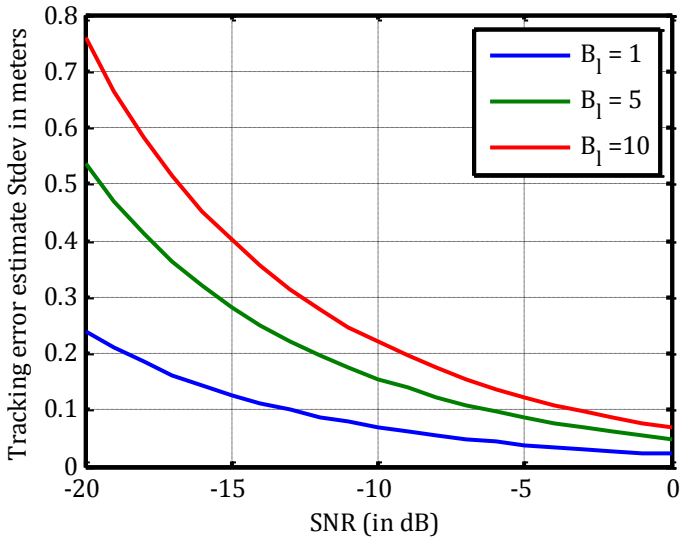

Figure 3.22: Impact of the loop bandwidth on the tracking error estimate standard deviation

As expected the tracking error estimate variance is decreasing when the loop bandwidth is reduced. However reducing the loop bandwidth decreases the reactivity of the loop. Thus, there is a compromise to found to have the smallest loop bandwidth possible while keeping a good reactivity of the loop. This reactivity, not so important in the considered AWGN propagation channel where the

dynamic is only due to receiver moves, become necessary in the urban propagation channel which is very unstable.

3.2.2.6 Tracking threshold

The tracking threshold is a SNR value, denoted SNR_{th}, below which the loop can be considered to have lost tracking. According to [18], a criterion to decide that the tracking is lost, is when the 3-sigma value of the tracking error becomes greater than the linearity zone of the discriminator. Indeed, in that case, a non negligible amount of the discriminator outputs are out of the linearity zone and a divergence of the loop may occur. According to Figure 3.8 the linearity zone of the studied discriminator spans about 0.5 delay unit. Thus, mathematically, the tracking loss criterion is:

$$3\sqrt{Var[D_{EMLP}^{\text{norm}}]} > \frac{1}{2} \tag{3.27}$$

Thus, when the inequality of Eq. (3.27) is true the tracking is considered loss.

According to the theoretical expression of $Var[D_{EMLP}^{\text{norm}}]$ presented on Eq. (3.25), it is easy to find the expression of SNR_{th} such as the inequality of Eq. (3.27) is true. After a resolution of a quadratic equality (see Annex A) it comes:

$$SNR_{th} = \frac{36B_l T_S K_1}{N_{P_S}}\left[1 + \sqrt{1 + \frac{K_2}{18B_l T_S N_C K_1}}\right] \tag{3.28}$$

where:

- $K_1 = \frac{9\left(1-\text{sinc}(\pi\beta\Delta)\right)\text{sinc}\left(\pi\beta\frac{\Delta}{2}\right)^2}{4K_{norm}{}^2}$
- $K_2 = \frac{9\left(1+\text{sinc}(\pi\beta\Delta)\right)}{32\text{sinc}\left(\pi\beta\frac{\Delta}{2}\right)^2}$

Figure 3.23, Figure 3.24, Figure 3.25 and Figure 3.26 show the value of the tracking threshold as a function of FFT size, coherent summation number, correlator spacing and loop bandwidth. The default simulation parameters are the same than in Table 3.2.

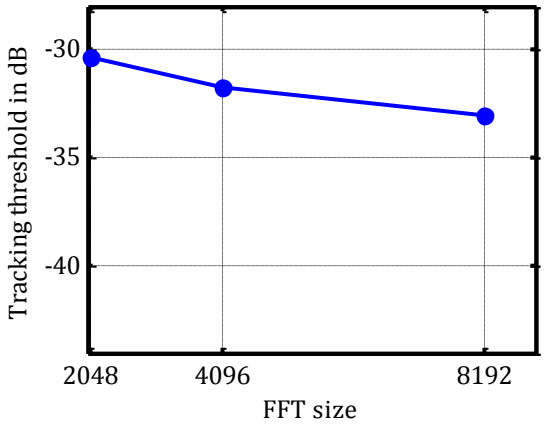

Figure 3.23: Impact of the FFT size on tracking

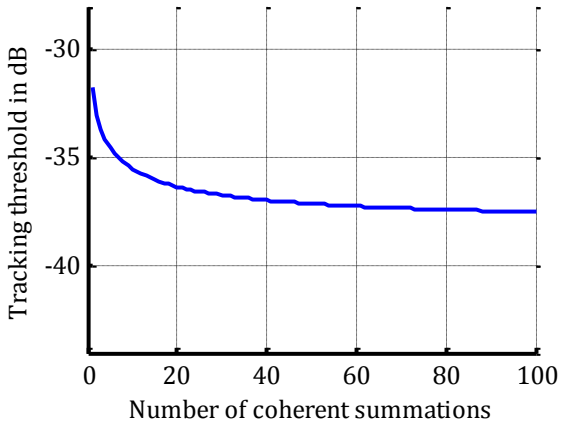

Figure 3.24: Impact of the number of summations

threshold *on tracking threshold*

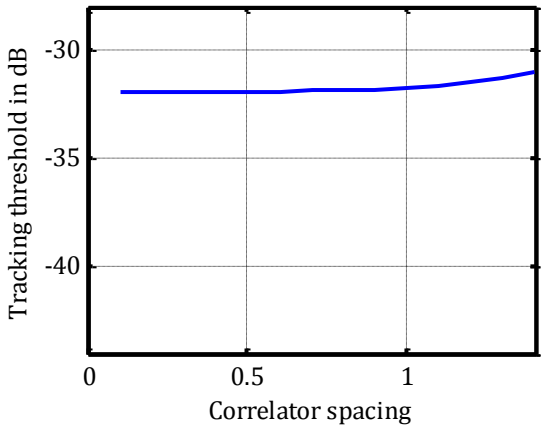

Figure 3.25: Impact of the correlation spacing on tracking threshold

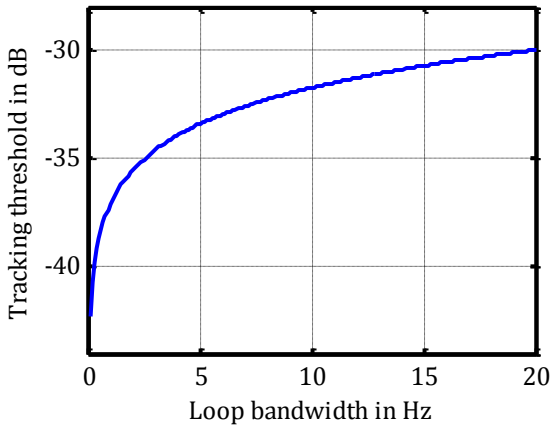

Figure 3.26: Impact of the loop bandwidth on tracking threshold

The tracking threshold for the default parameters is about -32 dB. The correlator spacing has no impact on the value of tracking threshold and FFT size has a limited impact (the tracking threshold is a little bit reduced when the FFT augments).

Coherent summations permits a reduction of the tracking threshold until $N_c = 20$, from which the tracking threshold is comprised between -36 and -38 dB.

Finally the smallest loop bandwidth presents the lowest tracking threshold. However, if the loop bandwidth is too small, the loop is not reactive enough to follow the receiver dynamic and the propagation channel variations.

3.2.2.7 Extension to the case of windowed correlation

The theoretical formulas have been developed in the case of the rectangular window where the correlation is sinc shaped. To extend the formulas to the other windows, one can, instead of consider the exact expression of the windowed correlation function, find the sinc function that best approximates the main lobe of the considered widowed correlation function. This approximation is valid because during the peak tracking, the correlation is always computed on the main lobe of the sinc function. For each possible window, the value of the coefficients β_w (that controls the wideness of the main lobe of the approximating sinc function) and K_w (that controls the amplitude of the main lobe of the approximating sinc function) are such that:

$$|R_w(\hat{\tau})| = \frac{4}{3} K_w |\mathrm{sinc}(\pi \beta_w \varepsilon_\tau)| \tag{3.29}$$

Table 3.3 gives the values, determined empirically, of those coefficients for the 3 possible windows:

Table 3.3: Sinc function parameters

Window technique	**Main lobe widening factor β_w**	**Main lobe amplitude factor K_w**

Rectangular	$\beta = \frac{12N_{P_S}}{N} \approx 0.832$	1
Hamming	$\frac{\beta}{1.5}$	0.9374
Blackman-Harris	$\frac{\beta}{2.1}$	0.7744

Thus the expressions of the tracking error estimate variance and tracking threshold became:

$$Var[\tilde{\varepsilon_\tau}] = 2B_l T_l Var(D_{EMLP}^{\text{norm}}) = \frac{2B_l T_S K_1}{N_{P_S} K_w^2 SNR}\left[1 + \frac{K_2}{N_C N_{P_S} K_w^2 SNR}\right] \quad (3.30)$$

$$SNR_{th} = \frac{36B_l T_S K_1}{N_{P_S} K_w^2}\left[1 + \sqrt{1 + \frac{K_2}{18B_l T_S N_C K_1}}\right] \quad (3.31)$$

where:

- $K_1 = \frac{9\left(1-\text{sinc}(\pi\beta_w\Delta)\right)\text{sinc}\left(\pi\beta_w\frac{\Delta}{2}\right)^2}{4{K_{norm}}^2}$, $K_2 = \frac{9\left(1+\text{sinc}(\pi\beta_w\Delta)\right)}{32\text{sinc}\left(\pi\beta_w\frac{\Delta}{2}\right)^2}$,

  $K_{norm} = \frac{1-(\Delta/2)\pi\beta_w.\sin(\pi\beta_w\Delta)-\cos(\pi\beta_w\Delta)}{(\pi\beta_w)^2.\Delta^3/2^4}$

Figure 3.27 and Table 3.4 show the theoretical tracking error estimate standard deviation and the tracking threshold for each possible window and for the default parameters of Table 3.2.

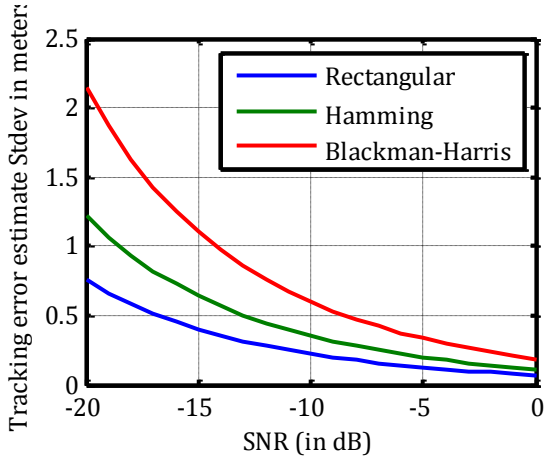

Figure 3.27: Tracking error estimate standard deviation for different correlation window

Table 3.4: Tracking threshold for different correlation window

Windows	**Tracking threshold**
Rectangular	-32 dB
Hamming	-29 dB
Blackman-Harris	-26 dB

The rectangular window presents the best results, then the Hamming window and finally the Blackman-Harris window. However, it is important to note that Hamming and Blackman-Harris windows permit an important attenuation of the secondary lobes that permit to reduce influence between two remote correlation peaks. Thus, even if in the case of AWGN channel, where only one peak is present in the correlation function, the rectangular window will be always preferred, in the

case of urban propagation channel, where multiple peaks are present in the correlation function, the Hamming and Rectangular windows present an important interest.

3.2.3 Conclusions

This theoretical analysis shows very promising results for the use of DVB-T, and more generally of OFDM modulation, as signal-of-opportunity for positioning. Indeed the time and frequency acquisition is possible at very low SNR (relatively to the typical SNR observed for this kind of signal) and very easily. The theoretical tracking performance is also very good at low SNR.

However, this theoretical study is valid for AWGN propagation channels which are never encountered in real world, especially when terrestrial networks and urban/indoor environments are envisaged. Whatever, this theoretical study is a good starting point to validate the feasibility and allow advanced tests on realistic signals.

4 Development and Validation of a DVB-T Ranging Test Bench

As explained in section 3.1.1, no urban propagation channel models adapted to positioning were found in literature. In addition [28], has shown very promising results on semi-simulated DVB-SH signal based on a field channel sounding but with a part of simulated data. Thus, to go a step further and to be able to quantify the PR estimation performance in a realistic channel, tests on real signal were considered as necessary.

Section 4.1 describes the developed test bench, composed of a hardware part, used to record a TV signal with a GPS time reference, and of a software part, consisting in a signal recording software and in a signal processing software. Section 4.2 presents the validation of the software part of the test bench. Section 4.3 describes the validation process of the hardware part and more particularly the synchronization of the hardware clock on an external reference.

4.1 Description of the Test Bench

The test bench is composed of a hardware part and of two pieces of software.

The hardware part allows receiving and digitizing TV signals from two independent TV antennas. Additionally a GPS receiver provides time references (10 MHz and 1PPS signals) for the rest of the hardware and permit to have a reference position. This test bench has been designed to be very flexible and the two reception chains allow the following test configurations:

- Two mobile TV antennas receiving the same signal to exploit antenna diversity and improve measurement quality.
- Two mobile TV antennas receiving two signals at different frequencies from the same emitter to exploit frequency diversity.
- Two mobile TV antennas receiving two signals at different frequencies from two emitters to have two PR measurements.
- One fixed antenna and one mobile to perform differential measurements.

The signal recording software is used to configure and control the hardware and to collect and save the digitized TV signal on the computer hard drive.

The signal processing software implements the PR estimation method to process the recorded signal.

4.1.1 Description of the hardware part

Figure 4.1 shows the block diagram of the hardware part of the test bench. It can be split in 3 groups:

- the 3 antennas (2 TV antennas, 1 optional, and 1 GPS antenna) to receive TV and GPS signals,
- the 2 USPR2/WBX devices (1 optional) to digitize and record TV signals from the 2 TV antennas and

- the GPS receiver to provide a GPS time reference and a position reference.

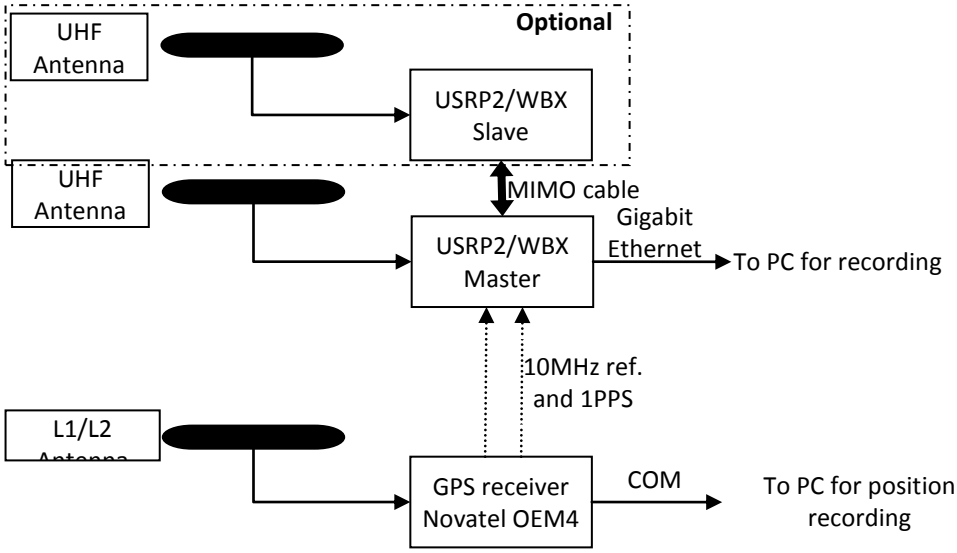

Figure 4.1: Block diagram of the test bench hardware

Antennas:

Three antennas are used:

- Mass-market amplified mobile omnidirectional UHF antenna ELAP 240011 – 40 dB gain, 1.1 dB noise factor (vendor information) (see Figure 4.2)
- Mass-market amplified indoor omnidirectional UHF antenna Meliconi Ad-elegance – 20 dB gain, 3.5 dB noise factor (vendor information) (see Figure 4.3)
- GPS L1/L2 GPS antenna Novatel ANT-534-C – 40 dB gain, 1.9 dB noise factor. (see Figure 4.4)

Figure 4.2: ELAP UHF antenna

Figure 4.3: Meliconi UHF antenna

Figure 4.4: Novatel GPS L1/L2 antenna

USRP2/WBX devices

The USRP2 (see picture on Figure 4.5), built by Ettus Research LLC [42] is a low-cost, flexible and open-source radio device, controlled by PC, that permits to receive and transmit simultaneously on two antennas a limitless variety of signal.

The USPR2 includes two analog-to-digital converters (ADC), (I-Q pair) with a sampling rate of 100 MS/s and a resolution of 14 bits, for the reception chain and two digital-to-analog converters (DAC), (1 I-Q pair) with a sampling rate of 100 MS/s and a resolution of 16 bits, for the transmission chain.

A FPGA (Xilinx Spartan 3-2000) allows performing high sample rate operations, like digital up and down conversions, filtering and decimation or interpolation, directly in the URSP2.

The digitized signal and the USRP2 configuration and control commands transit through a gigabit Ethernet interface connected to the host computer. Because of bandwidth limitation of the gigabit Ethernet interface the maximum sample frequency is 25Ms/s.
Multiple USRP2 can be connected together, thanks to a dedicated interface called MIMO expansion, to share sampling clock and local oscillators, allowing fully coherent MIMO operations.
A 10 MHz reference input allows locking the master oscillator of the USRP2 on an external clock. A 1 pulse per second (1PPS) input allows absolute timing operations.

A variety of daughterboards, plugged directly onto the USPR2, provides the RF front-end to the USPR2, and allows the reception/transmission of signals with a carrier frequency from DC to 5 GHz, each daughterboard covering a specific frequency band.

In the presented test bench, only the reception chain of two USPR2 is used and the chosen daughterboard is the WBX (see picture on Figure 4.6). This daughterboard, that permits to receive signal between 50 MHz and 2.2 GHz with a bandwidth up to 40 MHz, is adapted to the French DVB-T signal bandwidth and carrier frequency (see Table 2.7). It also proposes an amplifier with an adjustable gain from 0 to 31.5 dB, with a noise figure between 5 and 7 dB.
Two USRP2 are used in a Master/Slave configuration. The Master USRP2, locked to the GPS time thanks to the 10 MHz and 1PPS signal of the GPS receiver, is connected to the host PC through the gigabit Ethernet interface. The Slave USRP2 is connected to the Master with the MIMO cable, to have the same timing as the Master (thus it is also locked to GPS time). In addition, the digitized signal of the Slave USRP2 passes through the MIMO cable to be sent to the host PC through the gigabit Ethernet interface at the same time as the digitized signal of the Master USRP2.

Figure 4.5: Picture of one USPP2

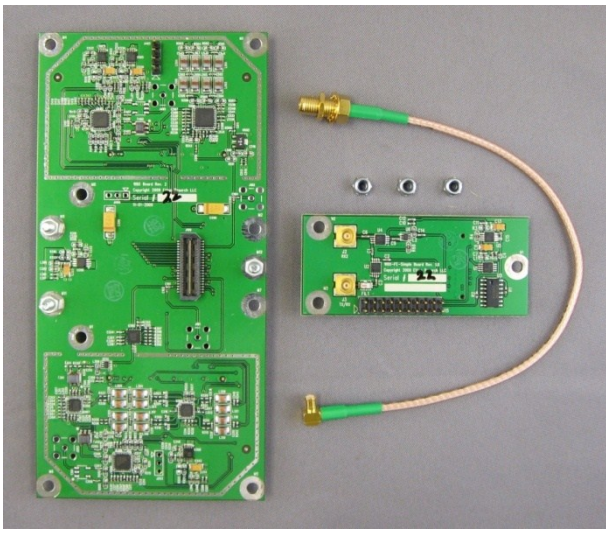

Figure 4.6: Picture of one WBX daughterboard

GPS receivers

The first GPS receiver, is a Novatel OEM4 ProPak-G2, is used for two purposes:

- Record on the host PC, connected through a serial communication interface, a variety of logs with in particular:
  - The position computed by the receiver every second (LOG ONTIME 1 BESTPOS)
  - The difference between the computed GPS time and the internal clock every second (LOG ONTIME 1 TIME)
- Provide the Master USRP2 with the 10 MHz and 1PPS signal. On this receiver, the internal clock is steered on the computed GPS time, thus the 10 MHz and 1PPS output have also with some limitations:
  - The 10 MHz signal is directly supplied by the internal clock and, because of some latency in the steering process, it is not always perfectly synchronized on computed GPS time. However, the TIME log permit to know the difference between the computed GPS time and the internal clock, which can be corrected a posteriori on the estimated delay.
  - The 1 PPS output is generated directly with the computed GPS time with no latency as for the 10MHz output.
  - Both 10 MHz and 1PPS outputs depends on the quality of the computed GPS time which is available only if a position fix is possible and whose accuracy depends on the reception conditions. Under correct reception conditions it is known that the standard deviation of the computed GPS time error is about 5 to 10 meters (about 0.15 to 0.3 µs).

A u-blox EVK-5T GPS receiver, is used to record the GPS position during the tests. Since this receiver is known to have a better sensitivity than the Novatel one, it will be used to obtain the reference position in urban environments.

4.1.2 Description of the signal recording software

The main purpose of the developed signal recording software is to configure the couple USRP2/WBX with the desired parameters (carrier frequency, sampling frequency, amplifier gain…). It is then used to record the desired signal directly on the hard drive. By doing so, the ranging method can be implemented in post-processing and the recorded signal can be processed as many times as wanted. The counter-part is that the limit of the HDD speed for writing could be reached if the desired sampling frequency is too high. In addition, to allow for absolute PR measurements, the software must also store the precise GPS time of the first sample of the recorded signal.

The signal recording software uses an open-source driver under GNU GPLv3 license, called USRP Hardware Driver (UHD) developed by Ettus Research to specifically control the USRP2 (and other Ettus Research‘s products). It takes the form of a C++ library with high level classes to configure and control easily the URSP2 without thinking of the flow control or the Ethernet communication.

Figure 4.7 shows the structure of the developed Signal Recording Software. Boxes with double lines represent functions from the UHD library.

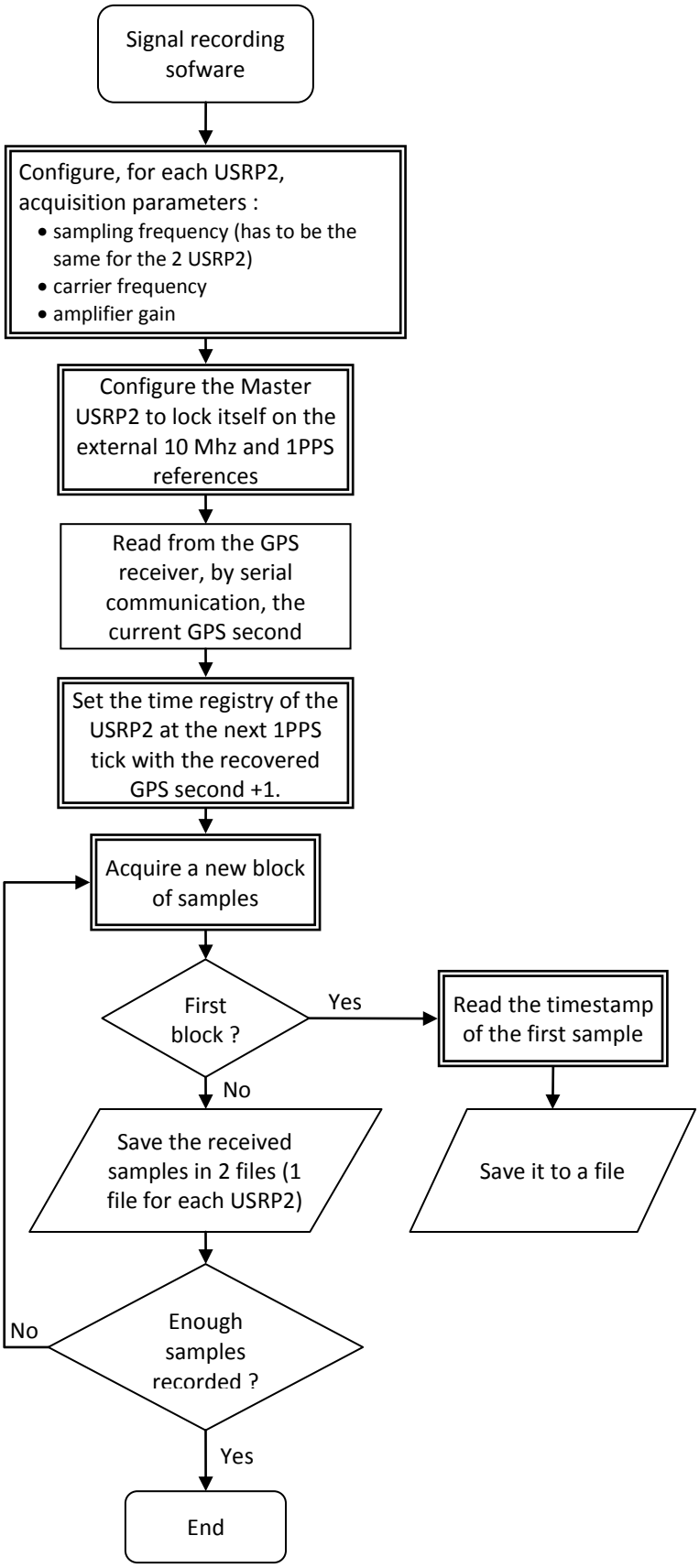

Figure 4.7: Structure of the signal recording software

In the first block of Figure 4.7, the desired sampling frequency, carrier frequencies and the amplifier gains are configured, for each USRP2, using UHD functions.

In the second block, an UHD function is called to make the Master USRP2 lock on the external 10 MHz and 1PPS references coming from the GPS receiver. As the Slave USRP2 is connected to the Master with the MIMO cable, it is automatically configured to lock on the Master USRP2 clock.

In the third block, the current GPS second is read on the COM port by calling a specific log on the GPS receiver. Then, an UHD function that permits to initialize the time register with any value at the next 1PPS tick, is called with the retrieved current GPS second + 1 second. Since this time register is updated every 10 ns (the period of the master clock) and since the master clock is locked on the GPS time, the time register always contains the current value of the GPS time (within 10 ns).

Finally, a block of samples (with an arbitrary size) is read from the USRP2 using a UHD function. If it is the first received block, the time of the first sample of this block, coming from the USRP2 time register and encapsulated in the metadata of the block of samples, is written in an output file. Next, the received samples are saved in two output files (one for each USRP2) or just one if the second optional USRP2 is not used. Then the next block of samples is acquired and so on until the desired recording duration is reached.

4.1.3 Description of the signal processing software

The signal processing software is composed of two subprograms, both developed in C++:

- a resampling program, that resamples the recorded signal using the sampling frequency of the considered DVB-T signal (64/7 MHz in this case), in order to make all the DVB-T receiver algorithms introduced in section 2.3 work and
- a ranging program, following the algorithm described in section 3.1

The binary files that have been generated by the signal recording software (one file if only one reception chain is used, two file if the two reception chains are used), are processed one after the other by the two signal processing programs.

4.1.3.1 Description of the resampling program

The sampling frequency of the USRP2 is set with a decimation factor, thus, it has to be a sub-multiple of the master sampling frequency, 100 MS/s. According to the useful bandwidth of the received DVB-T signal of about 8 MHz, the highest decimation factor respecting Shannon theorem is 12 leading to a sampling frequency $F_{e,1}$ equaled to $\frac{100\ \mathrm{MS/s}}{12} \approx 8.33\ \mathrm{MS/s}$

According to Table 2.7, the considered DVB-T signal has a native sampling frequency $F_{e,2}$ equals to $\frac{64\ \mathrm{MS/s}}{7} \approx 9.14\ \mathrm{MS/s}$. Some operations of an OFDM receiver, e.g. the FFT demodulation, can't work if

this native sampling frequency is not matched by the receiver. Thus, the recorded signal has to be resampled to this sampling frequency.

Here, the sampling frequency of the recorded signal has to be augmented from 8.33 MS/s to 9.14 MS/s.

The algorithm that makes this translation uses a direct and inverse discrete Fourier transforms (DFT and iDFT) and is quite simple:

- Chose two integer n and p such as : $\frac{n}{F_{e,1}} = \frac{p}{F_{e,2}}$
- Compute the complex DFT of n samples of the signal to resample
- Zero-pad the result of the DFT to have a p-sized vector
- Compute the complex iDFT of this zero-padded vector to obtain the resampled version of the signal
- Continue with the next n samples of the signal to resample

Figure 4.8 shows the block diagram of the resampling program that uses this algorithm to resample the recorded files. This program generate two output files: one for the real part of the complex resampled signal (channel I) and one for the imaginary part of the complex resampled signal (channel Q).

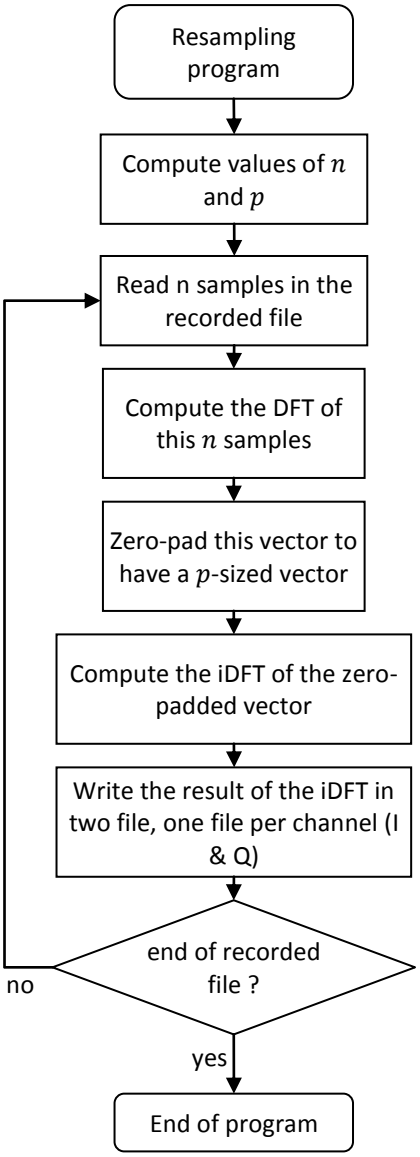

Figure 4.8: Structure of the resampling program

4.1.3.2 Description of the ranging program

The ranging program permits to process the resampled version of the DVB-T signal recorded by the USRP2 to acquire and track the correlation peak delays. Figure 4.9 shows the block diagram of this program that follows the procedure described in the section 3.1.

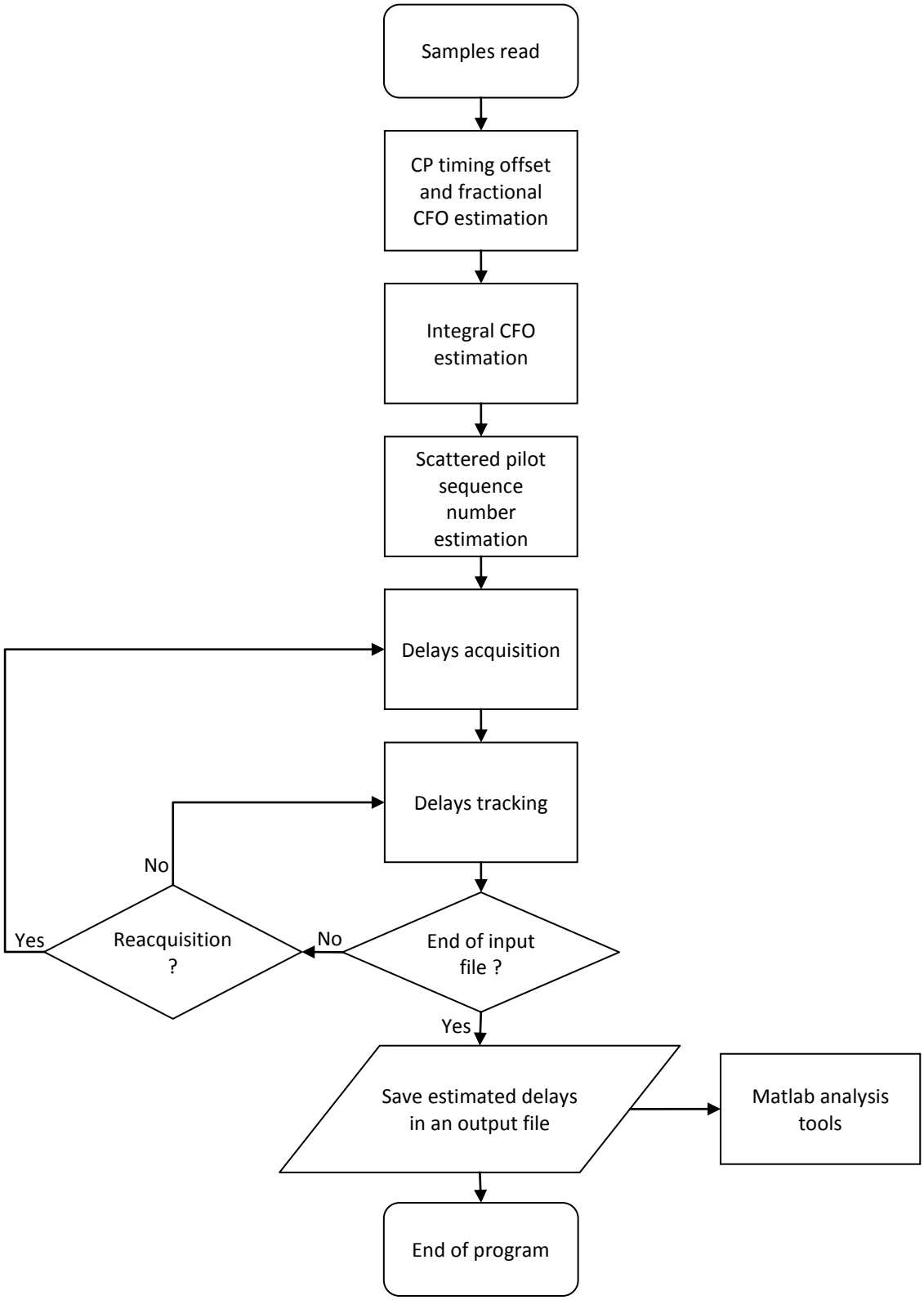

Figure 4.9: Structure of the ranging program

The three firsts blocks are classical functions of a DVB-T receiver described in sections 2.3.1, 2.3.2 and 2.3.3. Then, the acquisition of the received signals' delays is done as described in section 3.1.3.1 and, next, they are all (or a subset) tracked as described in 3.1.3.2. Until the end of the input file, the

tracking of the replicas continues. In addition, periodical delays reacquisitions are possible. Once the end of file is reached the estimated delays for the entire input file are saved to be analyzed with Matlab.

This delay tracking program does not include a continuous estimation of the CFO or the SCO using the algorithm described in section 2.3.4. Indeed, its presence was not required, since in the conducted tests, the CFO variation was small enough that a single estimation of the CFO at the beginning of the recorded signal was sufficient. Similarly, the SCO value was so small that its estimation and correction was not necessary.

In the following, the operation of each block is described in detail.

CP timing offset and fractional CFO estimation

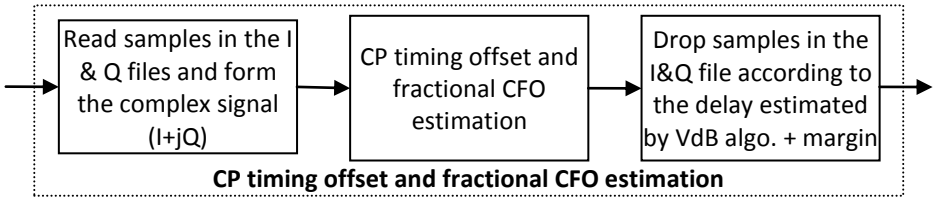

First samples are read in the input files and the complex signal is formed. Then, the CP timing offset and fractional CFO estimation is done according the algorithm explained in section 2.3.1. The timing offset is corrected by dropping samples in the input files according to the estimated timing offset plus a demodulation margin.

Integral CFO estimation

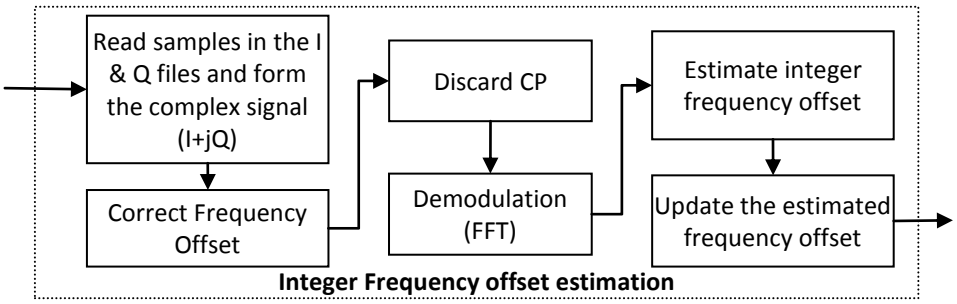

First samples are read in the input files and the complex signal is formed. The CFO is corrected according to the value found in the CP algorithm. The CP is discarded and the FFT demodulation is done. Then, the integral CFO is estimated according to the algorithm described in section 2.3.2 and added to the value of the fractional CFO found with the CP algorithm.

Scattered sequence number estimation

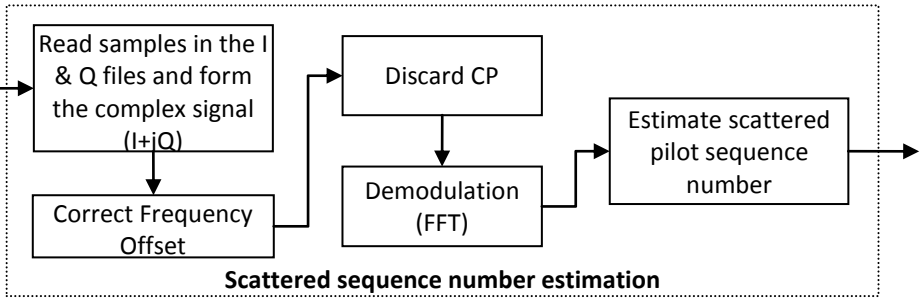

First samples are read in the input files and the complex signal is formed. The CFO is corrected, the CP is discarded and the FFT demodulation is done. Then, the scattered pilot sequence number is estimated according the algorithm explained in section 2.3.3.

Delays acquisition

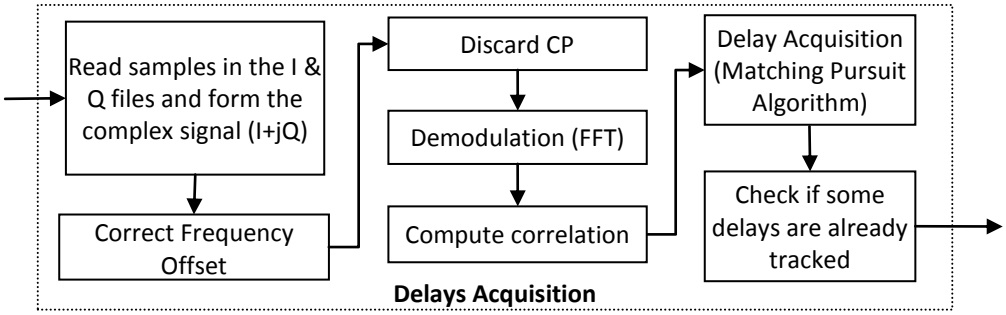

First samples are read in the input files and the complex signal is formed. The CFO is corrected, the CP is discarded and the FFT demodulation is done. Then, the correlation is computed and the correlation peaks delays are estimated using the matching pursuit algorithm as described in section 3.1.3. If it's a reacquisition, a function checks if some of the delays found are already tracked and discard them.

Delays tracking

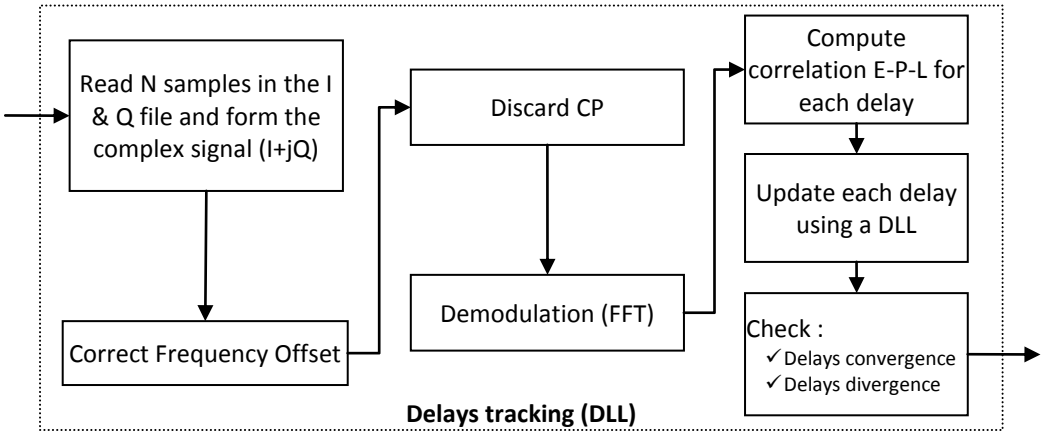

First samples are read in the input files and the complex signal is formed. The CFO is corrected, the CP is discarded and the FFT demodulation is done. Then the early, prompt and late correlation points are computed for each tracked delay and a DLL update is performed according to the algorithm described is section 3.1.3.2. Finally, some checks are done on the tracked delays to detect delays convergence or delays divergence.

4.2 Software Validation

In this section the ranging program is validated on a simulated DVB-T signal in, fisrt, an ideal scenario and then in more realistic scenario. In order to validate the C++ implementation, its results are compared to the Matlab implementation, which is considered as the reference implementation because of the simplicity of the Matlab language that limits development errors.

4.2.1 Ideal scenario

For this scenario, the synthetic DVB-T signal whose parameters are depicted in
Table 4.1 is generated without any impairment. The ranging program parameters used in the C++ and Matlab version are shown in Table 4.2.

Table 4.1: Parameters of the generated DVB-T signal - Ideal scenario

Parameters	Value
Mode – FFT size	8K - 8192
CP ratio	1/8
Approximate bandwidth – Sampling period	8 MHz – 7/64 µs
Timing Offset	0 sample
Carrier Frequency Offset	0 subcarrier spacing
SNR	Infinite (no noise)

Multipath delays	{0} (only one path, with a null delay)
Multipath relative amplitudes	{1}

Table 4.2: Parameters of the ranging programs (C++ and Matlab) – Ideal scenario

Parameter	Value
Van de Beek algorithm - Number of summations	1
Integer frequency estimation - Number of summations	1
Scattered pilot sequence detection - Number of summations	1
Delays acquisition - Number of summation	1
Delays acquisition - Number peak to detect	1
Delays acquisition – Correlation window	Rectangular
Delays tracking – Loop order	2
Delays tracking – Loop bandwidth	1 Hz
Delays tracking – Number of summation	1

Table 4.3 shows several results of the C++ and Matlab program compared to the true value. It can be seen the two programs find the same result . The unique difference between the true and the estimated value is for the estimation of the timing offset which is totally normal since the Van de Beek metric has a strong random component, even in absence of noise, due to the randomness of the data symbols.

Table 4.3: Comparison of true values with C++ and Matlab results

Parameters	True Value	C++ Program	Matlab program
Timing offset	0 sample	2 samples	2 samples
Fractional CFO	0	0.000375147	0.000375147
Integer CFO	0	0	0
Scattered pilot sequence number (of the 1st OFDM symbol)	0	0	0
Estimated peak delay	0 sample	0 sample	0 sample

Finally the following figures show with more details the results obtained with the C++ and the Matlab programs for the different algorithm. Figure 4.10 shows the metric used in the Van De Beek algorithm (Eq. (2.24)), Figure 4.11 shows the metric used in the integer frequency estimation (Eq. (2.30)), Figure 4.12 shows the metric used in the scattered pilot sequence detection (Eq. (2.32)) and Figure 4.13 shows the correlation function used for delays acquisition. It can be seen that the C++ result match perfectly the Matlab result, thus validating the C++ implementation.

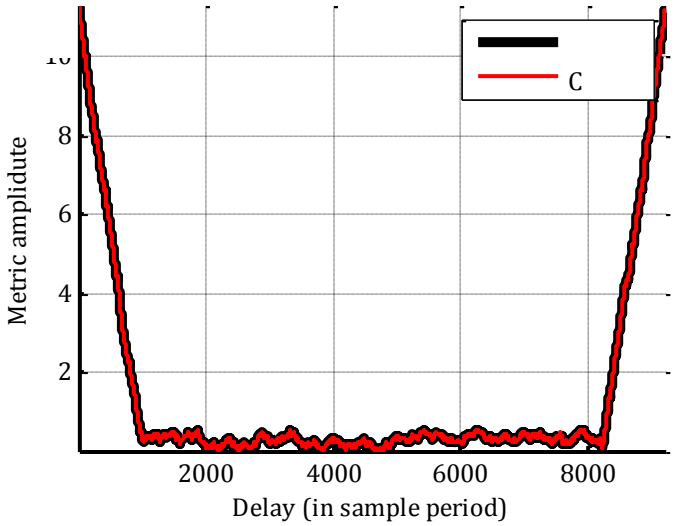

Figure 4.10: Van de Beek metric

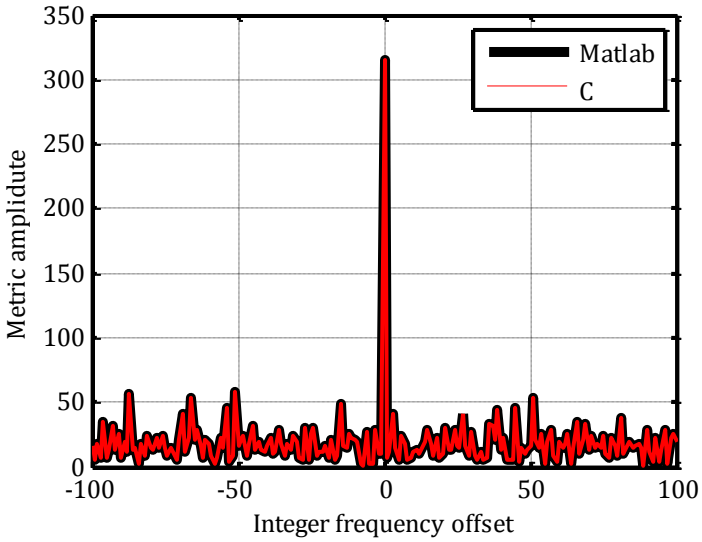

Figure 4.11: Integer frequency estimation metric

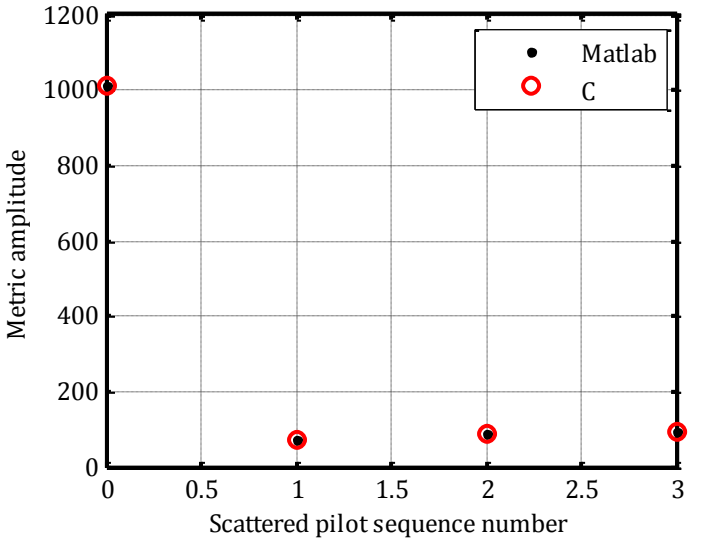

Figure 4.12: Scattered pilot sequence detection metric

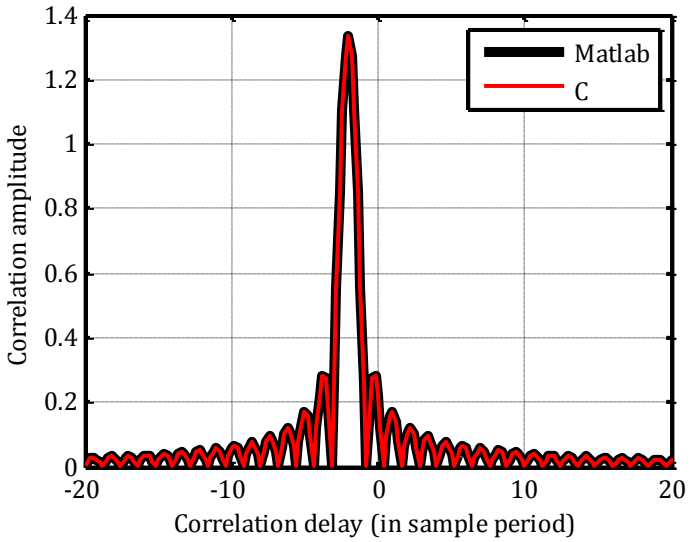

Figure 4.13: Absolute correlation function used for delay acquisition

4.2.2 Realistic scenario

For this scenario, the synthetic DVB-T signal whose parameters are depicted in Table 4.4 is generated with several impairments to approach a real signal. The propagation channel, slightly simpler than a real one, presents 3 replicas, the second one having the larger amplitude. An evolution of the timing offset of 5 m/s is simulated for all replicas. The ranging program parameters used in the C++ and Matlab version are shown in Table 4.5.

Table 4.4: Parameters of the generated DVB-T signal - Realistic scenario

Parameters	Value
Mode – FFT size	8K - 8192
CP ratio	1/8
Approximate bandwidth – Sampling period	8 MHz – 7/64 µs
Timing Offset at Origin	0 sample
Timing Offset rate	5 meters/second
Carrier Frequency Offset	2.1 subcarrier spacing
SNR	-5 dB
Multipath delays	{0;10;50} samples
Multipath relative amplitudes	{1;2;0.8}

Table 4.5: Parameters of the ranging programs (C++ and Matlab) – Realistic scenario

Parameter	Value
Van de Beek algorithm - Number of summations	10
Integer frequency estimation - Number of summations	10
Scattered pilot sequence detection - Number of summations	10
Delays acquisition - Number of summation	1
Delays acquisition - Number peak to detect	1
Delays acquisition – Correlation window	Rectangular
Delays tracking – Loop order	2
Delays tracking – Loop bandwidth	1 Hz
Delays tracking – Number of summation	1

Table 4.6 shows several results of the C++ and Matlab program compared to the true value. It can be seen the two programs found the same result. Here again only the timing offset estimated by the Van de Beek algorithm presents a slight difference with the real value due to multipathes.

Table 4.6: Comparison of true value with C++ and Matlab results

Parameters	True Value	C++ Program	Matlab program
Timing offset	0 sample	10 samples	10 samples
Fractional CFO	0.1	0.104247	0.104247
Integer CFO	2	2	2
Scattered pilot sequence number (of the 1st OFDM symbol)	2	2	2
Estimated peak delays	{0, 10, 50} samples	{0, 10, 50} sample	{0, 10, 50} samples

Figure 4.14 shows the estimated delays for each multipath for the Matlab and C++ program. It can be seen that the 2 programs give the exact same result. In addition, Figure 4.15 shows the tracking error (difference between the estimated delays and the true delays). It can be seen that the estimated delays correspond to the true delays except a small bias due the influence of sidelobes between peaks. Indeed the correlation function of one replica is distorted by the correlation functions of the two other (in particular their sidelobes), impacting the discriminator and thus the delay estimate. Since the relative delays between replicas are constant, the distortions of the correlation peaks are stable and the delays tracking error is constant.

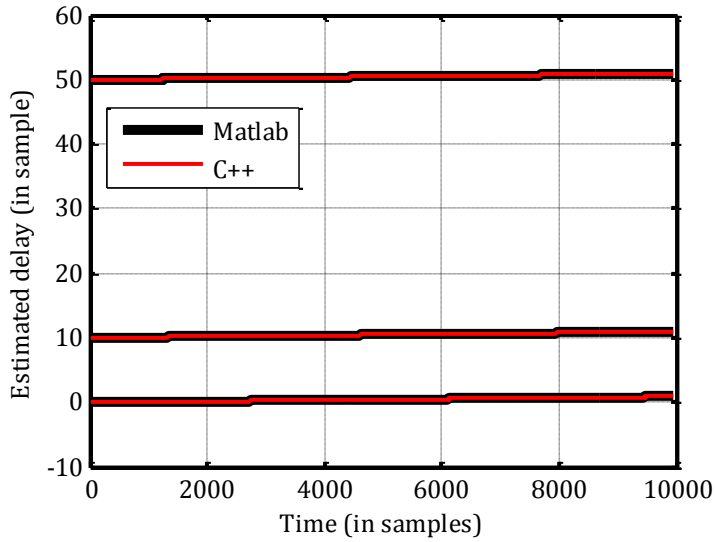

Figure 4.14: Comparison of estimated delays by the C++ and the Matlab programs

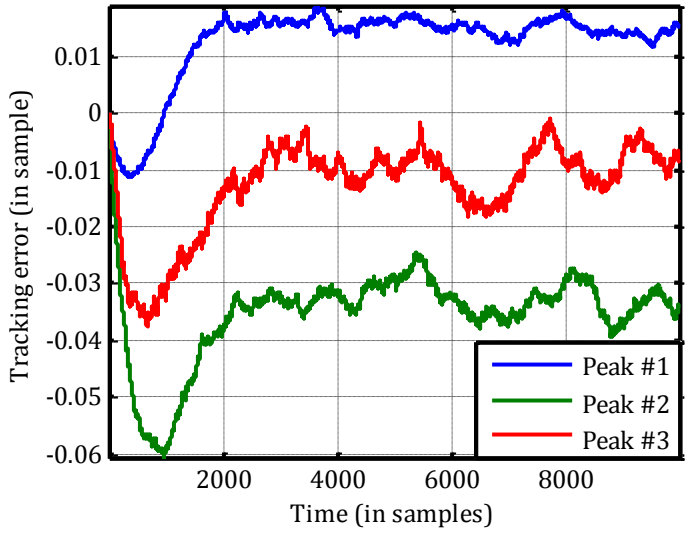

Figure 4.15: Tracking errors for each tracked peak

4.3 Validation of the USRP2 synchronization on an external reference

The synchronization of the URSP2 on a external reference has been validated by performing a recording of a GPS signal generated by a Spirent GPS signal generator while the clock reference input of the USRP2 was connected to the 10 MHz output of the Spirent generator, as shown on Figure 4.16.

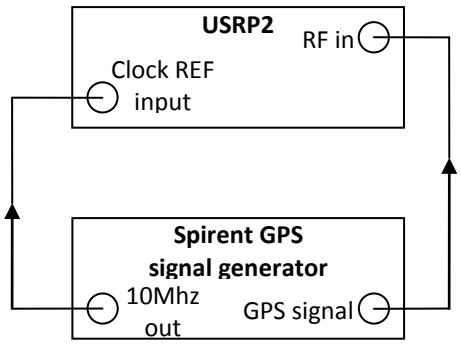

Figure 4.16: Synchronization validation set-up

The GPS signal was generated using a Spirent application that permits to generate a GPS signal with just one PRN code, no Doppler, no data and a fixed delay. Thus, if the USRP2 synchronization is efficient, the processing of the GPS signal recorded by the USRP2 must produce constant delay estimation. Figure 4.17 shows the result of the delay tracking of the recorded GPS signal obtained with a basic GPS software receiver.

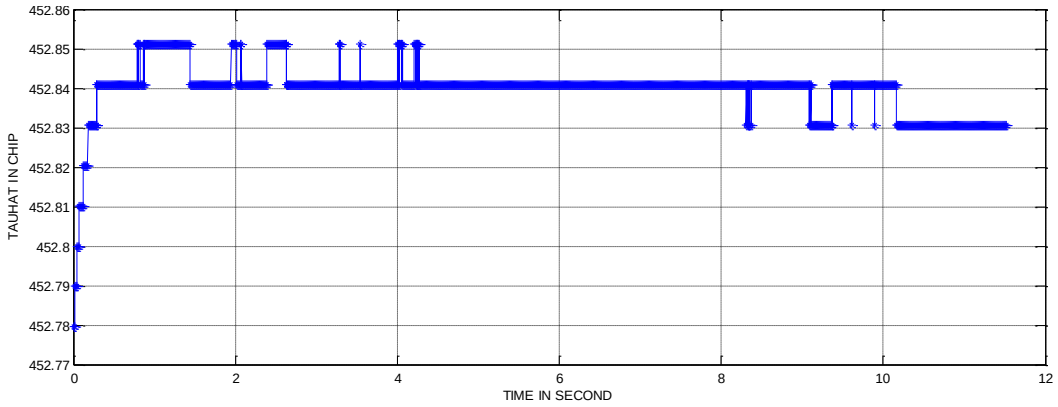

Figure 4.17: Result of delay tracking of the GPS signal recording with a synchronized USPR2

After a transition period, the estimated delay converges clearly to a constant value (at ±0.01 chip = ±3 meters), thus validating the URSP2 synchronization on an external clock reference within an acceptable precision.

5 Performance of the Pseudo-Range Estimation Method in Sub-urban, Urban and Indoor Environments Using Real Signal, in MFN

In this chapter, the results of tests on real signals, using the test bench exposed in section 4.1, are presented. Urban and indoor environments are explored.

The goal of these tests is to quantify the performance of the PR estimation on real signals and to conclude on the interest of the method. but not to validate the whole tracking strategy including multiple DLL, DLL exclusion and selection or reacquisition presented in section 3.1.3. Thus, for these tests, DLL exclusions and selections were done “manually”. In addition, the re-acquisition process is not used because it was not relevant in these tests (most of the time the tracking was maintained continuously on the shortest peak).

First of all the three possible DVB-T emitters tested and used are presented and the timing calibration process of the GPS time-synchronized emitter is presented.

5.1 Choice and timing calibration of the DVB-T emitter

Because the designed test bench do not permit to acquire more than two signals from two emitters in multi-frequency networks (MFN), which emit on different frequencies, it is not possible to compute a position. In addition, emitters of a MFN are not normally synchronized between them which prevent us from obtaining a position using TOA measurements without estimating the emitters relative oscillator drift, even if enough in-sight emitters are available.

Thus, the performance of the developed ranging method has to be analyzed in the range domain instead of the position domain. Consequently, the pseudorange measurements have to be clock-error-free. For that purpose it is necessary to have emitters synchronized on GPS time. If such an emitter can be found, its timing has to be calibrated in order to obtain a bias-free pseudo-range measurement comparable with a reference range.

5.1.1 Choice of the DVB-T emitter for real signal test

The test location is Toulouse, France. At this location, the reception of three different DVB-T emitters is possible. Each of the three emitters, called “Pic du Midi”, “Bonhoure” and “Pic de Nore”, emits on six channels of 8 MHz wide. Figure 5.1 shows the location of the three DVB-T emitters and of the tests location and Table 5.1 shows the different parameters for each emitter. It can be seen that the “Bonhoure” emitter is the local emitter of the city of Toulouse, whereas “Pic de Midi” and “Pic de Nore” emitters are regional emitters.

Figure 5.1: Emitters positions around the test place

Table 5.1: Emitters characteristics

Emitter	Pic du Midi	Bonhoure	Pic de Nore
Emitting power	13 kW	2 kW	8 kW
Approximate distance from the zone of test	130 km	5 km	80 km
Channels #	22, 26, 36, 48, 50, 54	49, 51, 52, 53, 55, 56	31, 57, 59, 60, 62

It is reminded that the central frequency of a channel can be deducted from the channel number using the following formula:

$$474\text{Mhz} + (k - 21).8\text{Mhz} + f_{\text{offset}} \tag{5.1}$$

where:

- k is the channel number
- $f_{\text{offset}} = 166.667$ kHz a spectrum protection offset

In order to choose which emitter(s) can be used for real signal testing, an analysis of the synchronization of each of one was done. For this purpose the following figures show the estimated delay for each emitter using a fixed antenna placed on the roof of the ENAC TELECOM lab and the test bench synchronized on GPS time. Thus the observed delay variation represents the synchronization of the emitter with respect to GPS time. In the following example the DLL loop bandwidth is set to 100 Hz to ensure the loop convergence and only observe the emitter clock behavior.

Figure 5.2 presents the estimated delay for the “Pic du Midi” emitter on the channel 22. It can be seen this emitter is almost synchronized on GPS time, but with a small deviation. The estimated delay for Bonhoure emitter on channel 49 is shown on Figure 5.3. It can be clearly seen that this emitter is

not synchronized on the GPS time, with a delay variation of about 1 kilometer per second (about 3 ppm). Figure 5.4 shows the estimated delay for the “Pic de Nore” emitter on channel 60. For this emitter the estimated delay is centered on zero with a standard deviation of about 0.3 meters. This emitter is clearly synchronized on GPS time and will be used in the following test on this channel 60.

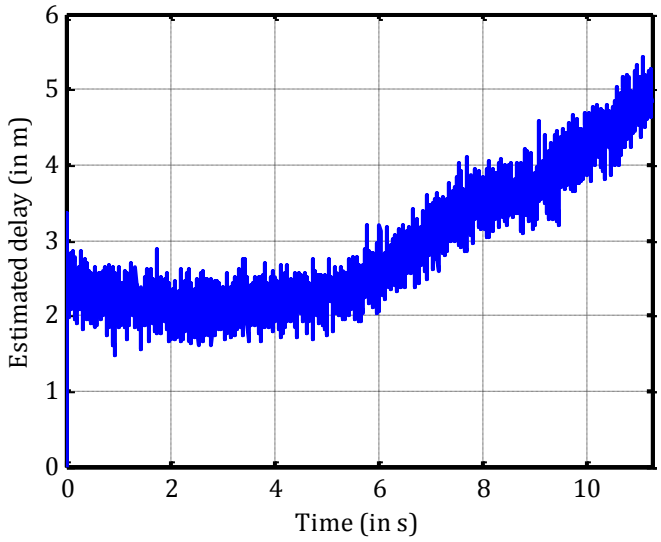

Figure 5.2: Estimated delay – “Pic du Midi” emitter – Channel 22

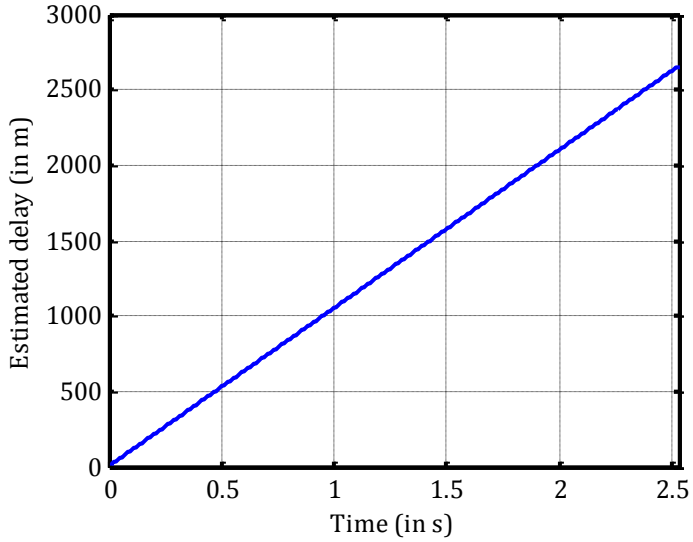

Figure 5.3: Estimated delay – “Bonhoure” emitter – Channel 49

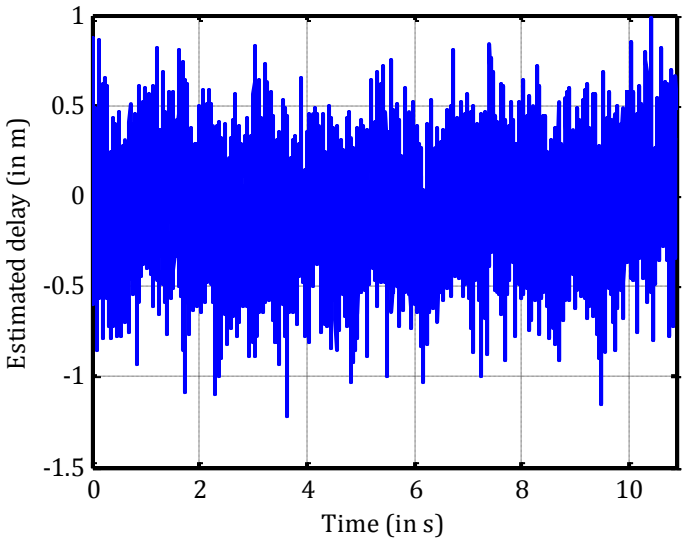

Figure 5.4: Estimated delay – "Pic de Nore" emitter – Channel 60

5.1.2 Timing calibration of the "Pic de Nore" emitter

Even if this emitter is synchronized on GPS time, it is not phase-locked on it. Indeed, the time of emission of an OFDM symbol does not match an integer millisecond of GPS time contrary to the GPS system in which each start of the spreading code coincides with a new millisecond of the GPS time. Thus, in order to obtain absolute pseudorange measurement and since only one emitter is available (not enough to solve this unknown phase offset), the instant of the OFDM symbols emission has to be determined empirically.

Ten data recordings of 5 seconds of the TV signals coming from this emitter (channel 60), have been done at a known location (determined using PPP) in direct sight of the emitter and on the top of a hill to avoid multipath error. Knowing the GPS time of the first recorded sample (thanks to a functionality of the test bench) and the exact positions of the emitter and of the receiver, and according to the delay estimated by the tracking algorithm, it is possible to determine the GPS time of the OFDM symbol emission for each recorded signal. The GPS times of the OFDM symbol emission are given modulo the OFDM symbol duration (see Table 5.2).

Table 5.2: Determination of the OFDM symbol emission time – Channel 60 of the "Pic de Nore" emitter

Test #	GPS time of the first recorded sample (in seconds in the GPS week)	Estimated delay (in sample period)	Computed value of OFDM symbol instant of emission modulo the OFDM symbol length (in sample period)

1	483282.6931	8387.02	7223.16
2	483313.8768	6286.70	7223.14
3	483341.3489	5598.41	7222.94
4	483369.8736	2767.25	7223.33
5	483400.3016	7225.57	7223.22
6	483423.5580	8744.17	7223.19
7	483449.3864	5189.99	7223.20
8	483474.5029	3153.34	7223.22
9	483497.6707	4151.88	7223.18
10	483520.8707	5320.90	7223.19

The measured GPS times of the OFDM symbol emission modulo the OFDM symbol duration are close and their mean value is 7223.18 samples with a standard deviation of 0.1 samples (3 meters). This mean value, called reference delay, is used in the following test to "transform" the estimated delay into an absolute pseudorange.

This transformation of the estimated delay into an absolute pseudorange is possible thanks to precise dating of the recorded signal obtained with the 1PPS signal from the GPS receiver used by the test bench. This precise dating consists in recording the GPS time of the first sample of the recorded file. Then, the tracking program gives an estimation of the delay between the first recorded samples and the sample of the beginning of an OFDM symbol. Thus, the GPS time of the instant of reception of OFDM symbol is deduced as the sum of the GPS time of the first recorded sample and the estimated delay. Then, as the GPS instant of emission of the OFDM symbol modulo the OFDM symbol length has been determined in the calibration process it is possible the compute an absolute pseudorange modulo the OFDM symbol length according to the following reference:

$$PR = \left(\hat{\tau} + t^{rec} - t_0^{emit} \bmod T_S\right) c_{light} \tag{5.2}$$

where:

- PR is the absolute pseudorange modulo the OFDM symbol length (in meter),
- $\hat{\tau}$ is the estimated delay between the first recorded sample and the sample of the beginning of an OFDM symbol, obtained with the tracking program (in second),
- t^{rec} is the GPS time of the first recorded sample (in second),
- t_0^{emit} is the GPS time of the instant of emission of the OFDM symbol modulo the OFDM symbol length obtained in the calibration process (in second),
- T_S is the OFDM symbol length and
- c_{light} is the celerity of light (in meter per second).

It can be seen on Eq. (5.2) that the value of the absolute pseudorange is computed with an ambiguity equals to the OFDM symbol duration. However, for the considered signal parameters, the OFDM symbol duration corresponds to a distance of about 300 kilometers. The ambiguity on the absolute pseudorange is consequently easily solved. In the following test, the distance to the "Pic de Nore"

emitter is about 80 km, thus the absolute reference position without ambiguity is directly the result of the modulo operation.

It is important to understand that this way to solve the clock error is only valid for a testing purpose. Of course for a final positioning application using OFDM signals, the clock error has to be solved as part of the positioning solution.

5.2 Urban Test

Five tests have been performed in urban environment using the test bench in its dual antenna version presented in section 4.1. In order to obtain five datasets on which the PR measurement techniques can be tested, the test bench was installed in a car. The locations of these tests voluntary avoid very hard urban environments (as urban canyon) to always ensure a correct GPS reception in order to have valid GPS time and accurate GPS position references. In these tests the reference position, obtained with a ublox GPS receiver, has an error from 4 to 6 meters (1-sigma – value estimated by the GPS receiver). These conditions are necessary to have a clock error-free PR measurement and to be able to construct a reference PR in order to assess the performance of the PR estimation technique. As explained in the previous section, the GPS-synchronized “Pic de Nore” emitter is used on the channel 60 (762,166667 MHz).

The characteristics of each recorded dataset are depicted in Table 5.3. Each dataset includes static phases, corresponding to periods where the car was stopped at a traffic light and dynamic phases, when the car was moving. To offer a better visualization of the type of environment, Figure 5.5 gives an example of trajectory for one of the five tests.

Table 5.3: Characteristics of the trajectory of the five datasets

		Dataset #1	**Dataset #2**	**Dataset #3**	**Dataset #4**	**Dataset #5**
Duration	**Static phase**	0	10 s	13 s	65 s	87 s
	Dynamic phase	99 s	82 s	47 s	235 s	98 s
Length		690 m	600 m	330 m	2000 m	830 m
Average velocity during dynamic phases		7 m/s	7.3 m/s	7 m/s	8.5 m/s	8.4 m/s

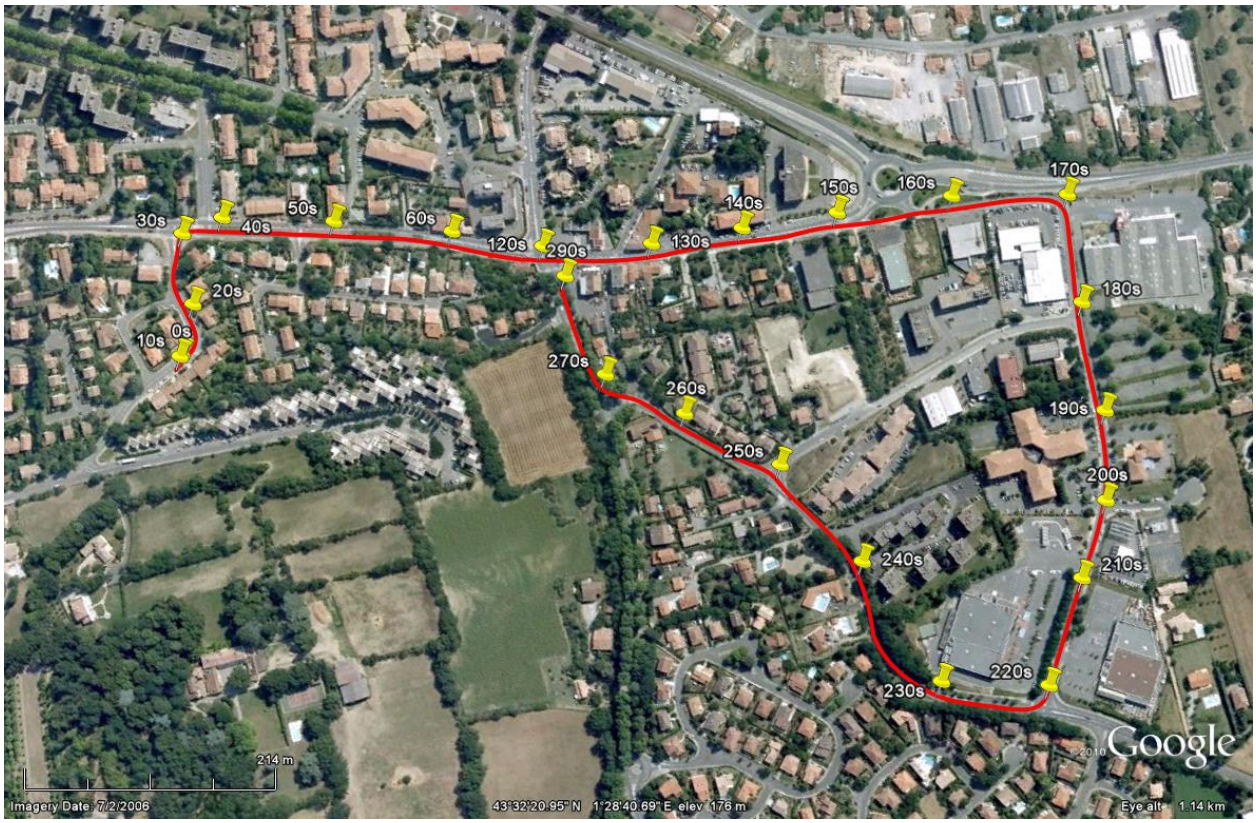

Figure 5.5: Example of trajectory – Dataset #4

The following section will present general considerations on the obtained results. A second part introduces two ways of improvement of the PR measurement based on the observations made in the first section. The last section proposes an extensive quantitative study of the performance of the PR estimation technique on the five tests for different tracking parameters (tracking loop bandwidth, number of coherent integrations and correlation window).

5.2.1 General observations on test results

Based on a a quick analysis of the results of the five tests several interesting observations can be done. These observations permit to realize the specificity of terrestrial propagation channel in urban environment. The results of this first section are obtained with the following parameters for the DLL: 1 Hz tracking loop bandwidth, 1 coherent summation and rectangular correlation window.

Figure 5.6 shows the correlation image of the antenna #1 signal, from the 1st dataset. It illustrates the evolution of the correlation function over time and thus offers a good representation of the propagation channel impulse response over time. On this figure, the reference pseudorange is also shown (represented with the black line).

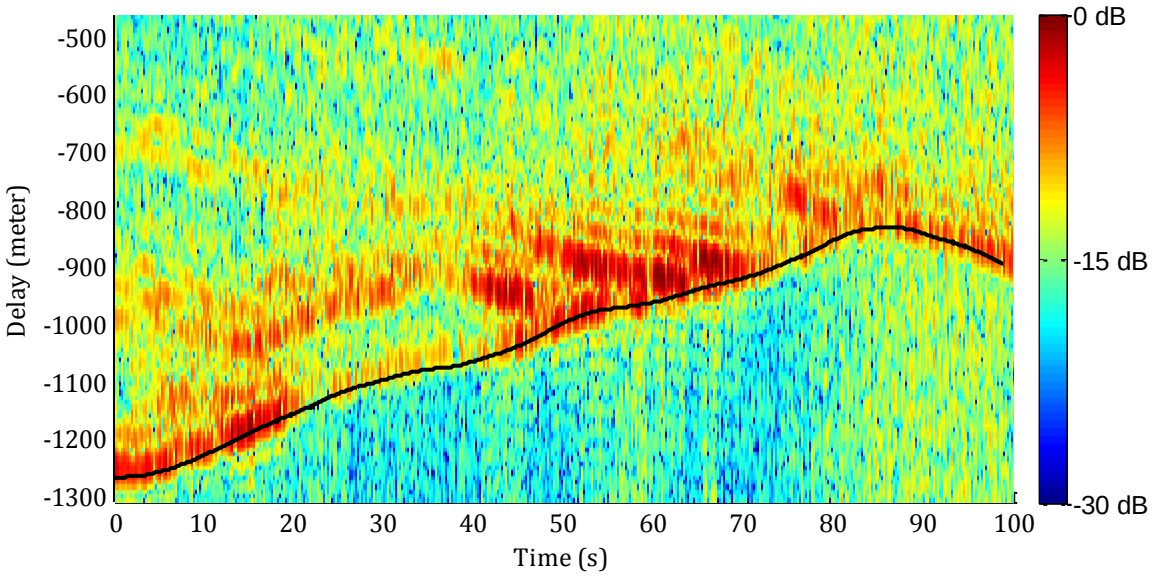

Figure 5.6: Correlation image and reference PR (black line) – Antenna #1 – 1st dataset

It can be seen that the correlation function is really disturbed during, with numerous multipathes, sometimes more powerful than the direct signal. The separation between the zone with the useful signal (orange/red colors) and the zone with noise (blue/green color) is clearly distinguishable and corresponds to the reference PR (black line). In addition, it is interesting to link the correlation image to the direct environment of the car during the test. For example, the attenuation of the direct signal visible between the 20th and the 40th second corresponds to the presence of 2 buildings near the car between the receiving antenna and the emitter, as shown on Figure 5.7. On this figure, the white line represents the trajectory of the car and the red line represents the emitter direction.

Figure 5.7: Buildings causing the attenuation of the direct signal

Another observation that can be done on the Figure 5.6 is the group of strong multipathes that converge towards the direct signal between the 40th and 70th. These multipathes are possibly due to a group a buildings on which the direct signal is reflected and towards which the car is heading for, as shown on Figure 5.8.

Figure 5.8: Building causing strong multipathes

Other observations can be done on the Figure 5.9, showing the estimated PR for antenna #1 and antenna #2 compared to the reference PR, obtained from dataset #4.

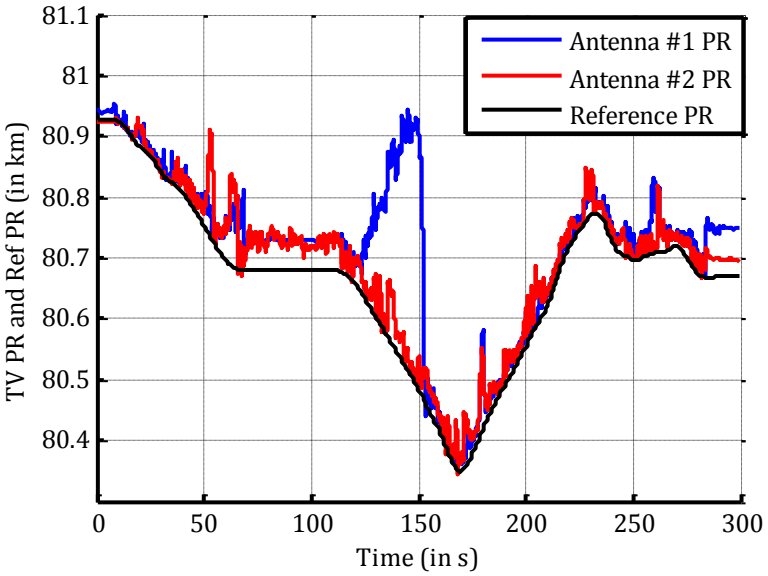

Figure 5.9: Estimated and reference PR – 4th dataset

It can be seen the PR estimation is clearly disturbed by the numerous multipathes of the terrestrial propagation channel. It also clear that the estimated PR is always longer than the reference PR, due to the numerous multipathes that attract the tracking away from the direct path. As illustrated on the Figure 5.10, the PR error (difference between estimated and reference PR) is mostly positive leading to an important positive bias, but sometimes reaches zero. This positive error is often called non-line-of-sight (NLOS) error in telecom world translating the error is PR measurement due to the absence, or at least the weakness, of the line-of-sight signal. Table 5.4, gathering all the mean values of the PR error for the 5 dataset and the 2 antennas (10 values on total), shows that this behavior is systematic and is comprised between 25 to 90 meters.

Table 5.4: Mean PR error for the 5 datasets

	Dataset #1		**Dataset #2**		**Dataset #3**		**Dataset #4**		**Dataset #5**	
Mean value of PR error (in meter)	28	32	24	43	34	33	64	25	86	24

The second observation that can be done looking at the Figure 5.9 is that the PR estimated by each antenna is very different even if the 2 antennas are very close, raising the possibility to exploit antenna diversity. This is confirmed by the Figure 5.11 showing the difference between the PR of antenna #1 and #2.

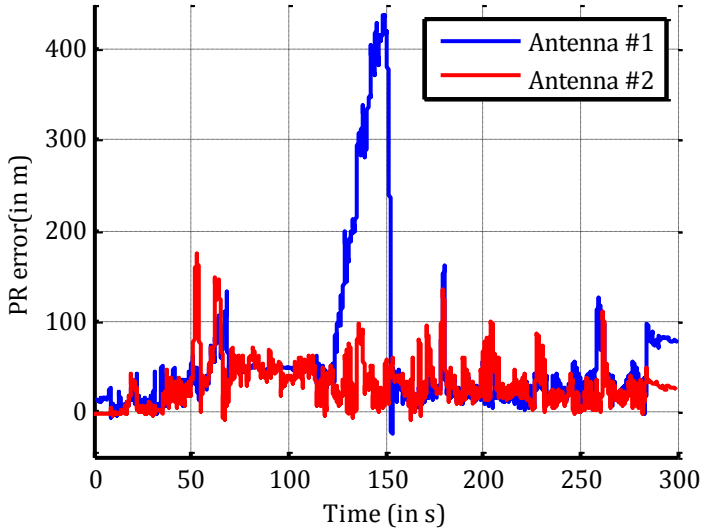

Figure 5.10: PR error for antennas #1 and #2 – 4th dataset

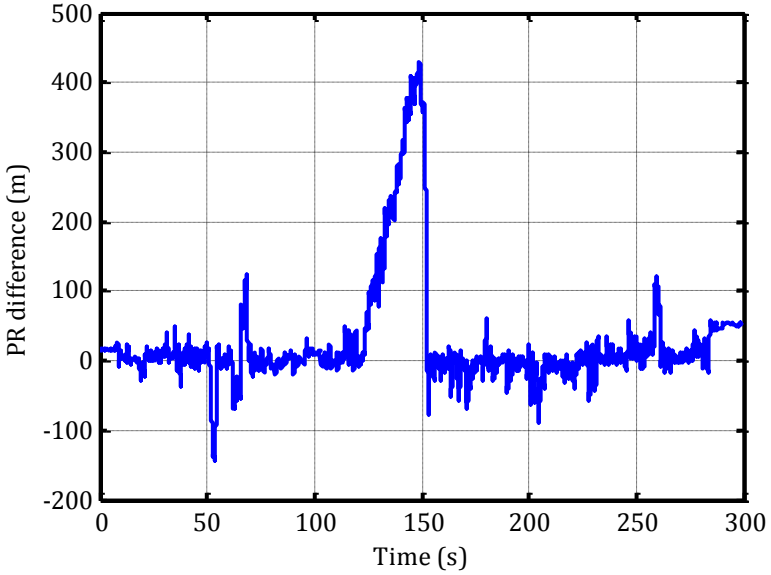

Figure 5.11: Difference between PRs of antenna #1 and antenna #2 – 4th dataset

The last observation concerns static phases. Indeed they can be easily distinguished from dynamic phases, by a much smaller PR error standard deviation. To illustrate this, Figure 5.12 represents a close-up on the correlation image during a static phase. Reference PR (black) and estimated PR (red) are also represented. It can be seen that during a static phase the correlation function is very stable (in contrast to dynamic phases) and thus the PR estimate also (4 meters of PR error standard deviation in this example). In addition during static phases the PR error may present an important bias. For these reasons, static phases will not be considered in the computation of performance metrics (PR error mean value and standard deviation) in order not to distort results.

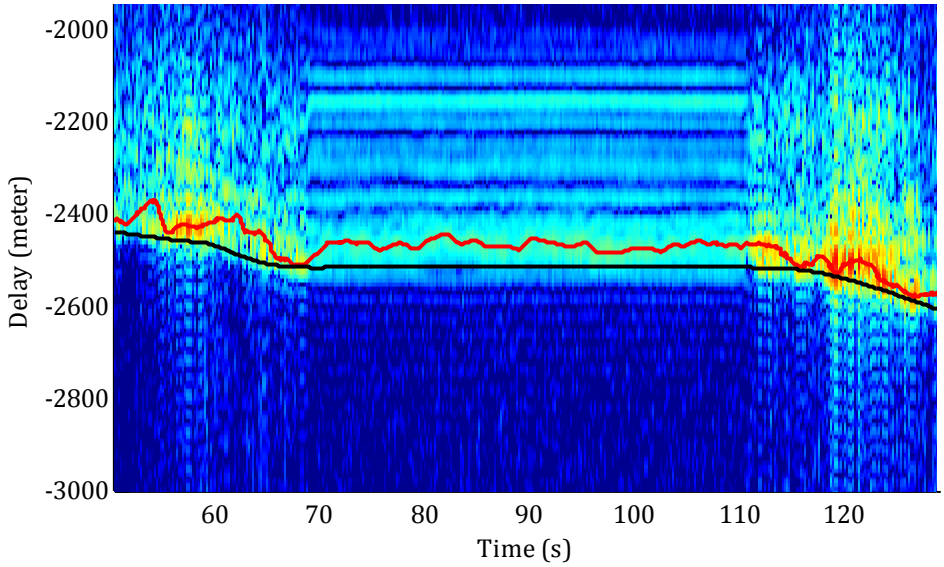

Figure 5.12: Correlation image – Close-up on a static phase – Dataset #4

5.2.2 PR estimate improvement

Two techniques have been considered to improve the PR measurements, based on the two last observations mode in the previous section:

- the PR error is mostly positive (NLOS error) but sometime reaches zero
- the PR on the two antennas are very different

The natural approach to improve the PR estimation precision given two independent measurements from two antennas would be to make their average. However, since the PR error on each antenna is mainly positive, due to the NLOS propagation most of the time, it was noticed that taking the minimum of the two measurements was clearly better.

This is confirmed by results shown in Table 5.5 that gathers the mean value and standard deviation of the PR error for the measurements of each antenna, for the mean of the measurements and for the minimum of the measurements. The results are given for the 4th dataset and for dynamic phases only since static phase presents a PR estimate almost constant and would distort the results.

Table 5.5: Comparison of raw PR error with mean and minimum technique – 4th dataset

PR error	Antenna #1 – Raw PR errror	Antenna #2 – Raw PR errror	Mean of two antennas	Minimum of two antennas
Mean (m)	63 m	25 m	44 m	21 m
Standard deviation (m)	102 m	18 m	53 m	15 m

It can be seen that the minimum technique outperforms the mean technique. It shows an improvement of the mean PR error of more than 65 % for antenna #1 and of 15 % for antenna #2 and an improvement of the standard deviation of the PR error of about 80 % for antenna #1 and 15 % for antenna #2.

The other interest of taking the minimum of the PRs of the two antennas is to mitigate temporary drift due to a NLOS multipath affecting one of the two antennas. For example, looking at Figure 5.9, the PR estimate of the antenna #1 is drifting to a multipath between the 120th and 150th second, but not the antenna #2. Thus, using the "minimum of two antennas" technique this drift is mitigated.

A second natural way of improving PR estimates would be to filter the PR estimate, that is to say averaging it over of a time window of given size. Here again, instead of taking the average it could be better to take the minimum over this time window. This technique is illustrated on Figure 5.13, showing a close-up view on the PR estimate for antenna #2. On this figure, the minimum of the PR is taken on successive block of 5 second and these local minimums are interpolated to form the NLOS-error-mitigated PR.

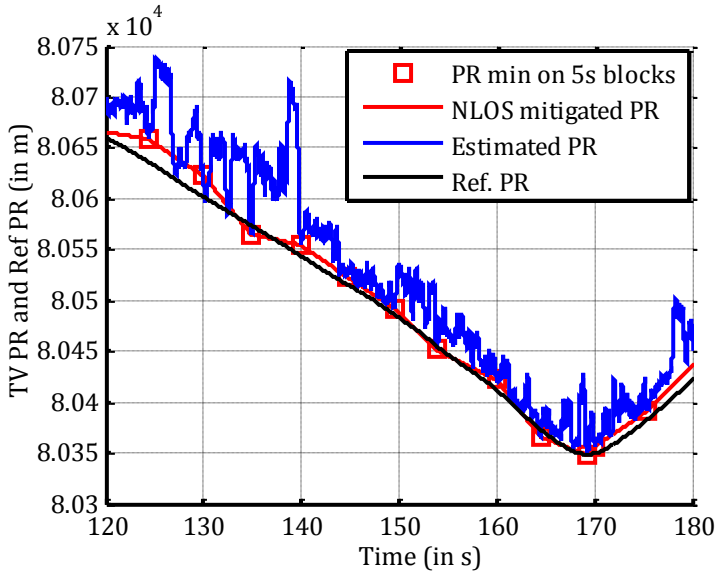

Figure 5.13: Illustration of NLOS error mitigation technique – 4th dataset

The counterpart of this technique is that it introduces a lag equal to the time window duration in the release of PR measurement (for the 5 second time windows a PR estimate is available every 5 seconds). Thus, the size of the window has to been chosen is consequence. Figure 5.14 shows the PR error statistics for Dataset #4, antenna #2, on which the minimum technique is applied with different values of the minimum window duration. It can been seen the window of 5 second offer the best performance in term of standard deviation of the PR error. For longer window, the bias NLOS error is reduced but at the expense of the PR error standard deviation and of the release lag of PR measurements. This time window of 5 seconds will be used in the following.

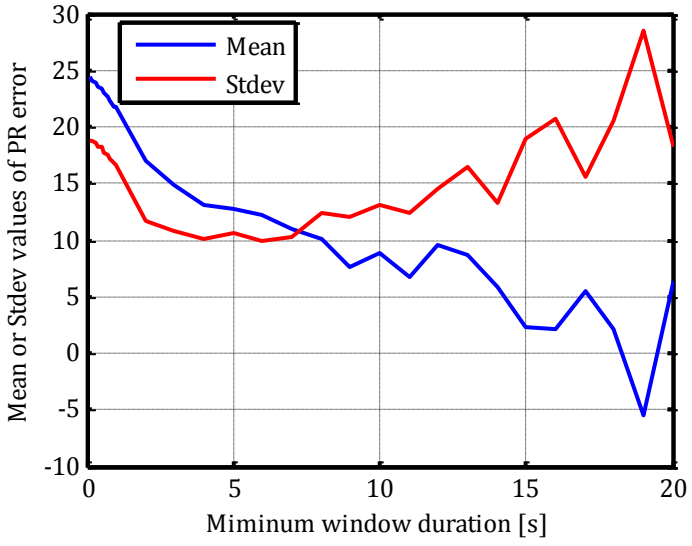

Figure 5.14: Mean and standard deviation of the PR error for different time window

Table 5.6 shows mean and standard deviation of PR error once this technique is used on antenna #1, antenna #2 PRs and on the combined antenna #1 and #2 PR as described in the "minimum of 2 antennas" technique. Here again results are shown for the 4th dataset and only in dynamic phases.

Table 5.6: Result of time window minimum technique – 4th dataset

PR error	Antenna #1 – With time window minimum	Antenna #2 – With time window minimum	Combined Antenna #1 and #2 – With time window minimum
Mean value (m)	52 m	12 m	11 m
Standard deviation (m)	96 m	10 m	10 m

The "time window minimum" technique seems to significantly improve the PR estimation performance and the best performance seems obtained when combined with "minimum of 2 antennas" techniques. The performance improvement is then of 90 % and 80 % compared to antenna #1 and antenna #2 alone for the mean value and of 90 % and 70 % for the standard deviation. Results for all datasets are presented in the following section.

5.2.3 Quantitative results for different tracking parameters

This section proposes a quantitative analysis of the tracking performance on the five recorded dataset and for different tracking parameters. The influence of three different tracking parameters (loop bandwidth, correlation window and coherent summation number) have been tested in order to underline the configuration giving the best PR estimation performance in term of (1) mean value and standard deviation of the PR error and (2) ability to maintain the tracking.

For the three influence test, the parameters listed in Table 5.7 have been used. When testing a specific parameter, the two other parameters are set to their default values, which are 1 Hz tracking loop bandwidth, rectangular correlation window and 1 coherent summation.

Table 5.7: Tracking parameters influence test configurations

Parameter	Loop bandwidth influence test	Correlation window influence test	Coherent summation number influence test
Loop bandwidth value(s) [Hz]	0.5, 1, 2, 10	1	1
Correlation window value(s)	rectangular	rectangular, hamming, blackman-harris	rectangular
Coherent summation number value(s)	1	1	1, 10, 100

A complete analysis of all the results for all the test configurations and for all the datasets does not permit to highlight a best set of tracking parameters. Indeed, because of the important random component of the terrestrial propagation channel in urban environment, a set of parameter can give the best performance for a particular dataset and not for another. The complete dataset results can be found in 0.

However an orientation for the choice of the tracking parameters can be given. First, the tracking loop bandwidth must not be too high. Indeed, with an important loop bandwidth, the channel perturbations are quickly followed and the risk too jump from the shortest peak to a longer peak is important. As an example, Figure 5.15 shows the PR error for the 1 Hz loop bandwidth (left) and for the 10 Hz loop bandwidth for both antenna and for the dataset #1.

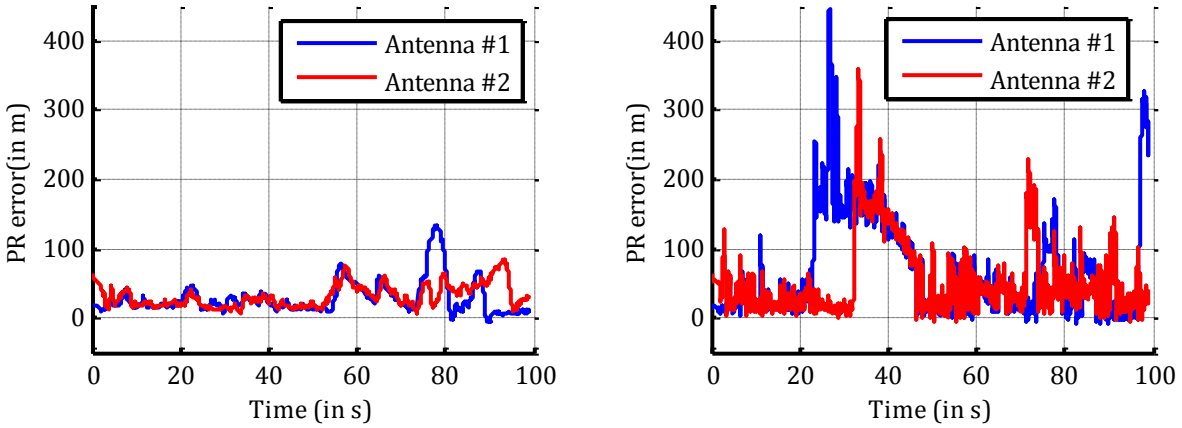

Figure 5.15: PR error for both antennas for 1 Hz loop bandwidth (left) and for 10 Hz loop bandwidth – dataset #1

The second trend which emerges from the complete tracking parameter influence analysis is that a too important coherent summation number, even if it is beneficial for the noise reduction, appears to be a handicap on the final tracking performance. A possible explanation is that an important number of coherent summations can lead to destructive correlation if the phase coherence is not maintained during the summation interval, which is the case if the direct signal is not present and if

only multipathes (which have a random phase) are tracked. For example, Figure 5.16 shows the correlation image, the reference PR (black line) and the estimated PR (blue line) for the antenna #2 and for dataset #2, with 1 coherent summation (up) and 100 coherent summation (down). It can be seen on this figure, even if the noise floor is significantly lower (about 10 dB) in the 100 coherent summations case, the correlation peak amplitude is also reduced, leading to a loss of tracking around the 35th second in the 100 coherent summation case contrary to the 1 coherent summation case.

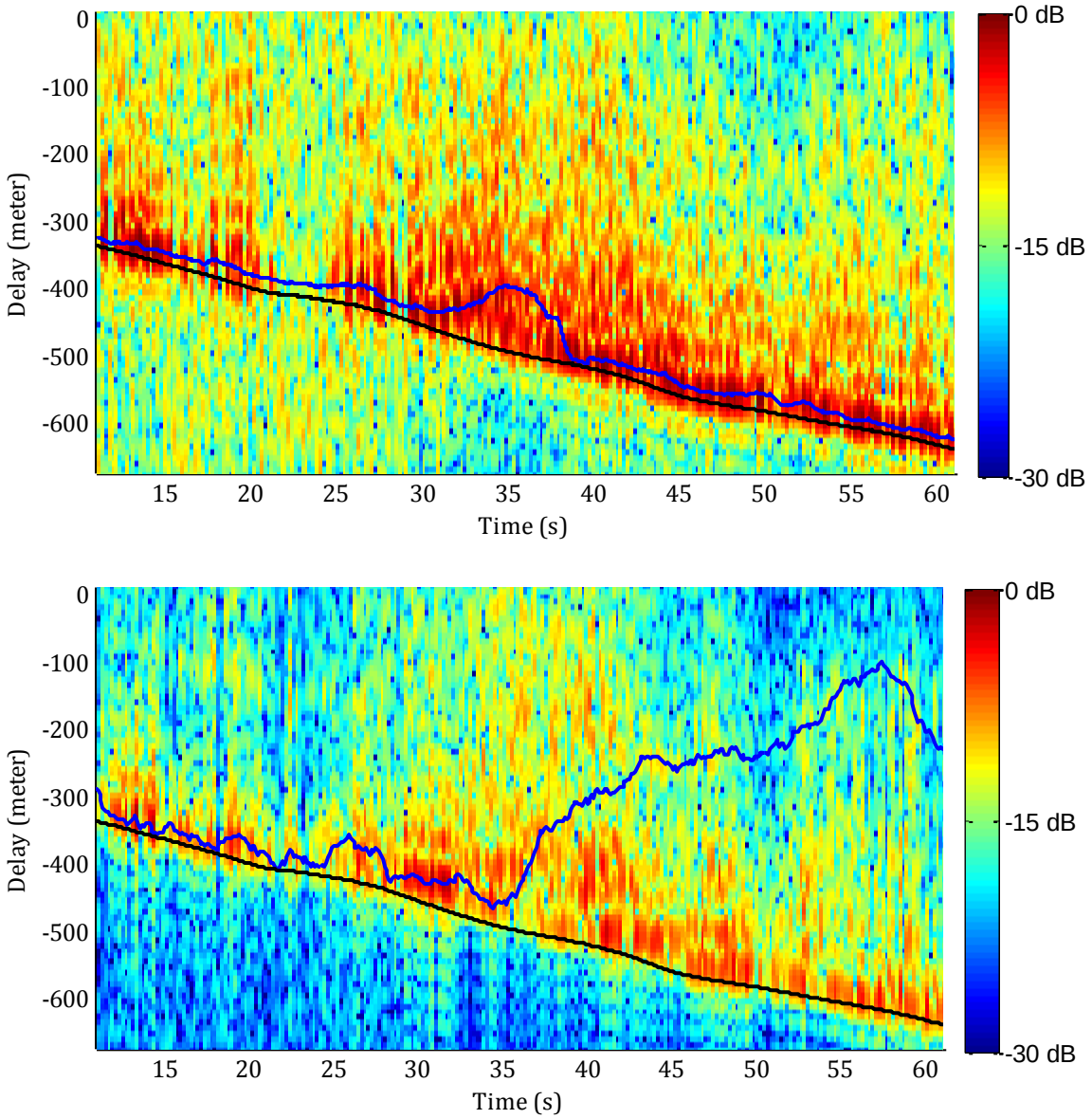

Figure 5.16: Correlation image, ref PR (black line) and estimated PR (blue line) for 1 coherent summation (up) and for 100 coherent summations (down) – Antenna #2 – Dataset #2

In order to give an idea of the best tracking parameters, the tracking performance has been assessed using the "minimum of two antennas" PR improvement technique. This choice has been done

because this technique permits to mitigate temporary large error on one of the two antenna PR measurement that could produce unrepresentative error on the final statistics.

Table 5.8 gathers for each set of tracking parameters and for each recorded dataset the mean value and the standard deviation of the PR error. Static phase of the trajectories are excluded to compute statistics. The table cells are colored from soft yellow to red, from the lowest value to the highest.

Table 5.8: Mean value and standard deviation of the PR error using the "minimum of two antennas" technique

"Minimum of two antennas" Window type, loop bandwidth, summation number	**Dataset #1**		**Dataset #2**		**Dataset #3**		**Dataset #4**		**Dataset #5**	
	mean [m]	**std [m]**	**mean [m]**	**std [m]**	**mean [m]**	**std [m]**	**mean [m]**	**std [m]**	**mean [m]**	**std [m]**
Rect, 1 Hz, 1	22	14	23	17	27	9	21	16	17	15
Hamming, 1 Hz, 1	23	20	21	17	25	9	22	17	29	39
BH, 1 Hz, 1	25	22	19	12	25	10	18	15	27	25
Rect, 0.5 Hz, 1	29	18	26	20	26	7	24	18	16	14
Rect, 2 Hz, 1	26	20	23	19	23	16	22	19	16	16
Rect, 10 Hz, 1	38	44	21	16	32	30	20	18	62	86
Rect, 1 Hz, 10	22	14	23	17	31	14	23	19	19	15
Rect, 1 Hz, 100	28	15	24	16	34	12	23	25	53	43

From this table it is not really possible to highlight a set of tracking parameter from another. However, two tracking parameters produce higher errors: the 10 Hz loop bandwidth and the 100 coherent summations. To sum up this performance figure Table 5.9 shows the mean value and standard deviation of the PR error averaged over the five dataset.

Table 5.9: Average value of PR error mean and standard deviation when the "Minimum of two antennas" technique is used

"Minimum of two antennas"	**Average value over the five datasets**	
Window type, loop bandwidth, summation number	**PR error mean [m]**	**PR error std [m]**
Rect, 1 Hz, 1	22	14
Hamming, 1 Hz, 1	24	20
BH, 1 Hz, 1	23	17
Rect, 0.5 Hz, 1	24	15
Rect, 2 Hz, 1	22	18
Rect, 10 Hz, 1	34	39
Rect, 1 Hz, 10	24	16
Rect, 1 Hz, 100	33	22

According to this table, the tracking parameter set {rectangular window, 1 Hz loop bandwidth 1 coherent summation} permit to reach the better tracking performance, on average, even if the difference with other parameter set is tiny. The mean value of the PR error is 22 meters and the standard deviation is 14 meters.

The same analysis can be done using the two PR improvement techniques: the “minimum of two antennas” combined to the “time window minimum”. Then the averaged results of Table 5.10 are obtained, considering a time window of 5 second for the minimum computation.

Table 5.10: Average value of PR error mean and standard deviation when the "Minimum of two antennas" and the “time window minimum” technique are used together

"Minimum of two antennas" + “Time window minimum” (5s window)	**Average value over the five datasets**	
Window type, loop bandwidth, summation number	**PR error mean [m]**	**PR error std [m]**
Rect, 1 Hz, 1	11	9
Hamming, 1 Hz, 1	11	9
BH, 1 Hz, 1	9	9
Rect, 0.5 Hz, 1	16	9
Rect, 2 Hz, 1	6	8
Rect, 10 Hz, 1	1	14
Rect, 1 Hz, 10	12	9
Rect, 1 Hz, 100	16	10

With the two PR improvement techniques combined, all the tracking parameters give similar performance in term of PR error standard deviation (about 9 meters) expect for the 10 Hz loop bandwidth which present a larger standard deviation (14 meters). Concerning the mean value of the

PR error, it is improved by increasing the loop bandwidth and small coherent summation number. This is normal since a high loop bandwidth augments the allowed dynamic of the PR measurements, which have more chance to approach the direct signal, which positively impact the “time window minimum” technique. In the same way long coherent integration reduce the dynamic by an averaging phenomenon.

To conclude, when the “minimum of two antennas” is combined to the “time window minimum” the better compromise is to use a loop bandwidth of 2 Hz and a very good PR estimation can be obtained with only 6 meters of positive bias and 8 meters of standard deviation, on average.

5.3 Indoor Test

The test presented in this section present the tracking performance in indoor environment. Since a precise GNSS positioning is not possible indoor, no reference PR could be available contrary to the urban environment test. Thus, the tracking performance can only be analyzed qualitatively and not quantitatively.

5.3.1 Test presentation

This test takes place in the first floor of a concrete building, in Toulouse, France, at about 81 km from the TV emitter. It has been made with the single TV antenna version of the test bench because of hardware availability constraints. The GPS receiver is connected to an antenna placed on the roof of the building to provide a precise the GPS time reference to the test bench which is therefore fixed. Thus to make dynamic measurements, the TV antenna is connected to the test bench with a 10m-cable thus limiting the movement in the building at a radius of about 20 meters around the test bench.

The test lasts about 36 seconds, beginning by a static phase of about 11 seconds (from 0s to 11s) near a window oriented towards the TV emitter, followed by a dynamic phase in deep indoor (passing through a room without a window) of about 15 seconds (from 11s to 26s) and ending by another static phase of 10 seconds (from 26s to 36s);

Figure 5.17 shows the sat view of the start and end points of the test with the direction of the TV emitter represented by a white line. The approximate range between the TV emitter and the start and the end points, determined with the Google Earth distance measurement tool, are also specified. As it can be seen on this figure, even if the travelled distance is close to 20 meters, the PR variation between the start and the end point is about 11 meters.

Figure 5.17: Sat. view of the test configuration

The TV emitter is the same that in the urban environment tests ("Pic de Nore" emitter) but the channel #31 (554.166667 MHz) is used instead of the channel #60, to have a better indoor reception (low frequencies have a better penetration in buildings).

5.3.2 Results analysis

Figure 5.18 shows the image correlation of the recorded signal. The first static phase, near a window is clearly visible, then the dynamic phase induce important variation of the correlation function but the signal is still clearly visible, despite the deep indoor environment. For the last static phase the signal is very weak but still visible.

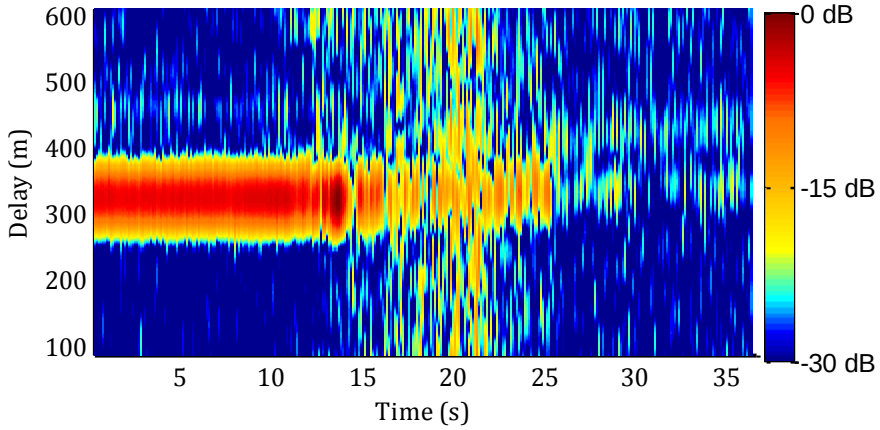

Figure 5.18: Correlation image ($N_C = N_I = 1$)

Figure 5.19 shows the variation of the estimated PR. Since no reference PR is available the PR estimate is initialized at zero to have a better visualization. The tracking parameters used are those determined in the previous section: 1 Hz loop bandwidth, rectangular window and 1 coherent summation.

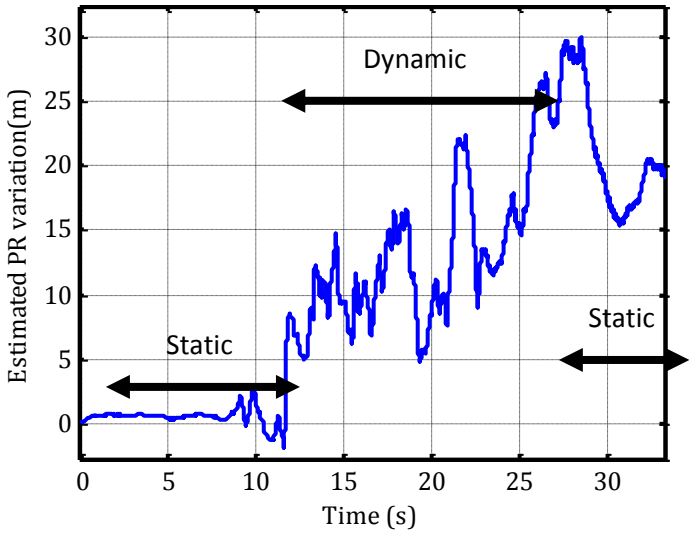

Figure 5.19: Variation of estimated delay

The first static phase is clearly visible, with a null variation of the PR. On the opposite, the PR variation during the final static phase is very important, because of the low signal power (and so important noise) as visible on the correlation image of Figure 5.18.

The total PR variation between the start and the end of the record is about 15 meters, which is bigger that the real PR variation which has been estimated at about 9 meters. This can be explained since multipathes surely bias the PR measurements during the static phases. However, during dynamic the phase the variation of the estimated PR is quite small (about 5 meters) demonstrating a possible good level of performance.

The absence of reference position and the limited travelled distance do not permit to give a quantified performance of the PR estimation in indoor. Nevertheless, this experiment shows that is still possible to track the signal in indoor environment with a relatively good precision even out of the coverage of the TV service.

6 Performance of the Pseudo-Range Estimation Method in Sub-urban, Urban Using Real Signal, in SFN

This section presents the results of tests in sub-urban and urban environments using 2 emitters in single-frequency network (SFN). As explained in section 1.1.2, a SFN is very interesting from a positioning point-of-view because it allows tracking multiple signals coming from different synchronized emitters transmitting on the same frequency (only 1 tuner required). With this type of network, a new position computation strategy can be developed, using TDOA measurements instead of TOA as in mono-frequency network, thus requiring a specific performance study.

As in the previous chapter, the DLL exclusion and selection are done manually and re-acquisition process in not used, since the goal is to quantify the precision of TDOA measurements and not to validate the whole tracking processes as it could be implemented in a final positioning application.

The single antenna version of the test bench, mounted in a car, is used for these tests (the dual antenna version was not yet operational at the time of the measurement campaign). A different test location was used where two emitters are in SFN.

The first emitter is a regional emitter with an EIRP of 13 kW located on the “Pic du Midi” summit in the Pyrenees mountain. The second emitter is a small emitter with an EIRP of 24W, which is used to fill a coverage hole of the Emitter #1 in a small area of about 100 square kilometers near the small city of Auch (20000 inhabitants). This emitter is in fact a simple analog repeater of emitter #1, i.e. it receives the signal of emitter #1 with a directive antenna and reemits it after a simple amplification, without any frequency conversion but introducing an unknown delay (but small enough to avoid ISI between the signals of the two emitters). Thus, these two emitters do not form a pure SFN since the signals from the 2 emitters are not transmitted independently in a synchronized way, with a common time reference as GPS time. However, since the emitter #2 is a repeater of Emitter #1, the signal from these 2 emitters share, by construction, the same time reference, they can be considered as forming a SFN without loss of generality.

Table 6.1 shows the coordinates and principal characteristics of the 2 considered emitters. These coordinates were obtained using Google Earth and have consequently a limited precision (estimated to about 2 meters of error).

Table 6.1: Emitters parameters

	Emitter #1 “Pic du midi”	Emitter #2 “Auch”
Latitude	42°56'14.43"N	42°56'14.43"N
Longitude	0° 8'28.02"E	0° 8'28.02"E
Site height (HAE)	2886 m	276 m
Antenna height	94 m	20 m
ERP	13 kW	24 W
Carrier Frequency	706.166667 MHz	706.166667 MHz

The zone where the two tests have been done is located near emitter #2, between 2 and 6 km from it, to be in its small coverage zone and at about 100 km from emitter #1.

To illustrate the synchronization of signal from emitter #1 and emitter #2, Figure 6.1 shows the estimated delay for each emitter, the reception TV antenna being fixed. To be compared, the two delays are centered on zero (their averaged values are removed). As the test bench is fixed and synchronized to GPS time the observed delay variation corresponds to the variation of emitter’s clock with respect to GPS time. Not surprisingly, the two emitters have the same clock, but this one is not perfectly synchronized to GPS time. Thus, an absolute timing can’t be derived from the estimated delay, as in the case of chapter 1, only the variations of the estimated delays and of the reference PR (centered by removing the averaged values) will be presented in the following.

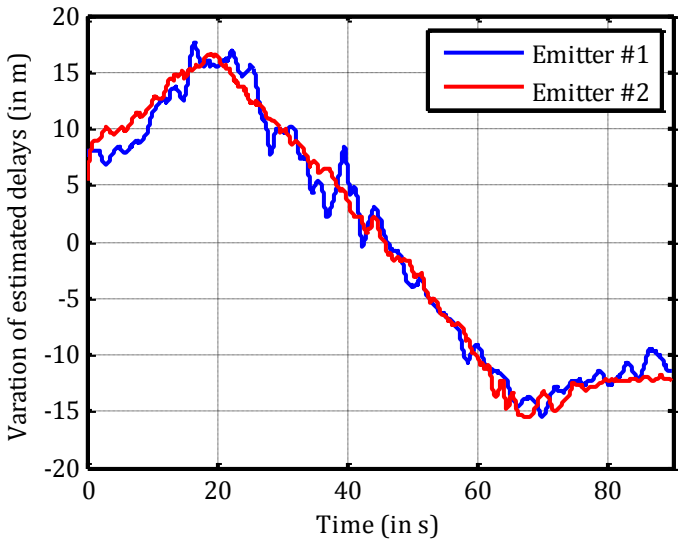

Figure 6.1: Variation of estimated delay for the 2 emitters at a fixed location

6.1 Sub-urban test

6.1.1 Test presentation

This test lasts 90 seconds and takes place on a countryside road as shown on Figure 6.2.

Figure 6.2: Sat view of the test trajectory

With the position recorded by the GPS receiver during the test and thanks to the emitters coordinates presented in Table 6.1, the reference PR can be computed for each emitter. Their variations is presented on Figure 6.3 (the mean values has been removed). The GPS position precision is about 1.5 meter (1 sigma) which is the precision of the Novatel GPS receiver in clear sky environment.

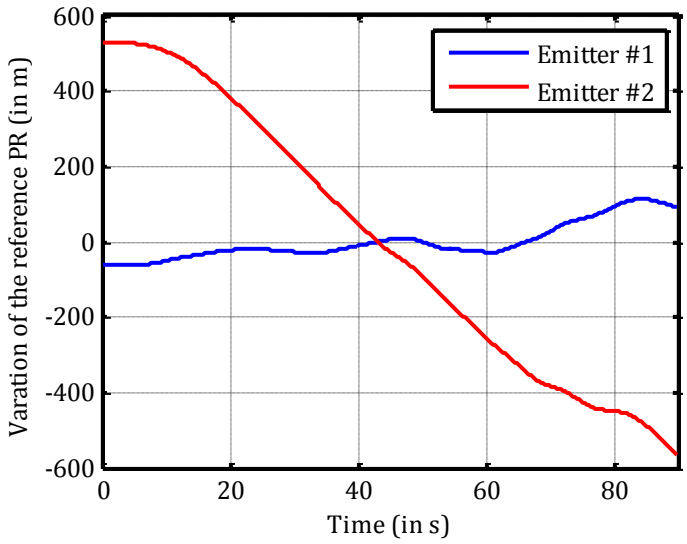

Figure 6.3: Variation of the reference PR for each emitter

6.1.2 Results analysis

Figure 6.4 shows the correlation image obtained from the correlation functions computed using a Hamming window, with 8 coherent summations and 12 incoherent summations in order to reduce noise and have a better visualization of the different received paths.

Note: the vertical band of noise that can be observed in the correlation image (e.g. between the 10th and 20th second) is due to an inexplicable behavior of the receiver (saturation, phase noise, poor electrical contact…).

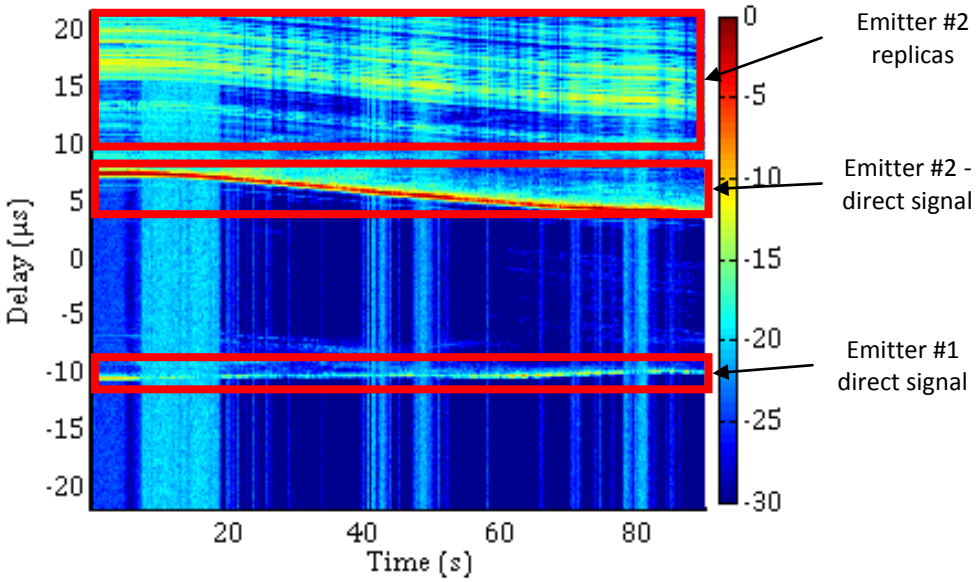

Figure 6.4: Correlation image – Sub-urban SFN

A large number of peaks appear on the correlation image. The shortest one has been identified as the signal of emitter #1. Indeed, since emitter #2 is a repeater of emitter #1, the signal of emitter #1 arrives necessarily before the signal of emitter #2. The most powerful peak, around the 5µs delay on the correlation image, corresponds to the direct signal of emitter #2. All the others identifiable peaks correspond to signal replicas of emitters #2 which are very numerous because of the feedback introduced by the signal repeating (similarly to the audio Larsen effect).

Figure 6.5 and Figure 6.6 show a closer look on each emitter peaks.

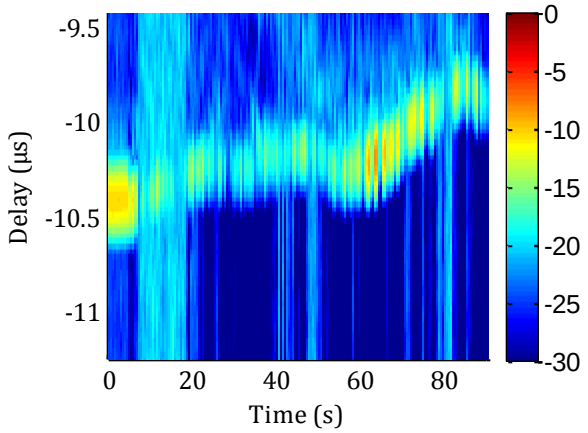

Figure 6.5: Correlation image around peak of emitter #1– Sub-urban SFN

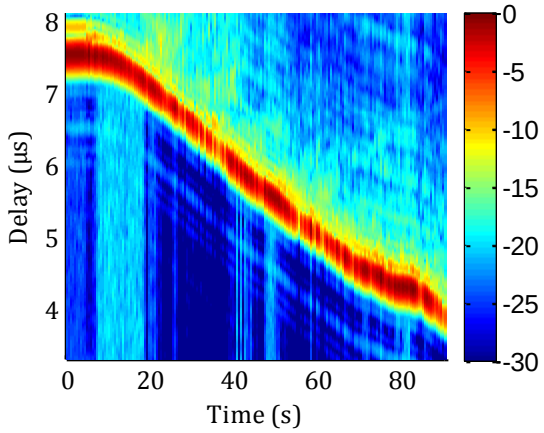

Figure 6.6: Correlation image around peak of emitter #2– Sub-urban SFN

Tens peaks have been acquired with the matching pursuit algorithm and tracked using a DLL that uses a 1 Hz loop bandwidth, a 1 coherent summation and a rectangular correlation window.

Among the 10 resulting estimated delays, the two estimated delays tracking the peaks identified in the correlation image as the direct signals from emitter #1 and emitter #2 are considered. Their variation is plotted on Figure 6.7 and compared with the variation of the reference PR.

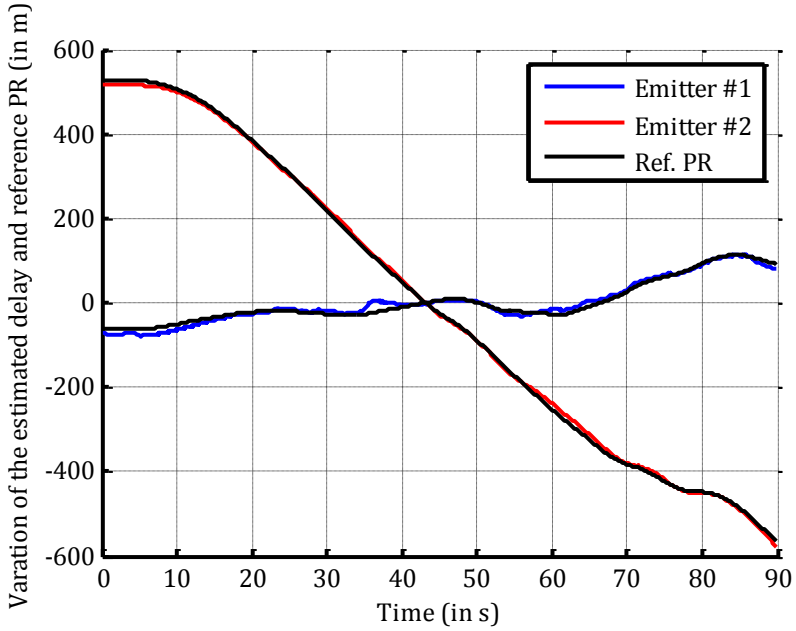

Figure 6.7: Variation of the estimated delay and comparison with the variation of the reference PR, for each emitter

The resulting tracking error variation is shown on Figure 6.8, for each emitter. Since emitters' clocks are not synchronized to GPS time, the resulting variations of the tracking error include the difference between emitter clocks and GPS time. Since the two emitters have the same clock the tracking error variation of the two emitters are similar. As the signal received from emitter #1 is weaker, its tracking error appears noisier.

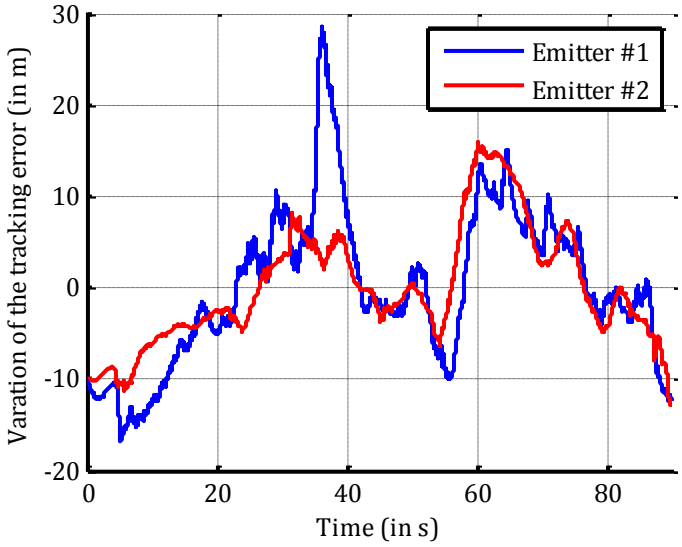

Figure 6.8: Tracking error variation, for each emitter

To deal with this clock error and have an idea of the real tracking performance, one can observe the TDOA measurement. TDOA is the time difference of arrival and corresponds to the difference between the estimated delay of emitter #1 and the estimated delay of emitter #2. As emitter #1 and emitter #2 are based on the same time reference, the TDOA measurement is clock error-free, but include a bias which is introduced by the fixed delay brought by the repeater (not only due to geometrical disposition of the two emitters but also an additional delay). This unknown delay can be estimated because TDOA are also impacted by multipathes in addition to this fixed delay. Figure 6.9 shows the variation of the TDOA measurement (the averaged value is removed) compared to the variation of reference TDOA (the averaged value is removed). The reference TDOA is the difference between reference PR of emitter #1 and emitter #2. Figure 6.10 shows the TDOA error (difference between TDOA measurement and reference TDOA). Since the TDOA error is computed with the zero-mean values of the measured and reference TDOA, its mean is also null.

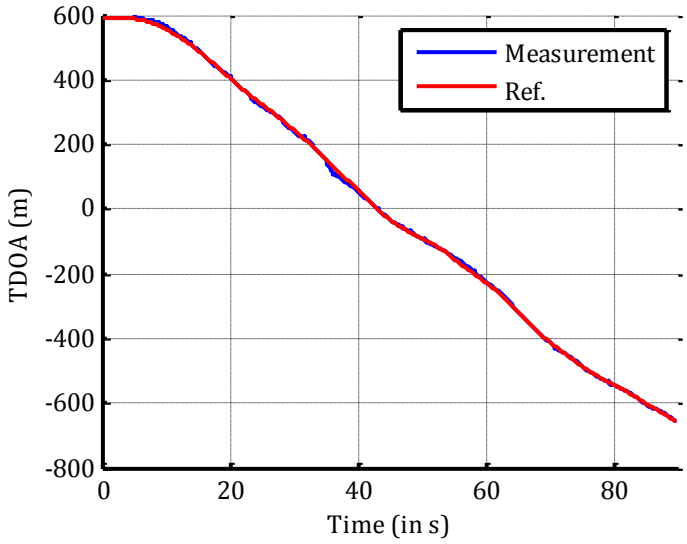

Figure 6.9: TDOA measurement compared to reference TDOA

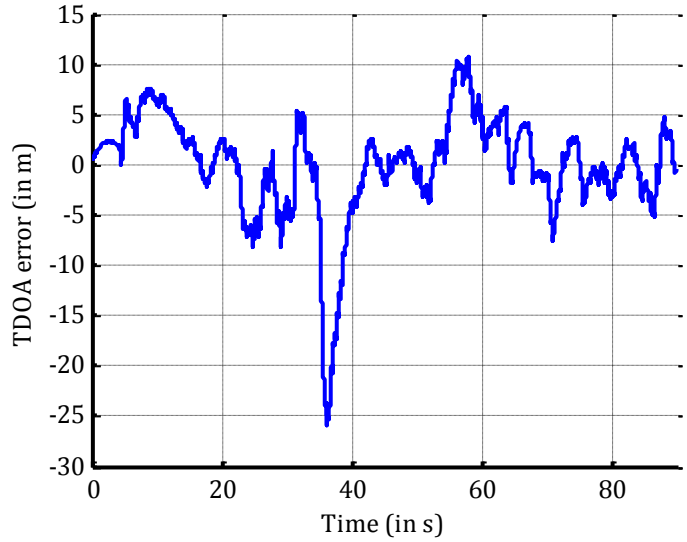

Figure 6.10: TDOA measurement error

The statistics of the TDOA measurement error are gathered in Table 6.2. As already explained, its averaged value is equals to zero by construction. Thus, it doesn't mean that there is no bias in the real (without centering) TDOA measurement.

Table 6.2: TDOA measurement error statistics

Standard deviation	5.2 meters
66% of time error	3.6 meters
90% of time error	6.8 meters
Maximum error	26 meters

The standard deviation of the TDOA error is about 5 meters which much more better that PR error standard deviation in MFN urban environment which is about 25 meters in average (raw) or 10 meters (with improvement techniques). This difference is due to the difference of environment (sub-urban instead of urban) rather than the difference of network (SFN instead of MFN).

6.2 Urban test

6.2.1 Test presentation

Figure 6.11 shows the satellite view of the trajectory of the urban test in the city of Auch that lasted 90 seconds.

Figure 6.11: Sat view of the test trajectory

As it can been seen on this figure, the precision of this reference trajectory is really poor, due to the bad reception conditions of the GPS signal. The precision of this reference trajectory is about 10 meters.

Figure 6.12 shows the variation of the reference PR for emitter #1 and emitter #2 computed from the recorded GPS position and from TV emitters coordinates.

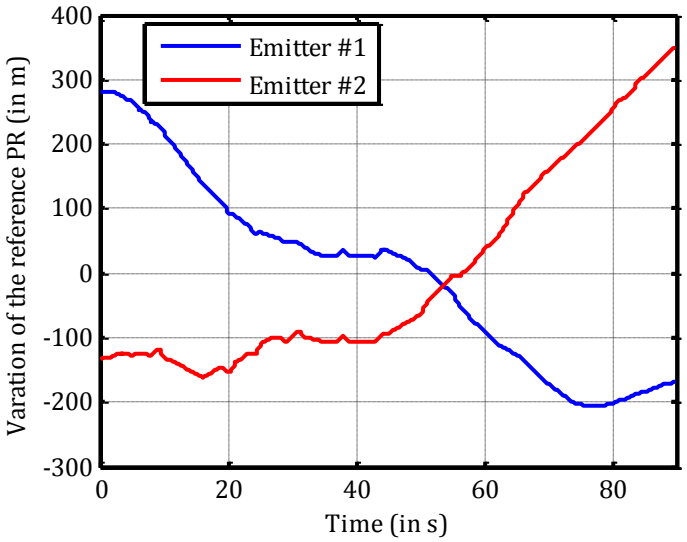

Figure 6.12: Variation of the reference PR for each emitter

6.2.2 Test results

Figure 6.13 and Figure 6.14 show the correlation image zoomed around the correlation peaks of emitter #1 and emitter #2. They are computed using 0.1 second summations ($N_C = 8, N_I = 12$) and a hamming window.

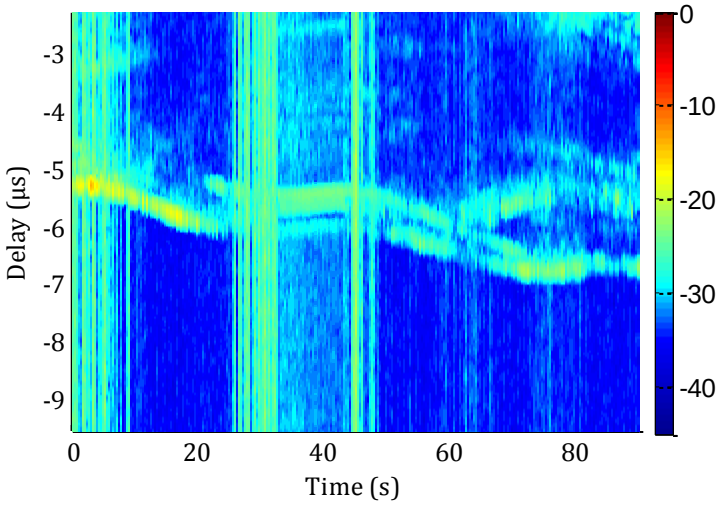

Figure 6.13: Correlation image around peak of emitter #1

The correlation peak of emitter #1 is very weak (about 25 dB under the peak of emitter #2) and is sometimes drowned by the noise . In addition a strong multipath, more powerful than the shortest peak, appearing at the 20th second, could disturb the tracking of the shortest peak.

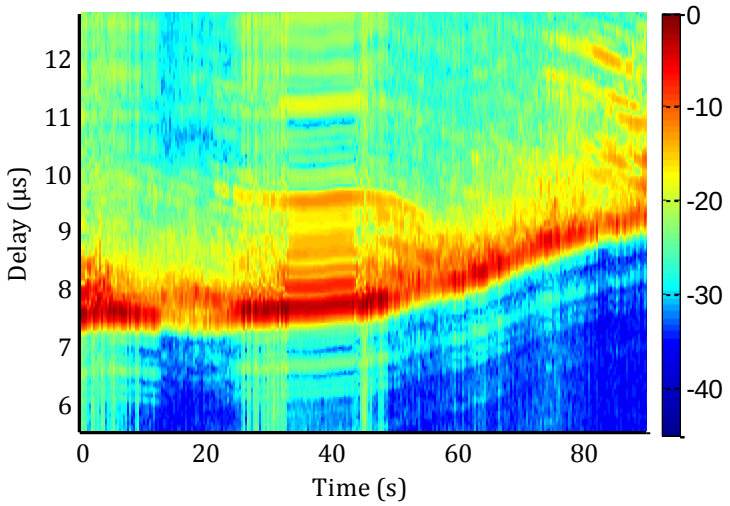

Figure 6.14: Correlation image around peak of emitter #2

The correlation peak of emitter #2 is very strong but much more disturbed by multipathes than in the suburban test.

As in the sub-urban test, tens peaks have been acquired with the matching pursuit algorithm and tracked with a loop bandwidth of 1 Hz, 1 coherent summation and a rectangular correlation window. Among the 10 resulting estimated delays, the two estimated delays tracking the peaks identified in the correlation image as the direct signals from emitter #1 and emitter #2 are considered. Their variation is plotted on Figure 6.15 and compared with the variation of the reference PR.

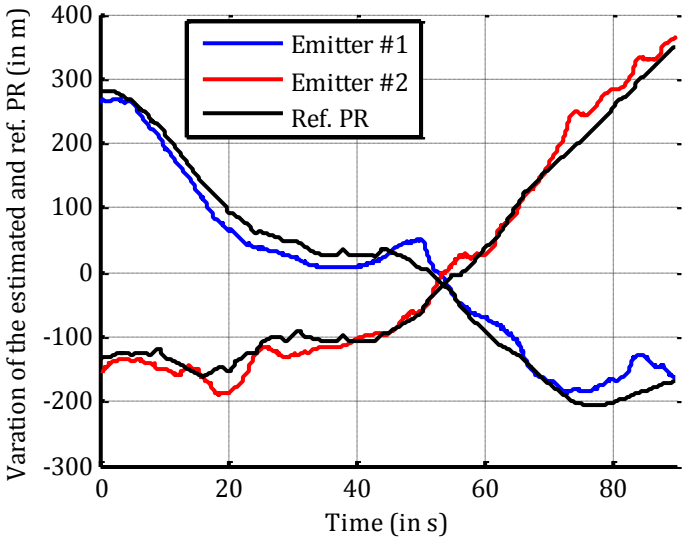

Figure 6.15: Variation of estimated delay and comparison with the variation of reference PR, for each emitter

The resulting tracking error variation (difference between estimated delay and reference delay variations) is shown on Figure 6.16, for each emitter.

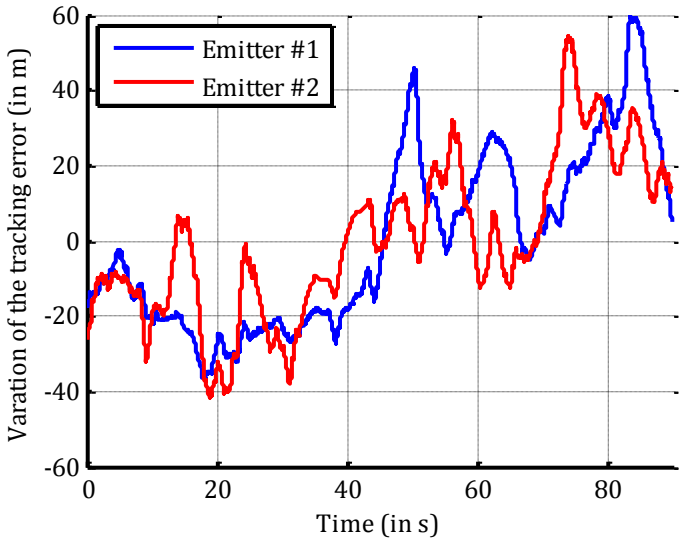

Figure 6.16: Tracking error variation, for each emitter

The different component of the tracking error are:

- the error due to multipath
- and the clock offset between emitters and GPS time
- error in the reference trajectory (quite large as it can be seen on Figure 6.11)

The multipath component, that produces the quick variation in the tracking error, appears more clearly than in the sub-urban test (Figure 6.8) because of the more constrained environment. The error due to the offset between the emitters' time and GPS time, common to the 2 tracking errors, is still observable. Another error component is brought by the imprecise reference trajectory.

As previously, to observe a clock error-free quantity the TDOA measurement is computed. Figure 6.17 shows the variation of the TDOA measurement compared to the variation of reference TDOA and Figure 6.18 shows the TDOA error (difference between TDOA measurement and reference TDOA).

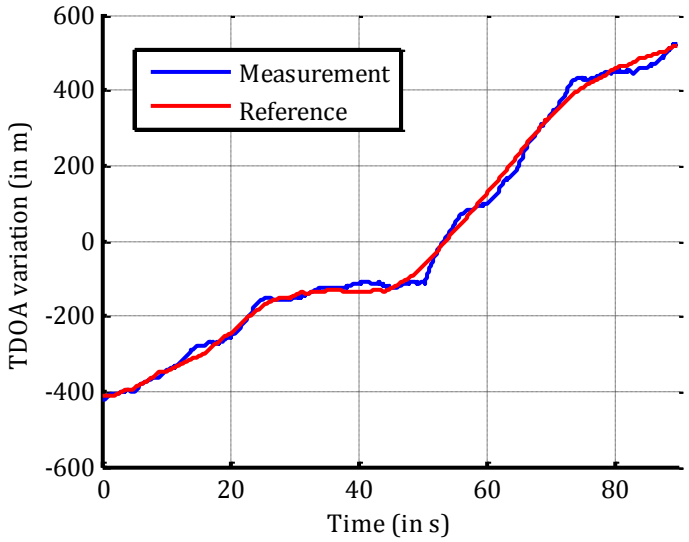

Figure 6.17: TDOA measurement compared to the reference TDOA

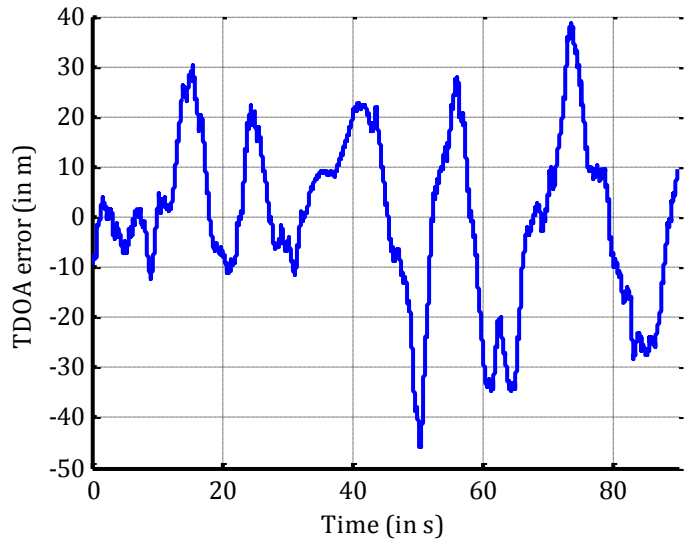

Figure 6.18: TDOA measurement error

Due to more intense multipathes, TDOA measurement error, whose statistics is depicted in Table 6.3, is larger than in the sub-urban test. Note that part of the TDOA error is due to the bad precision of the reference trajectory, whose error reaches sometimes 20 meters, according to Figure 6.11.

Table 6.3: TDOA measurement error statistics

Standard deviation	16 meters
66% time error	16 meters
90% time error	27 meters
Maximum error	45 meters

The standard deviation is comparable to that obtained in the in MFN urban test in the previous section, which is quite normal since both concern in urban environment. No conclusion can be done on the impact of NLOS effect since absolute TDOA could not be obtained. However, it can be thought that the NLOS error could be mitigated by the TDOA operation, since the difference of two NLOS bias is expected to be null in average.

As a conclusion, SFN appears to be interesting when used with TDOA measurements, especially when the reference time of emitters in unknown. In addition, TDOA measurement presents, by construction, a natural way to mitigate the NLOS error (even if it could not be proven on real signal).

Conclusion and perspectives

6.3 Contributions

The main contribution of this thesis is the demonstration of the feasibility of a TOA/TDOA positioning solution using an OFDM signal-of-opportunity in a terrestrial network, based on result obtained on real signals.

In collaboration with another PhD student [23], a ranging method using DVB-T signal has been developed. This includes acquisition and tracking algorithms adapted to terrestrial multi- and single-frequency networks, with, for example, the concepts of multiple peaks acquisition and tracking, periodic re-acquisitions, correlation windowing and coherent and non-coherent summations.

A theoretical analysis of acquisition and tracking performance has been done. This includes, for the acquisition, the definition of the detection probability as a function of SNR given a false alarm probability. This analysis takes into account the different possible parameters of the DVB-T signal and the different parameters of the correlation computation (number of summations). For example with the DVB-T parameters used in France and with standard tracking parameters (1 coherent and non-coherent summation), and for a false alarm probability of 10^{-3} and a detection probability of 0.99, the SNR threshold is about -10 dB.
For the tracking, the expression of the standard deviation of the tracking error and the expression of the tracking threshold have been derived theoretically and validated by simulation. This analysis takes into account the different possible parameters of the DVB-T signal and the different parameters of the correlation computation (summation, windowing). For example with the DVB-T parameters used in France and with standard tracking parameters (1 Hz loop bandwidth, 1 summation, and rectangular window) the tracking error standard deviation is about 0.2 meter at -20 db of SNR and the tracking threshold is about -38 dB.

A flexible test bench, permitting TV signal recording on two reception chains (allowing antenna diversity operation), synchronized of GPS time and providing a reference position has been developed. A complete C++ software has also been developed to control the hardware and process the recording signal according to the developed ranging method. This test bench also permits the analysis of the propagation channel by providing an estimate of the channel impulse response through the computation of periodic correlations.

Tests in urban area using two reception antenna and a DVB-T emitter synchronized on GPS time have been done. The tracking performance is quite good and promising with a mean error of about 30

meters and a standard deviation of about 20 meters. Exploiting the antenna diversity during dynamic phase, the tracking performance can be improved to a mean error of about 5 meters and a standard deviation close to 10 meters which is significantly better than existing positioning solutions using signals of opportunity. Influence of tracking parameters on the tracking performance has also been analyzed, showing that a too important tracking loop bandwidth and an too important coherent summation number degrade the performance due to loss of tracking.

An indoor test has also been done, but a numerical performance cannot be provided since no reference position was available. However this test shows the possibility of tracking the DVB-T signal inside buildings.

Tests in a single-frequency network have been done in sub-urban and urban environments. The results are again very promising with a standard deviation of the TDOA error of about 5 meters in the sub-urban case and 16 meters in the urban case, proving the feasibility of simultaneous tracking of multiple emitter peaks in the same correlation function.

6.4 Perspectives

The continuation of this work includes the adaptation of the method to other OFDM standards. Indeed, DVB-T is not the most adapted standard to a final application (not dimensioned to mobile and indoor reception and weak density of emitters).

The 4G wireless communication standard of the 3GPP called Long Term Evolution (LTE) could be an interesting candidate. Indeed, LTE permits a better reception in urban environment and indoor (that was already not a problem with DVB-T) with the advantage of a high emitter density that would increase the number of PR measurements. In addition the maximum bandwidth of the LTE signal is 20 MHz, larger than the DVB-T signal, allowing better tracking performance and an improved robustness against multipathes, and it includes a Positioning Reference Signal (PRS) for positioning applications.

Another interesting candidate could be the European standard for digital terrestrial radio Digital Audio Broadcasting (DAB), operating in SFN and which directly provide in the standard definition ways to identify emitters and includes in its signal a special message with the GPS position of the emitter and time of emission of the message.

It would also interesting to characterize more finely the propagation channel in urban environment with terrestrial network, and more particularly the NLOS phenomenon.

Another continuation of this work could be to implement the complete system of positioning based on OFDM signal including the presented PR measurement engine, but also the DLL selection strategy and the positioning engine. An extension could be also to study the hybridization of OFDM-based

ranging measurements with GNSS measurements, through, for example a vectorized DLL. Indeed such architecture could permit to facilitate the selection of peak more likely to be the LOS signal or at least the shortest of the LOS. The study of the coupling with other SoO could be also pertinent.

References

[1] G. MacGougan, G. Lachapelle, R. Klukas, K. Siu, L. Garin, J. Shewfelt, and G. Cox, "Performance analysis of a stand-alone high-sensitivity receiver," *GPS Solutions*, vol. 6, no. 3, pp. 179–195, 2002.

[2] G. A. McGraw and M. S. Braasch, "GNSS multipath mitigation using gated and high resolution correlator concepts," in *Proceedings of the 1999 National Technical Meeting of The Institute of Navigation*, 1999, pp. 333–342.

[3] P. C. Fenton and J. Jones, "The theory and performance of NovAtel Inc.'s Vision Correlator," in *Proceedings of the ION GNSS 2005*, 2005, pp. 2178–2186.

[4] L. J. Garin, "The' Shaping Correlator', Novel multipath mitigation technique applicable to Galileo BOC (1, 1) modulation waveforms in high volume markets," in *Proceedings of ENC-GNSS*, 2008.

[5] M. Monnerat, R. Couty, N. Vincent, O. Huez, and E. Chatre, "The assisted GNSS, technology and applications," in *Proceedings of the 17th International Technical Meeting of the Satellite Division of The Institute of Navigation (ION GNSS 2004)*, 2001, pp. 2479–2488.

[6] J. P. Tardif, M. George, M. Laverne, A. Kelly, and A. Stentz, "A new approach to vision-aided inertial navigation," in *Intelligent Robots and Systems (IROS), 2010 IEEE/RSJ International Conference on*, 2010, pp. 4161–4168.

[7] V. Gabaglio, *GPS/INS integration for pedestrian navigation*. Schweizerische Geodätische Kommission, 2003.

[8] H. S. Cobb, "GPS pseudolites: Theory, design, and applications," Stanford University, 1997.

[9] J. Barnes, C. Rizos, J. Wang, D. Small, G. Voigt, and N. Gambale, "Locata: A new positioning technology for high precision indoor and outdoor positioning," in *Proceedings 2003 International Symposium on GNSS*, 2003, pp. 9–18.

[10] I. L. Association and others, "eLoran Definition Document," *Version*, vol. 1, p. 16, 2007.

[11] J. C. Adams, W. Gregorwich, L. Capots, and D. Liccardo, "Ultra-wideband for navigation and communications," in *Aerospace Conference, 2001, IEEE Proceedings.*, 2001, vol. 2, pp. 2–785.

[12] S. Chumkamon, P. Tuvaphanthaphiphat, and P. Keeratiwintakorn, "A blind navigation system using RFID for indoor environments," in *Electrical Engineering/Electronics, Computer, Telecommunications and Information Technology, 2008. ECTI-CON 2008. 5th International Conference on*, 2008, vol. 2, pp. 765–768.

[13] S. Wang, J. Min, and K. Y. Byung, "Location based services for mobiles: Technologies and standards," in *IEEE International Conference on Communication (ICC)*, 2008, pp. 78–92.

[14] A. Bose and C. H. Foh, "A practical path loss model for indoor WiFi positioning enhancement," in *Information, Communications & Signal Processing, 2007 6th International Conference on*, 2007, pp. 1–5.

[15] I. Quader, B. Li, W. Peng, and A. G. Dempster, "Use of fingerprinting in Wi-Fi based outdoor positioning," *Proc IGNSS, Sydney*, 2007.

[16] T. Gallagher, B. Li, A. Kealy, and A. G. Dempster, "Trials of commercial Wi-Fi positioning systems for indoor and urban canyons," in *IGNSS 2009 Symposium on GPS/GNSS*, 2009.

[17] "SKYHOOK Wireless." [Online]. Available: http://www.skyhookwireless.com/howitworks/.

[18] B. W. Parkinson, J. J. S. Jr, P. Axelrad, and P. Enge, *The Global Positioning System: Theory and Applications*. American Institute of Aeronautics & Astronautics, 1996.

[19] J. J. Caffery and G. L. Stuber, “Radio location in urban CDMA microcells,” in *, Sixth IEEE International Symposium on Personal, Indoor and Mobile Radio Communications, 1995. PIMRC’95. “Wireless: Merging onto the Information Superhighway,”* 1995, vol. 2, pp. 858 –862 vol.2.

[20] M. P. Wylie and J. Holtzman, “The non-line of sight problem in mobile location estimation,” in *, 1996 5th IEEE International Conference on Universal Personal Communications, 1996. Record*, 1996, vol. 2, pp. 827 –831 vol.2.

[21] M. Rabinowitz and J. Spilker, “A new positioning system using television synchronization signals,” *Broadcasting, IEEE Transactions on*, vol. 51, no. 1, pp. 61, 51, 2005.

[22] “TruePosition Angle of Arrival.” [Online]. Available: http://www.trueposition.com/aoa/.

[23] P. Thevenon, “S-band air interface for navigation systems: a focus on OFDM signal,” Thèse, Université de Toulouse, 2010.

[24] D. Serant, P. Thevenon, M. L. Boucheret, O. Julien, C. Macabiau, S. Corazza, M. Dervin, and L. Ries, “Development and validation of an OFDM/DVB-T sensor for positioning,” in *Position Location and Navigation Symposium (PLANS), 2010 IEEE/ION*, 2010, pp. 988–1001.

[25] D. Serant, O. Julien, C. Macabiau, L. Ries, P. Thevenon, M. Dervin, and M. L. Boucheret, “Positioning Using OFDM-based Digital TV: New Algorithms and Tests with Real Signals,” in *Proceedings of the 24th International Technical Meeting of The Satellite Division of the Institute of Navigation (ION GNSS 2011)*, Portland, OR, 2010.

[26] D. Serant, L. Ries, P. Thevenon, O. Julien, C. Macabiau, M. Dervin, and M. Boucheret, “Use of OFDM-based digital TV for ranging: Tests and validation on real signals,” in *Satellite Navigation Technologies and European Workshop on GNSS Signals and Signal Processing (NAVITEC), 2010 5th ESA Workshop on*, 2010.

[27] D. Serant, O. Julien, P. Thevenon, L. Ries, and M. Dervin, “The Digital TV Case - Positioning Using Signals-of-Opportunity Based on OFDM Modulation,” *Inside GNSS*, no. November/December 2011, pp. 54–62, 2011.

[28] P. Thevenon, D. Serant, O. Julien, C. Macabiau, M. Bousquet, L. Ries, and S. Corazza, “Positioning Using Mobile TV Based on the DVB-SH Standard,” *NAVIGATION: Journal of the Institute of Navigation*, 2011.

[29] P. Thevenon, O. Julien, C. Macabiau, D. Serant, L. Ries, S. Corazza, and M. Bousquet, “Positioning principles with a mobile TV system using DVB-SH signals and a Single Frequency Network,” in *Digital Signal Processing, 2009 16th International Conference on*, 2009, pp. 8, 1.

[30] P. Thevenon, O. Julien, C. Macabiau, D. Serant, S. Corazza, M. Bousquet, L. Ries, and T. Grelier, “Pseudo-Range Measurements Using OFDM Channel Estimation,” in *ION GNSS 2009*, 2009.

[31] I. Mateu, C. Boulanger, J.-L. Issler, L. Ries, J.-A. Avila-Rodriguez, S. Wallner, T. Kraus, B. Eissfeller, P. Mulassano, S. Germaine, J.-Y. Guyomard, F. Bastide, J. Godet, D. Hayes, D. Serant, P. Thevenon, O. Julien, and G. W. Hein, “Exploration of Possible GNSS Signals in S-band,” presented at the Proceedings of the 22nd International Technical Meeting of The Satellite Division of the Institute of Navigation (ION GNSS 2009), 2009, pp. 1573–1587.

[32] I. Mateu, C. Boulanger, J.-L. Issler, L. Ries, J.-A. Avila-Rodriguez, S. Wallner, B. Eissfeller, P. Mulassano, S. Germaine, J.-Y. Guyomard, F. Bastide, J. Godet, D. Hayes, D. Serant, P. Thevenon, O. Julien, G. W. Hein, M. Paonni, M. Caporale, and A. R. Pratt, “A Search for Spectrum: GNSS Signals in S-Band, Part II,” *Inside GNSS*, no. October 2010, pp. 46–53, 2010.

[33] J. A. . Bingham, “Multicarrier modulation for data transmission: An idea whose time has come,” *IEEE Communications magazine*, vol. 28, no. 5, pp. 5–14, 1990.

[34] Y. Li and G. Stüber, *Orthogonal Frequency Division Multiplexing for Wireless Communications (Signals and Communication Technology)*. Springer, 2006.

[35] M. Speth, S. A. Fechtel, G. Fock, and H. Meyr, "Optimum receiver design for wireless broad-band systems using OFDM. I," *Communications, IEEE Transactions on*, vol. 47, no. 11, pp. 1668–1677, 1999.

[36] M. Morelli, C. Kuo, and M. Pun, "Synchronization Techniques for Orthogonal Frequency Division Multiple Access (OFDMA): A Tutorial Review," *Proceedings of the IEEE*, vol. 95, no. 7, pp. 1427, 1394, 2007.

[37] "ETSI EN 300 744 V1.6.1: Digital Video Broadcasting (DVB); Framing structure, channel coding and modulation for digital terrestrial television." 2009.

[38] J. van de Beek, M. Sandell, and P. Borjesson, "ML estimation of time and frequency offset in OFDM systems," *Signal Processing, IEEE Transactions on [see also Acoustics, Speech, and Signal Processing, IEEE Transactions on]*, vol. 45, no. 7, pp. 1805, 1800, 1997.

[39] "ETSI TR 125 943 v6. 0.0-Universal Mobile Telecommunications System (UMTS)." 2004.

[40] S. F. Cotter and B. D. Rao, "Sparse channel estimation via matching pursuit with application to equalization," *IEEE Transactions on Communications*, vol. 50, no. 3, pp. 374–377, 2002.

[41] S. Stephens and J. Thomas, "Controlled-root formulation for digital phase-locked loops," *Aerospace and Electronic Systems, IEEE Transactions on*, vol. 31, no. 1, pp. 95, 78, 1995.

[42] "Ettus Research LLC." [Online]. Available: http://www.ettus.com/.

[43] L. Isserlis, "On a Formula for the Product-Moment Coefficient of any Order of a Normal Frequency Distribution in any Number of Variables," *Biometrika*, vol. 12, no. 1/2, pp. 134–139, Nov. 1918.

Annex A. Expression of the Correlation Function

The correlation function of the k-th OFDM symbol is defined by:

$$R^k(\hat{\tau}) = iDFT\left(\left\{\widetilde{d_p^k}P_p^k\right\}_{p\in P_S^k}\right)[\hat{\tau}] = \frac{1}{N_{P_S}}\sum_{p\in P_S^k}\widetilde{d_p^k}{P_p^k}^*\exp\left(j2\pi\frac{\hat{\tau}p}{N}\right) \quad \text{(A.1)}$$

where:

- $\hat{\tau}$ is the delay, normalized by the sampling period, where the correlation is computed
- $\widetilde{d_p^k}$ is the demodulated symbol over the p-th subcarrier of the k-th OFDM symbol
- P_p^k is the value (-1 or +1) of the pilot over the p-th subcarrier of the k-th OFDM symbol
- $\mathcal{P}_S^k$ is the set of scattered pilot indexes for the k-th OFDM symbol
- $N_{P_S} = \mathrm{card}\left(\mathcal{P}_S^k\right)$ is the number of scattered pilot

The set of pilot indexes $\mathcal{P}_S^k$ is defined by:

$${\mathcal{P}_S}^k = \left\{p \in [\![N_{0,\text{lower}}\ \ N - N_{0,\text{upper}}]\!] \mid p = 3\left((k-1)\mathrm{mod}4 + 1\right) + N_{0,\text{lower}} + 12q\ , q \in \mathbb{N}\right\} \quad \text{(A.2)}$$

where:

- $N_{0,\text{lower}}$ and $N_{0,\text{upper}}$ are the number of null subcarriers in the lower and upper guard bands.

Let us suppose that there is no impairments in the transmission, only a timing offset τ in the safe zone (see section 2.1.2.1). Thus $\widetilde{d_p^k} = d_p^k\exp\left(-j2\pi\frac{\tau p}{N}\right)$ and the expression of the correlation function becomes:

$$R^k(\hat{\tau}) = \frac{1}{N_{P_S}}\sum_{p\in\mathcal{P}_S^k} d_p^k{P_p}^*\exp\left(j2\pi\frac{(\hat{\tau}-\tau)p}{N}\right) \quad \text{(A.3)}$$

Since the pilot symbols are transmitted with boosted amplitude of 4/3, we have $d_p^k{P_p}^* = \frac{4}{3}$ and according to the pilot set expression of Eq. (2.23), the expression of the correlation function becomes:

$$R^k(\hat{\tau}) = \frac{1}{N_{P_S}}\frac{4}{3}\sum_{p=0}^{N_p-1}\exp\left(j2\pi\frac{N_{0,\text{lower}} + P_0^k + 12p}{N}\varepsilon_\tau\right) \quad \text{(A.4)}$$

where:

- $P_0^k = 3\left((k-1)\mathrm{mod}\ 4 + 1\right) \in \{12,3,6,9\}$ is the index of the first scattered pilot in the k-th OFDM symbol and
- $\varepsilon_\tau = \hat{\tau} - \tau$ is the difference between the point where the correlation is computed and the timing offset, also known as the tracking error.

Then, it comes:

$$R^k(\hat{\tau}) = \frac{1}{N_{P_S}}\frac{4}{3}\exp\left(j2\pi\frac{N_{0,\text{lower}} + P_0^k}{N}\varepsilon_\tau\right)\sum_{p=0}^{N_{P_S}-1}\exp\left(j2\pi\frac{12.\varepsilon_\tau}{N}\right)^p$$

$$R^k(\hat{\tau}) = \frac{1}{N_{P_S}}\frac{4}{3}\exp\left(j2\pi\frac{P_0^k}{N}\varepsilon_\tau\right)\exp\left(j2\pi\frac{N_{0,\text{lower}}}{N}\varepsilon_\tau\right)\frac{1-\exp\left(j2\pi\frac{12N_{P_S}}{N}\varepsilon_\tau\right)}{1-\exp\left(j2\pi\frac{12}{N}\varepsilon_\tau\right)}$$

$$R^k(\hat{\tau}) = \frac{1}{N_{P_S}}\frac{4}{3}\exp\left(j2\pi\frac{P_0^k}{N}\varepsilon_\tau\right)\exp\left(j\pi\frac{2N_{0,\text{lower}} + 12(N_{P_S}-1)}{N}\varepsilon_\tau\right)\frac{\sin\left(\pi\frac{12N_{P_S}}{N}\varepsilon_\tau\right)}{\sin\left(\pi\frac{12}{N}\varepsilon_\tau\right)}$$

But, according Table 2.3 and Table 2.6 $2N_{0,\text{lower}} + 12\left(N_{P_S}-1\right) = \text{N} - 12$ thus:

$$\boxed{R^k(\hat{\tau}) = \frac{1}{N_{P_S}}\frac{4}{3}\exp\left(j2\pi\frac{P_0^k}{N}\varepsilon_\tau\right)\exp\left(j\pi\frac{\text{N}-12}{N}\varepsilon_\tau\right)\frac{\sin\left(\pi\frac{12N_{P_S}}{N}\varepsilon_\tau\right)}{\sin\left(\pi\frac{12}{N}\varepsilon_\tau\right)}} \quad \text{(A.5)}$$

Annex B. Expression of the EMLP Discriminator Normalization Factor

The normalized EMLP discriminator is defined by:

$$D_{EMLP}^{\text{norm}}(\varepsilon_\tau) = \frac{\left|R\left(\hat{\tau} - \frac{\Delta}{2}\right)\right|^2 - \left|R\left(\hat{\tau} + \frac{\Delta}{2}\right)\right|^2}{K_{norm}|R(\hat{\tau})|^2} \tag{B.1}$$

where:

- $R(\hat{\tau}) = \frac{4}{3}\exp(j\pi\varepsilon_\tau)\,\text{sinc}(\pi\beta\varepsilon_\tau)$ is the simplified expression of the correlation function
- $\varepsilon_\tau = \hat{\tau} - \tau$ is the difference between the point where the correlation is computed and the timing offset, also known as the tracking error.

Let us determine the value of K_{norm} such that:

$$D_{EMLP}^{\text{norm}}(\varepsilon_\tau) \sim_0 \varepsilon_\tau \tag{B.2}$$

Supposing ε_τ close to zero it comes:

$$D_{EMLP}^{\text{norm}}(\varepsilon_\tau) = \frac{\text{sinc}\left(\pi\beta\left(\varepsilon_\tau - \frac{\Delta}{2}\right)\right)^2 - \text{sinc}\left(\pi\beta\left(\varepsilon_\tau + \frac{\Delta}{2}\right)\right)^2}{K_{norm}\,\text{sinc}(\pi\beta\varepsilon_\tau)^2}$$

By performing simple asymptotic analysis, knowing that $\text{sinc}(\pi\beta\varepsilon_\tau) \sim_0 1$ and developing the sinc function it comes:

$$D_{EMLP}^{\text{norm}}(\varepsilon_\tau) \sim_0 \frac{\sin(\pi\beta(\varepsilon_\tau - \Delta/2))^2}{K_{norm}(\pi\beta)^2(\varepsilon_\tau - \Delta/2)^2} - \frac{\sin(\pi\beta(\varepsilon_\tau + \Delta/2))^2}{K_{norm}(\pi\beta)^2(\varepsilon_\tau + \Delta/2)^2}$$

Then:

$$D_{EMLP}^{\text{norm}}(\varepsilon_\tau) \sim_0 \frac{\sin(\pi\beta(\varepsilon_\tau - \Delta/2))^2(\varepsilon_\tau + \Delta/2)^2 - \sin(\pi\beta(\varepsilon_\tau + \Delta/2))^2(\varepsilon_\tau - \Delta/2)^2}{K_{norm}(\pi\beta)^2(\varepsilon_\tau - \Delta/2)^2(\varepsilon_\tau + \Delta/2)^2}$$

But $\sin(x) = \frac{1-\cos(2x)}{2}$, thus:

$$D_{EMLP}^{\text{norm}}(\varepsilon_\tau) \sim_0 \frac{\frac{1-\cos(\pi\beta(2\varepsilon_\tau - \Delta))}{2}(\varepsilon_\tau + \Delta/2)^2 - \frac{1-\cos(\pi\beta(2\varepsilon_\tau + \Delta))}{2}(\varepsilon_\tau - \Delta/2)^2}{K_{norm}(\pi\beta)^2(\varepsilon_\tau - \Delta/2)^2(\varepsilon_\tau + \Delta/2)^2}$$

And:

$$D_{EMLP}^{\text{norm}}(\varepsilon_\tau) \sim_0 \frac{\frac{1}{2}[(\varepsilon_\tau+\Delta/2)^2-(\varepsilon_\tau+\Delta/2)^2]+\frac{(\varepsilon_\tau{}^2+(\Delta/2)^2)}{2}(\cos(\pi\beta(2.\varepsilon_\tau+\Delta))-\cos(\pi\beta(2.\varepsilon_\tau-\Delta))-\frac{\varepsilon_\tau.\Delta}{2}(\cos(\pi\beta(2\varepsilon_\tau+\Delta))+\cos(\pi\beta(2.\varepsilon_\tau-\Delta))}{(\pi\beta)^2.(\varepsilon_\tau-\Delta/2)^2.(\varepsilon_\tau+\Delta/2)^2}$$

But $\cos(p) + \cos(q) = \frac{1}{2}\cos\left(\frac{p+q}{2}\right)\cos\left(\frac{p-q}{2}\right)$, thus:

$$D_{EMLP}^{\text{norm}}(\varepsilon_\tau) \sim_0 \frac{\varepsilon_\tau.\Delta - (\varepsilon_\tau{}^2 + (\Delta/2)^2)\sin(2\pi\beta\varepsilon_\tau)\sin(\pi\beta\Delta) - \varepsilon_\tau.\Delta.\cos(2\pi\beta\varepsilon_\tau)\cos(\pi\beta\Delta)}{K_{norm}(\pi\beta)^2.(\varepsilon_\tau - \Delta/2)^2.(\varepsilon_\tau + \Delta/2)^2}$$

Thus, using that $\frac{\sin(kx)}{x} \underset{x\to 0}{\longrightarrow} k$, it comes:

$$\frac{D_{EMLP}^{\text{norm}}(\varepsilon_\tau)}{\varepsilon_\tau} \underset{\varepsilon_\tau\to 0}{\longrightarrow} \frac{1 - (\Delta/2)\pi\beta.\sin(\pi\beta\Delta) - \cos(\pi\beta\Delta)}{K_{norm}(\pi\beta)^2.\Delta^3/2^4}$$

Thus:

$$\boxed{K_{norm} = \frac{1 - (\Delta/2)\pi\beta.\sin(\pi\beta\Delta) - \cos(\pi\beta\Delta)}{(\pi\beta)^2.\Delta^3/2^4}} \quad \text{(B.3)}$$

Annex C. Computation of Statistical Distributions of the Signal Detector of CP Algorithm

The expression of the lambda metric, used in the CP acquisition algorithm is:

$$\Lambda(m) = \frac{1}{N_{CP}} \sum_{n=m}^{N_{CP}+m-1} r_n r_{n+N}^* \ , m \in [0, N-1] \tag{C.1}$$

The signal detector, based on this metric, is:

$$T = |\Lambda(m)|^2 = \left| \frac{1}{N_{CP}} \sum_{n=m}^{N_{CP}+m-1} r_n r_{n+N}^* \right|^2 , m \in [0, N-1] \tag{C.2}$$

where:

- r_n is the n-th sample of the received signal
- N_{CP} the number of samples in the CP

Two hypotheses are considered:

- H_0: the useful signal is not present → $r_n = n_n$, with $n_n \sim C\mathcal{N}(0, \sigma_n^2)$
- H_1: the useful signal is present → $r_n = r_n^u + n_n$

C.1. Statistical distribution of the signal detector under hypothesis H_0

In this case the expression of the signal detector is:

$$T^{H_0} = |\Lambda(m)|^2 = \left| \frac{1}{N_{CP}} \sum_{n=m}^{N_{CP}+m-1} n_n n_{n+N}^* \right|^2 \tag{C.3}$$

Thanks to the central limit theorem, N_{CP} being large, the distribution of the lambda metric can be approximated by a complex normal distribution having the following statistics:

$$E[\Lambda(m)] = \frac{1}{N_{CP}} \sum_{n=m}^{N_{CP}+m-1} E[n_n] E[n_{n+N}^*] = 0$$

And:

$$Var[\Lambda(m)] = \frac{1}{N_{CP}^2} \sum_n \sum_p E[n_n n_p^*] E[n_{n+N} n_{p+N}^*] = \frac{1}{N_{CP}^2} \sum_n \sum_p \sigma_n^4 \delta(n-p) = \frac{\sigma_n^4}{N_{CP}}$$

Thus the distribution of the lambda metric is:

$$\Lambda(m) \sim C\mathcal{N}\left(0, \frac{\sigma_n^4}{N_{CP}}\right) \tag{C.4}$$

Thus the result comes:

$$\boxed{\frac{2N_{CP}}{\sigma_n^4} T^{H_0} \sim \chi_2^2} \tag{C.5}$$

C.2. Statistical distribution of the signal detector under hypothesis H_1

Preliminary result:

Let $\Lambda^u(m)$ be the metric of the CP acquisition algorithm when only the useful signal is r_n^u received. Thus:

$$\Lambda^u(m) = \frac{1}{N_{CP}} \sum_{n=m}^{N_{CP}+m-1} r_n^u (r_{n+N}^u)^* \tag{C.6}$$

Let us consider this metric at the perfect synchronization instant, denoted m_0, (i.e. $r_n = r_{n+N}$, for $n \in [m_0, N_{CP} + m_0 - 1]$)

Thus:

$$\Lambda^u(m_0) \stackrel{\text{def}}{=} \Lambda^u = \frac{1}{N_{CP}} \sum_{n=m_0}^{N_{CP}+m_0-1} |r_n^u|^2$$

Even if the received useful signal is a stochastic process (the data sent is random), the lambda metric at the perfect synchronization point can be approximated by its average value. Indeed, in the first hand:

$$E[\Lambda^u] = \frac{1}{N_{CP}} \sum_{n=m_0}^{N_{CP}+m_0-1} E[|r_n^u|^2] = \sigma_{r^u}^2 \tag{C.7}$$

On the other:

$$Var[\Lambda^u] = E[\Lambda^u \Lambda^{u*}] - E[\Lambda^u]^2 = \frac{1}{N_{CP}^2} \sum_{n=m_0}^{N_{CP}+m_0-1} \sum_{p=m_0}^{N_{CP}+m_0-1} E\left[|r_n^u|^2 |r_p^u|^2\right] - \sigma_{r^u}^4$$

But from Isserlis' theorem it can be shown that:

$$E\left[|r_n^u|^2 |r_p^u|^2\right] = \sigma_{r^u}^4 \left(1 - \delta(p-n)\right)$$

Thus:

$$Var[\Lambda^u] = \frac{\sigma_{r^u}^4}{N_{CP}}$$

For the considered DVB-T signal $N_{CP} \gg 1$, consequently the value of standard deviation of the lambda metric is negligible compared to its mean and thus the following approximation will be done in the next developments:

$$\Lambda^u = \frac{1}{N_{CP}} \sum_{n=m_0}^{N_{CP}+m_0-1} |r_n^u|^2 \cong \sigma_{r^u}^2 \tag{C.8}$$

Statistical distribution of T^{H_1}

The statistical distribution is determined at the perfect synchronization point m_0. At this point and under H_1, the expression of the signal detector is:

$$T^{H_1} = |\Lambda(m_0)|^2 = \left| \frac{1}{N_{CP}} \sum_{n=m_0}^{N_{CP}+m_0-1} (r_n^u + n_n)(r_n^u + n_{n+N})^* \right|^2 \tag{C.9}$$

Let us decompose the lambda metric in a useful part Λ^u and a noisy part Λ^n. Their expressions are:

$$\Lambda^u = \frac{1}{N_{CP}} \sum_n r_n^u r_n^{u^*} \cong \sigma_{r^u}^2 \text{ (result of Eq. Erreur ! Source du renvoi introuvable.)} \tag{C.10}$$

$$\Lambda^n = \frac{1}{N_{CP}} \sum_n r_n^u n_{n+N}^* + n_n r_n^{u^*} + n_n n_{n+N}^* \tag{C.11}$$

Again using the central limit theorem, we know that the distribution of Λ^n can be approximated by a complex normal distribution having the following statistics:

$$E[\Lambda^n] = \frac{1}{N_{CP}} \sum_n r_n^u E[n_{n+N}^*] + E[n_n] r_{n+N}^{u\ *} + E[n_n] E[n_{n+N}^*] = 0$$

and (the terms leading to a null expectancy have been deleted):

$$Var[\Lambda^n] = E[\Lambda^n \Lambda^{n^*}] = \frac{1}{N_{CP}^2} \sum_n \sum_p r_n^u r_p^{u^*} E\left[n_{n+N}^* n_{p+N}\right] + E\left[n_n n_p^*\right] r_n^{u^*} r_p^u + E\left[n_n n_{n+N}^* n_p^* n_{p+N}\right]$$

But:

$$E\left[n_{n+N}^* n_{p+N}\right] = E\left[n_n n_{p+N}^*\right] = \sigma_n^2 \delta(n-p)$$

and:

$$E\left[n_n n_{n+N}^* n_p^* n_{p+N}\right] = E\left[n_n n_p^*\right] E\left[n_{n+N}^* n_{p+N}\right] = \sigma_n^4 \delta(n-p)$$

Thus:

$$Var[\Lambda^n] = \frac{2\sigma_n^2}{N_{CP}^2} \sum_n r_n^u r_n^{u^*} + \frac{\sigma_n^4}{N_{CP}} = \frac{2\sigma_n^2 \sigma_{r^u}^2 + \sigma_n^4}{N_{CP}}$$

Thus, the distribution of the lambda metric under H_1 is:

$$\Lambda = \Lambda^u + \Lambda^n \sim \mathcal{CN}\left(\sigma_{r^u}^2, \frac{2\sigma_n^2 \sigma_{r^u}^2 + \sigma_n^4}{N_{CP}}\right) \tag{C.12}$$

Thus the result comes:

$$\boxed{\frac{2N_{CP}}{2\sigma_n^2\sigma_{ru}^2+\sigma_n^4}T^{H_1}\sim\chi_2^2(\lambda)} \quad \text{(C.13)}$$

where:

- $\lambda = 2N_{CP}\frac{\sigma_{ru}^4}{2\sigma_n^2\sigma_{ru}^2+\sigma_n^4}$ is the non-centrality parameter

C.3. Use of coherent and incoherent summations

Considering N_C coherent summations and N_I incoherent summations the signal detector becomes:

$$T_{N_C,N_I} = \frac{1}{N_I}\sum_{l=0}^{N_I-1}\left|\frac{1}{N_C}\sum_{k=0}^{N_C-1}\Lambda_k(m)\right|^2 \quad \text{(C.14)}$$

where:

- $\Lambda_k(m) = \Lambda(m+k.N_t) = \frac{1}{\mathrm{N_{CP}}}\sum_{n=m}^{N_{CP}+m-1} r_{n+k.N_t}r^*_{n+k.N_t+N_{FFT}}$ is the lambda metric computed on the k-th N_t-sized block
- $N_t = N + N_{CP}$ is the size of the complete OFDM symbol (i.e. CP included)

The coherent summation induces a multiplication of the noise variance of the lambda function by $\frac{1}{N_C}$, while incoherent summations induce a multiplication of the degree of freedom of the chi-square distribution by $\frac{1}{N_I}$. Thus the detectors statistical distribution under H_0 and H_1 hypothesis are:

$$\boxed{\frac{2N_{CP}N_CN_I}{\sigma_n^4}T^{H_0}_{N_C,N_I}\sim\chi^2_{2N_I}} \quad \text{(C.15)}$$

and:

$$\boxed{\frac{2N_{CP}N_CN_I}{2\sigma_n^2\sigma_{ru}^2+\sigma_n^4}T^{H_1}_{N_C,N_I}\sim\chi^2_{2N_I}(\lambda)} \quad \text{(C.16)}$$

where:

- $\lambda = 2N_{CP}N_CN_I\frac{\sigma_{ru}^4}{2\sigma_n^2\sigma_{ru}^2+\sigma_n^4}$ is the non-centrality parameter

Annex D. Variance of Discriminator Output and Tracking Threshold

Preliminary note : the variance computation is done supposing a perfect tracking, i.e. $\varepsilon_\tau = 0$

D.1. Reminder, notation and preliminary results

As stated in section 3.2.2.1 the noisy correlation model is:

$$R(\hat{\tau}) = \alpha R_U(\hat{\tau}) + R_N(\hat{\tau}) \tag{D.1}$$

where:

- $R_U(\hat{\tau}) = \frac{4}{3}$ is the useful correlation (i.e. without noise) as calculated in section 3.1.2, for $\varepsilon_\tau = 0$
- $\beta = \frac{12N_{P_S}}{N}$
- $R_N(\hat{\tau}) = \frac{1}{N_{P_S}} \sum_{p \in P_S^k} n_p^k P_p^{k^*} \exp\left(j2\pi \frac{\hat{\tau}p}{N}\right)$ is the noise term of the correlation.
- α is the attenuation due to propagation (pathloss).

As shown on Eq. (3.21), the signal-to-noise ratio is related to the attenuation α and to the variance of the noise on the demodulated subcarriers by :

$$SNR = \frac{\alpha^2}{\sigma_n^2} \tag{D.2}$$

As preliminary results, the statistics of the noise term of the correlation are:

- $E[R_N(\hat{\tau})] = 0$ and,
- $Var\left(R_N(\hat{\tau})\right) = E[R_N(\hat{\tau}) R_N(\hat{\tau})^*] = \frac{\sigma_n^2}{N_{P_S}}$

The non-normalized EMLP discriminator output is:

$$D_{EMLP}(\varepsilon_\tau) = \left|R\left(\hat{\tau} - \frac{\Delta}{2}\right)\right|^2 - \left|R\left(\hat{\tau} + \frac{\Delta}{2}\right)\right|^2 \tag{D.3}$$

Let us express each term of the discriminator:

$$\begin{aligned} \left|R\left(\hat{\tau} - \frac{\Delta}{2}\right)\right|^2 &= R\left(\hat{\tau} - \frac{\Delta}{2}\right) R\left(\hat{\tau} - \frac{\Delta}{2}\right)^* \\ &= \alpha^2 \left|R_U\left(\hat{\tau} - \frac{\Delta}{2}\right)\right|^2 + N^- \end{aligned} \tag{D.4}$$

with:

- $N^- = N\left(\hat{\tau} - \frac{\Delta}{2}\right)$ and,
- $N(\hat{\tau}) = \alpha R_U(\hat{\tau}) R_N(\hat{\tau})^* + \alpha^* R_N(\hat{\tau}) R_U(\hat{\tau})^* + |R_N(\hat{\tau})|^2$

In the same way:

$$\left|R\left(\hat{\tau}+\frac{\Delta}{2}\right)\right|^2 = \alpha^2\left|R_U\left(\hat{\tau}+\frac{\Delta}{2}\right)\right|^2 + N^+ \quad \text{(D.5)}$$

with:

- $N^+ = N\left(\hat{\tau}+\frac{\Delta}{2}\right)$

Equivalently, let us introduce the following notations:

- $R_U^- = R_U\left(\hat{\tau}-\frac{\Delta}{2}\right)$, $R_U^+ = R_U\left(\hat{\tau}+\frac{\Delta}{2}\right)$ and,
- $R_N^- = R_N\left(\hat{\tau}-\frac{\Delta}{2}\right)$, $R_N^+ = R_N\left(\hat{\tau}+\frac{\Delta}{2}\right)$

Thus the expression of non-normalized discriminator can be rewritten as:

$$D_{EMLP}(\varepsilon_\tau) = \alpha^2|R_U^-|^2 - \alpha^2|R_U^+|^2 + \mathcal{N} \quad \text{(D.6)}$$

with

- $\mathcal{N} = N^- - N^+$ the global noise of the discriminator.

D.2. Variance of the normalized EMLP discriminator output

Let us compute the statistics of the noise on the EMLP discriminator.

First, its expectancy:

$$E[\mathcal{N}] = E[N^-] - E[N^+] = \frac{\sigma_n^2}{N_{P_S}} - \frac{\sigma_n^2}{N_{P_S}} = 0 \quad \text{(D.7)}$$

Second, its variance:

$$Var(\mathcal{N}) = E[\mathcal{N}\mathcal{N}^*] = E[(N^- - N^+)(N^- - N^+)^*] = E\left[|N^-|^2 + |N^+|^2 - 2.\mathrm{Re}\left(N^-.N^{+^*}\right)\right] \quad \text{(D.8)}$$

Thus, the expectation of three terms has to be calculated:

Firstly, $E[|N^-|^2]$:

$$|N^-|^2 = N^-N^{-*} = (\alpha R_U^- R_N^{-*} + \alpha^* R_N^- R_U^{-*} + |R_N^-|^2)(\alpha R_U^- R_N^{-*} + \alpha^* R_N^- R_U^{-*} + |R_N^-|^2)^* \quad \text{(D.9)}$$

As R_N is a centered complex normal variable the following can be used:

- $E[R_N^- R_N^-] = 0$
- $E\left[R_N^{-(*)} R_N^{-(*)} R_N^{-(*)}\right] = 0$ (the 3rd order moment of a complex normal variable is null).

Thus, since $\varepsilon_\tau = 0$, we have

$$E[|N^-|^2] = 2\alpha^2|R_U^-|^2E[|R_N^-|^2] + E[|R_N^-|^4] = 2\frac{16}{9}\alpha^2\,\mathrm{sinc}\left(\pi\beta\frac{\Delta}{2}\right)^2\frac{\sigma_n^2}{N_{P_S}} + 2\frac{\sigma_N^4}{N_{P_S}^2} \quad \text{(D.10)}$$

Secondly, $E[|N^+|^2]$. In the same way than the previous calculation, it can be shown that:

$$E[|N^+|^2] = 2\frac{16}{9}\alpha^2 \operatorname{sinc}\left(\pi\beta\frac{\Delta}{2}\right)^2 \frac{\sigma_n^2}{N_{P_S}} + 2\frac{\sigma_N^4}{N_{P_S}^2} \tag{D.11}$$

Thirdly, $E\left[N^-.N^{+^*}\right]$:

$$N^-.N^{+^*} = (\alpha R_U^- R_N^{-^*} + \alpha^* R_N^- R_U^{-^*} + |R_N^-|^2)\left(\alpha R_U^+ R_N^{+^*} + \alpha^* R_N^+ R_U^{+^*} + |R_N^+|^2\right)^* \tag{D.12}$$

Using the same properties of normal variables than previously, it comes:

$$E\left[N^-.N^{+^*}\right] = \alpha^2 R_U^- R_U^{+^*} E[R_N^{-^*} R_N^+] + \alpha^2 R_U^{-^*} R_U^+ E\left[R_N^- R_N^{+^*}\right] + E[|R_N^-|^2|R_N^+|^2] \tag{D.13}$$

But, from the expression of $R_U(\hat{\tau})$ and supposing that $\varepsilon_\tau = 0$, we have:

- $R_U^- R_U^{+^*} = \frac{16}{9}\alpha^2 \exp(-j\pi\Delta) \operatorname{sinc}\left(\pi\beta\frac{\Delta}{2}\right)^2$
- $R_U^{-^*} R_U^+ = \frac{16}{9}\alpha^2 \exp(j\pi\Delta) \operatorname{sinc}\left(\pi\beta\frac{\Delta}{2}\right)^2$

In addition, from a similar calculation, it can be shown that:

- $E[R_N^{-^*} R_N^+] = \exp(j\pi\Delta) \operatorname{sinc}(\pi\beta\Delta)\frac{\sigma_n^2}{N_{P_S}}$,
- $E\left[R_N^- R_N^{+^*}\right] = \exp(-j\pi\Delta) \operatorname{sinc}(\pi\beta\Delta)\frac{\sigma_n^2}{N_{P_S}}$,

In addition using this property of 4 normal random variables N_1, N_2, N_3, N_4 (Isserlis' theorem [43]):

$$E[N_1N_2N_3N_4] = E[N_1N_2]E[N_3N_4] + E[N_1N_3]E[N_2N_4] + E[N_1N_4]E[N_2N_3] \tag{D.14}$$

It comes:

$$\begin{aligned} E[|R_N^-|^2|R_N^+|^2] &= E[|R_N^-|^2]E[|R_N^+|^2] + E[R_N^{-^*}R_N^+]E\left[R_N^-R_N^{+^*}\right] + E[R_N^-R_N^+]E\left[R_N^{-^*}R_N^{+^*}\right] \\ &= \frac{\sigma_n^4}{N_P^2}(1 + \operatorname{sinc}(\pi\beta\Delta)^2) \end{aligned} \tag{D.15}$$

Thus:

$$E\left[N^-N^{+^*}\right] = 2\frac{16}{9}\alpha^2 \operatorname{sinc}\left(\pi\beta\frac{\Delta}{2}\right)^2 \operatorname{sinc}(\pi\beta\Delta)\frac{\sigma_n^2}{N_{P_S}} + (1 + \operatorname{sinc}(\pi\beta\Delta)^2)\frac{\sigma_n^4}{N_{P_S}^2} \tag{D.16}$$

And finally:

$$
\begin{aligned}
Var(\mathcal{N}) &= E\left[|N^-|^2 + |N^+|^2 - 2.\mathrm{Re}\left(N^-.N^{+*}\right)\right] \\
&= 2\frac{16}{9}\alpha^2\,\mathrm{sinc}\left(\pi\beta\frac{\Delta}{2}\right)^2\frac{\sigma_n^2}{N_{P_S}} + 2\frac{16}{9}\alpha^2\,\mathrm{sinc}\left(\pi\beta\frac{\Delta}{2}\right)^2\frac{\sigma_n^2}{N_{P_S}} - \\
&\quad 2\left(2\frac{16}{9}\alpha^2\,\mathrm{sinc}\left(\pi\beta\frac{\Delta}{2}\right)^2\mathrm{sinc}(\pi\beta\Delta)\frac{\sigma_n^2}{N_{P_S}} + (1+\mathrm{sinc}(\pi\beta\Delta)^2)\frac{\sigma_n^4}{N_{P_S}^2}\right) \\
&= 2\frac{\sigma_n^2}{N_{P_S}}\left[2\frac{16}{9}\alpha^2\,\mathrm{sinc}\left(\pi\beta\frac{\Delta}{2}\right)^2\left(1-\mathrm{sinc}(\pi\beta\Delta)\right) - (1+\mathrm{sinc}(\pi\beta\Delta)^2)\frac{\sigma_n^2}{N_{P_S}}\right]
\end{aligned}
\tag{D.17}
$$

Let us consider the normalization of the DLL (normalization supposed perfect):

$$
Var(D_{EMLP}^{\mathrm{norm}}) = Var\left(\frac{D_{EMLP}}{K_{\mathrm{norm}}|\alpha R_U(\hat{\tau})|^2}\right) = \frac{Var(D_{EMLP})}{K_{\mathrm{norm}}^2\alpha^4|R_U(\hat{\tau})|^4}
\tag{D.18}
$$

where:

- $K_{\mathrm{norm}} = \frac{1-(\Delta/2)\pi\beta.\sin(\pi\beta\Delta)-\cos(\pi\beta\Delta)}{(\pi\beta)^2.\Delta^3/2^4}$ is the normalization coefficient computed in Annex A
- $\alpha R_U(\hat{\tau}) = \frac{4}{3}\alpha$ is the prompt correlation value without noise, for $\varepsilon_\tau \approx 0$. This value can be deduced from the noisy prompt correlator by averaging it or by other suitable means (e.g. from a signal power estimator).

Thus:

$$
Var(D_{EMLP}^{\mathrm{norm}}) = \frac{9}{4}\frac{1}{N_{P_S}K_{\mathrm{norm}}^2\mathrm{SNR}}\left[\mathrm{sinc}\left(\pi\beta\frac{\Delta}{2}\right)^2\left(1-\mathrm{sinc}(\pi\beta\Delta)\right) - \frac{9}{32}\frac{(1+\mathrm{sinc}(\pi\beta\Delta)^2)}{N_{P_S}\mathrm{SNR}}\right]
\tag{D.19}
$$

Thus, after some rewriting:

$$
Var(D_{EMLP}^{\mathrm{norm}}) = \frac{K_1}{N_{P_S}SNR}\left(1+\frac{K_2}{N_{P_S}SNR}\right)
\tag{D.20}
$$

with:

- $\boxed{K_1 = \frac{9\mathrm{sinc}\left(\pi\beta\frac{\Delta}{2}\right)^2\left(1-\mathrm{sinc}(\pi\beta\Delta)\right)}{4K_{\mathrm{norm}}^2}}$ and,
- $\boxed{K_2 = \frac{9\left(1+\mathrm{sinc}(\pi\beta\Delta)\right)}{32\mathrm{sinc}\left(\pi\beta\frac{\Delta}{2}\right)^2}}$

D.3. Use of coherent and non-coherent summations

The expression of the correlation function with N_C coherent summation and N_I non-coherent summations

$$
R_{N_C,N_I}(\hat{\tau}) = \frac{1}{N_I}\sum_{l=0}^{N_I-1}\left|\frac{1}{N_c}\sum_{k=0}^{N_C-1}R^{k+lN_C}(\hat{\tau})\right|^2
\tag{D.21}
$$

where

- $R^k(\hat{\tau})$ si the correlation function computed with the k-th OFDM symbol

The coherent summations induce a reduction of the noise power. Indeed, the expression of the correlation with N_C coherent summations is:

$$R_{N_C}(\hat{\tau}) = \alpha R_U(\hat{\tau}) + R_{N,N_C}(\hat{\tau}) \tag{D.22}$$

with:

- $R_{N,N_C}(\hat{\tau}) = \frac{1}{N_c}\sum_{k=0}^{N_C-1} R_N^k(\hat{\tau})$ the noisy part of the correlation averaged over N_C OFDM symbols.

As noise terms over consecutive OFDM symbols are independent, we have:

- $E\left[R_{N,N_C}(\hat{\tau})\right] = 0$ and,
- $Var\left(R_{N,N_C}(\hat{\tau})\right) = \frac{\sigma_n^2}{N_c N_{P_S}}$

Thus the correlation with N_C coherent summations can be seen has a unique correlation with a noise power divided by N_C. Consequently the expression of the discriminator variance with N_C coherent summations is:

$$Var\left(D^{\text{norm}}_{EMLP,N_C}\right) = \frac{K_1}{N_C N_{P_S} SNR}\left(1 + \frac{K_2}{N_C N_{P_S} SNR}\right) \tag{D.23}$$

Concerning non-coherent summation, the expression of the normalized EMLP discriminator can be seen as the average of N_I consecutive discriminator:

$$D^{\text{norm}}_{EMLP,N_C,N_I} = \frac{1}{N_I}\sum^{N_I} D^{\text{norm}}_{EMLP,N_C} \tag{D.24}$$

Thus, its variance can be easily computed (consecutive discriminator outputs are independent) :

$$\boxed{Var\left(D^{\text{norm}}_{EMLP,N_C,N_I}\right) = \frac{1}{N_I} Var\left(D^{\text{norm}}_{EMLP,N_C}\right) = \frac{K_1}{N_I N_C N_{P_S} SNR}\left(1 + \frac{K_2}{N_C N_{P_S} SNR}\right)} \tag{D.25}$$

Annex E. Complete results for the 5 datasets in MFN

This annex includes the complete results of the five datasets presented in section 5.2. Each dataset contains 8 tables corresponding to 8 sets of parameters (see Table E.1). For each table, the mean and standard deviation of the PR error is given (in meter), for antenna #1, antenna #2 and the combination of both antennas (minimum od the two antennas) and for the raw PR (label raw) and "minimum time window" improvement PR (label Min). Static and Dynamic phase are distinguished. Sometimes, some values could not be computed and are missing, sometimes tracking failed and DNS is present in the table.

Table E.1 Parameters sets

		Parameters		
		Correlation window	**Loop bandwidth**	**Number of coherent summation**
Keyword Table	RECT	Rectangular	1 Hz	1
	HAMMING	Hamming	1 Hz	1
	BH	Blackman-Harris	1 Hz	1
	BL 0.5Hz	Rectangular	0.5 Hz	1
	BL 2Hz	Rectangular	2 Hz	1
	BL 10Hz	Rectangular	10 Hz	1
	Nc 10	Rectangular	1 Hz	10
	Nc 100	Rectangular	1 Hz	100

E.1. Dataset #1

RECT		Dynamic phases	
		Mean	Std
Antenna 1	Raw	28.3	24.4
	Min	11	10.4
Antenna 2	Raw	31.6	16.6
	Min	19.3	7.1
Dual antenna	Raw	22.2	13.9
	Min	12.7	12.3

HAMMING		Dynamic phases	
		Mean	Std
Antenna 1	Raw	29.2	26.3
	Min	8.1	9
Antenna 2	Raw	31.2	22.7
	Min	16.5	7.6
Dual antenna	Raw	22.8	19.6
	Min	7.3	7.5

BH		Dynamic phases	
		Mean	Std
Antenna 1	Raw	33.4	30.6
	Min	9.9	9.7
Antenna 2	Raw	34.9	26.8
	Min	15.8	8.5
Dual antenna	Raw	25.1	21.6
	Min	8.2	7.7

BL 0.5Hz		Dynamic phases	
		Mean	Std
Antenna 1	Raw	72.7	93.4
	Min	66.2	87.5
Antenna 2	Raw	32.2	17.2
	Min	22	8.2
Dual antenna	Raw	29.2	17.8
	Min	19.9	6.9

BL 2Hz		Dynamic phases	
		Mean	Std
Antenna 1	Raw	30.4	24.7
	Min	7.4	9.5
Antenna 2	Raw	50.4	40.0
	Min	24.2	20.9
Dual antenna	Raw	26.0	19.9
	Min	6.0	7.7

BL 10Hz		Dynamic phases	
		Mean	Std
Antenna 1	Raw	68.1	75
	Min	24.4	44.1
Antenna 2	Raw	53.1	51.7
	Min	11.8	24.9
Dual antenna	Raw	38.1	43.8
	Min	9.3	26.1

Nc 10		Dynamic phases	
		Mean	Std
Antenna 1	Raw	29	24.7
	Min	11.2	10.4
Antenna 2	Raw	28.9	13.8
	Min	14.7	8.1
Dual antenna	Raw	22.2	13.6
	Min	10.7	10.4

Nc 100		Dynamic phases	
		Mean	Std
Antenna 1	Raw	55.1	33.3
	Min	20.9	14.2
Antenna 2	Raw	31.2	13.8
	Min	16.4	6.5
Dual antenna	Raw	27.5	14.6
	Min	11.5	9.2

E.2. Dataset #2

RECT		Static phases		Dynamic phases	
		Mean	Std	Mean	Std
Antenna 1	Raw	14	3.5	23.8	16.9
	Min	9.6		16.3	5.11
Antenna 2	Raw	8	2.3	42.7	34.4
	Min	8		26.1	16.6
Dual antenna	Raw	11.8	2.8	23.2	16.9
	Min	8.33		15	5.2

HAMMING		Static phases		Dynamic phases	
		Mean	Std	Mean	Std
Antenna 1	Raw	18.3	3.3	21.7	16.5
	Min	16		14.3	4.7
Antenna 2	Raw	5.4	3.9	33.5	22.2
	Min	5.4		18.7	7.4
Dual antenna	Raw	12.4	3.5	21.3	16.5
	Min	6		13.5	5.18

BH		Static phases		Dynamic phases	
		Mean	Std	Mean	Std
Antenna 1	Raw	20.4	2.9	18.9	11.7
	Min	18.6		11.6	4.96
Antenna 2	Raw	3.55	5.34	32.6	21
	Min	3.5		17.6	8.07
Dual antenna	Raw	12.93	3.9	18.5	11.67
	Min	3.49		11.1	5.33

BL 0.5Hz		Static phases		Dynamic phases	
		Mean	Std	Mean	Std
Antenna 1	Raw	14.9	3.7	26.7	20.2
	Min	9		21.5	13.7
Antenna 2	Raw	7.3	2.8	43.8	33.2
	Min	7.3		33.9	25.8
Dual antenna	Raw	11.1	2.79	26.1	20.4
	Min	8.84		20.6	14

BL 2Hz		Static phases		Dynamic phases	
		Mean	Std	Mean	Std
Antenna 1	Raw	15.3	5.8	23.5	16.3
	Min	4.6		11.0	5.5
Antenna 2	Raw	9.0	2.8	34.0	22.1
	Min	4.2		17.2	7.3
Dual antenna	Raw	11.4	3.3	22.5	16.1
	Min	7.0		10.7	5.5

BL 10Hz		Static phases		Dynamic phases	
		Mean	Std	Mean	Std
Antenna 1	Raw	15.5	5.7	25.6	23.4
	Min	3.7		0.5	6.4
Antenna 2	Raw	9.22	2.7	40.1	35.8
	Min	8.4		4.9	8.5
Dual antenna	Raw	11.6	3.03	20.9	16.2
	Min	-6.5		-0.8	7.17

Nc 10		Static phases		Dynamic phases	
		Mean	Std	Mean	Std
Antenna 1	Raw	13.9	3.5	24	16.8
	Min	9.6		16.2	4.8
Antenna 2	Raw	8.1	2.3	42.2	34.7
	Min	8.1		26.16	17.1
Dual antenna	Raw	11.7	2.85	23.4	16.7
	Min	8.3		15.2	5.5

Nc 100		Static phases		Dynamic phases	
		Mean	Std	Mean	Std
Antenna 1	Raw	358	8.4	203	167
	Min	362		175	151
Antenna 2	Raw	8.84	2.1	28.6	21.8
	Min	8.84		16.1	4.27
Dual antenna	Raw	13.5	2.04	24.3	16.3
	Min	7.3		13.5	7.5

E.3. Dataset #3

RECT		Static phases		Dynamic phases	
		Mean	Std	Mean	Std
Antenna 1	Raw	39.1	1.8	34.4	22
	Min	37.9		15.9	6.6
Antenna 2	Raw	57.9	1.95	33.2	8.7
	Min	51		27.7	5.91
Dual antenna	Raw	39.1	1.8	27	9.39
	Min	56.2		16	6.68

HAMMING		Static phases		Dynamic phases	
		Mean	Std	Mean	Std
Antenna 1	Raw	40.7	1.18	28.9	16.1
	Min	43.2		14.3	5.49
Antenna 2	Raw	57.8	1.69	32.6	9.17
	Min	72.57		26.6	6.8
Dual antenna	Raw	40.7	1.18	25.3	9.1
	Min	33		14.4	5.5

BH		Static phases		Dynamic phases	
		Mean	Std	Mean	Std
Antenna 1	Raw	40	1.4	28.5	16.2
	Min	42.9		14	5.2
Antenna 2	Raw	60.1	2.66	34.1	11
	Min	74.5		27.5	8.66
Dual antenna	Raw	40	1.4	25.4	10.2
	Min	33.6		14.2	5.2

BL 0.5Hz		Static phases		Dynamic phases	
		Mean	Std	Mean	Std
Antenna 1	Raw	39.8	1.4	27	8.1
	Min			19.2	5.2
Antenna 2	Raw		2.2	32.7	7.8
	Min	40	28.2	28.7	7.5
Dual antenna	Raw	39.8	1.4	26	7.3
	Min			19.2	5.27

BL 2Hz		Static phases		Dynamic phases	
		Mean	Std	Mean	Std
Antenna 1	Raw	38.4	1.0	30.5	16.2
	Min	32.7		15.1	4.9
Antenna 2	Raw	42.3	6.0	37.4	18.9
	Min	36.6		21.6	8.1
Dual antenna	Raw	38.4	1.0	26.3	10.0
	Min	66.5		14.3	5.6

BL 10Hz		Static phases		Dynamic phases	
		Mean	Std	Mean	Std
Antenna 1	Raw	137.1	1.2	41.5	37.6
	Min	140		4.67	17.35
Antenna 2	Raw	178.1	2.17	45.5	38.55
	Min	178.7		12.63	27.5
Dual antenna	Raw	137.1	1.2	31.5	29.7
	Min	317.1		7.69	22

Nc 10		Static phases		Dynamic phases	
		Mean	Std	Mean	Std
Antenna 1	Raw	39.1	1.88	34.3	20
	Min	38		16.5	6.3
Antenna 2	Raw	57.9	1.9	37.5	14
	Min	50.8		30.4	7.21
Dual antenna	Raw	39.1	1.8	30.6	14.3
	Min	56.5		16.5	6.3

Nc 100		Static phases		Dynamic phases	
		Mean	Std	Mean	Std
Antenna 1	Raw	39.2	2.83	40.2	14.8
	Min	36.2		27.4	7.5
Antenna 2	Raw	56.8	2.8	47.2	25.1
	Min	44.2		30.1	10
Dual antenna	Raw	39.2	2.7	34.2	12.4
	Min	42		23.1	6.3

E.4. Dataset #4

RECT		Static phases		Dynamic phases	
		Mean	Std	Mean	Std
Antenna 1	Raw	51	3.47	63.7	102.4
	Min	45.7	0.33	47.1	84.5
Antenna 2	Raw	47.7	4.83	24.8	18.9
	Min	34.3	0.95	10.9	10.3
Dual antenna	Raw	33.9	3.77	20.8	15.7
	Min	26.6	0.95	8.87	9.63

HAMMING		Static phases		Dynamic phases	
		Mean	Std	Mean	Std
Antenna 1	Raw	348	6.2	637.5	621.7
	Min	274.3	1.72	719.5	621.5
Antenna 2	Raw	22.5	17.3	10.7	10.7
	Min	22.2	0.2	9	10.3
Dual antenna	Raw	25.4	5.4	22.1	17.2
	Min	16.8	0.27	9	9

BH		Static phases		Dynamic phases	
		Mean	Std	Mean	Std
Antenna 1	Raw	62.6	6.02	28.6	20.8
	Min	60.4	0.71	14.6	12.5
Antenna 2	Raw	22.3	17.4	8.39	9.9
	Min	18.5	0.28	7.18	9.5
Dual antenna	Raw	21	6.2	18.2	14.6
	Min	12.7	0.28	7.3	9.7

BL 0.5Hz		Static phases		Dynamic phases	
		Mean	Std	Mean	Std
Antenna 1	Raw	49.1	8	383.7	360.1
	Min	46.4	0.36	376.1	361.7
Antenna 2	Raw	47.2	5.3	24.8	17.8
	Min	34.6	0.88	12.9	12.7
Dual antenna	Raw	32.9	4.08	24.2	17.6
	Min	25.2	0.88	12.6	12.5

BL 2Hz		Static phases		Dynamic phases	
		Mean	Std	Mean	Std
Antenna 1	Raw	51.1	3.2	59.7	92.9
	Min	45.1	0.3	27.3	58.4
Antenna 2	Raw	45.7	5.4	29.1	27.4
	Min	27.5	1.0	5.5	9.3
Dual antenna	Raw	33.2	4.0	22.1	19.4
	Min	20.1	1.0	3.6	9.1

BL 10Hz		Static phases		Dynamic phases	
		Mean	Std	Mean	Std
Antenna 1	Raw	50.9	2.9	37.4	38.1
	Min	45.01	0.34	0.87	8.82
Antenna 2	Raw	46	4.83	27.8	26
	Min	28.2	0.82	-1.46	8.99
Dual antenna	Raw	33.4	3.67	20.2	18.3
	Min	20.6	0.82	-4.75	8.06

Nc 20		Static phases		Dynamic phases	
		Mean	Std	Mean	Std
Antenna 1	Raw	51	3.4	152	212
	Min	45	0.3	133	203
Antenna 2	Raw	47.5	4.83	25.6	20.5
	Min	34.2	0.94	9.7	9.6
Dual antenna	Raw	33.9	3.79	22.6	18.5
	Min	26.7	0.94	9.08	9.15

Nc 100		Static phases		Dynamic phases	
		Mean	Std	Mean	Std
Antenna 1	Raw	49.9	7.1	29	24.5
	Min	48.4	4.27	9.9	9.3
Antenna 2	Raw	45	5.4	36.4	45.7
	Min	33.7	1.06	10.6	21.7
Dual antenna	Raw	33	3.7	23.4	24.7
	Min	24.4	1.06	5.79	8.74

E.5. Dataset #5

RECT		Static phases		Dynamic phases	
		Mean	Std	Mean	Std
Antenna 1	Raw	61.6	3.8	85.7	112
	Min	57	3.7	54.5	82.8
Antenna 2	Raw	82	2.7	23.9	24.3
	Min	79.3		7.5	12.79
Dual antenna	Raw	61.5	3.8	17.3	15.2
	Min	51.9		4.08	9.91

HAMMING		Static phases		Dynamic phases	
		Mean	Std	Mean	Std
Antenna 1	Raw	57	4.3	62.7	68.1
	Min	51.8		37.7	45.3
Antenna 2	Raw	80.9	3.4	36.3	47.4
	Min	73.6		12.2	23.9
Dual antenna	Raw	57	4.46	28.67	39.09
	Min	49.1		8.41	18

BH		Static phases		Dynamic phases	
		Mean	Std	Mean	Std
Antenna 1	Raw	56.5	5	35.1	23.2
	Min	51		20.2	13.5
Antenna 2	Raw	98.5	22.3	103.8	116
	Min	79.2		62.8	99.9
Dual antenna	Raw	56.54	5.96	26.7	24.8
	Min	46.6		4.7	14.8

BL 0.5Hz		Static phases		Dynamic phases	
		Mean	Std	Mean	Std
Antenna 1	Raw	61.5	3.6	34	20.1
	Min	59.1	2.6	22	12.4
Antenna 2	Raw	82.1	2.9	18.4	15.7
	Min	80		9.23	11.9
Dual antenna	Raw	61.5	3.5	16.2	14.1
	Min	54.9		7.4	7.69

BL 2Hz		Static phases		Dynamic phases	
		Mean	Std	Mean	Std
Antenna 1	Raw	61.3	6.5	54.1	64.6
	Min	54.3	5.5	14.6	18.2
Antenna 2	Raw	81.9	4.8	24.9	27.8
	Min	72.2		0.8	5.6
Dual antenna	Raw	61.1	6.7	16.0	16.3
	Min	46.9		1.0	8.8

BL 10Hz		Static phases		Dynamic phases	
		Mean	Std	Mean	Std
Antenna 1	Raw	61.3	5.8	DNS	DNS
	Min	54.4	5.12	DNS	DNS
Antenna 2	Raw	82	4.4	75.8	91.1
	Min	79.1		-2.6	17.2
Dual antenna	Raw	61.2	6.2	61.6	85.8
	Min	46.3		-8.06	8.51

Nc 10		Static phases		Dynamic phases	
		Mean	Std	Mean	Std
Antenna 1	Raw	61.4	3.7	51.9	54.5
	Min	57.9	3.6	20.3	12.98
Antenna 2	Raw	82	2.7	26.3	24.2
	Min	79.4		14.2	21.76
Dual antenna	Raw	61.3	3.7	19.48	15.43
	Min	52.6		9.22	12.3

Nc 100		Static phases		Dynamic phases	
		Mean	Std	Mean	Std
Antenna 1	Raw	61.3	5.1	DNS	DNS
	Min	58.2	3.39	DNS	DNS
Antenna 2	Raw	82	2.46	83.5	68
	Min	77		58.1	48.6
Dual antenna	Raw	61.2	5	53.2	43.4
	Min	55.9		25.3	19.3